Powder Spreading and Tribocharging for Additive Manufacturing Powder Bed Fusion Processes

Basel Alchikh-Sulaiman

Department of Mining and Materials Engineering McGill University, Montreal

April 2020

A thesis submitted to McGill University in partial fulfillment of the requirements for the degree of Doctor of Philosophy in Engineering.

© Basel Alchikh-Sulaiman 2020

Abstract	xiii
Résumé	xiv
Acknowledgments	xv
Contribution to original knowledge	xvi
Contribution of Authors	xvii
Chapter 1: Introduction	1
References	5
Chapter 2: Literature Review	8
2.1 Powder Characterization	
2.2 Powder Flowability	
2.2.1. Flowability Characterized by Dynamic Angle of Repose	17
2.2.2 Powder Flowability in Vacuum	18
2.2.2. Effects of Humidity on Powder Flowability	19
2.2.3. Powder Rheometer: Stability and Variable Flow Rate test (Dynamic test)	21
2.3 Powder Spreading and Surface Characterization	
2.4 Tribocharging	24
2.4.1. Metal/ Metal Contact	26
2.4.2. Metal/ Insulator contact	31
2.5 Size-Dependent Same-Material Tribocharging	
2.5.1 Same-Material Tribocharging and Segregation	32
2.6 White Light Interferometry (WLI)	
2.7 Conclusions	
References	
Chapter 3: A Novel Method for Generating a Single Layer of Powder and Calc Packing Factor with the Assistance of White-Light Interferometry, for Electron Bed Fusion (EB-PBF)	n Beam Powder
Abstract	
3.1 Introduction	45
3.1.1. Powder Spreading and Surface Characterization	49
3.1.2 Packing Factor and Contact-Sintering Mechanism	
3.2 Experimental Methods	51
3.2.1 White-Light Interferometry	51

3.2.2 Experiments	52
3.2.3 Materials	52
3.2.4 Procedure to Prepare a Single Layer of Powder	53
3.2.5 Contact-sintering	54
3.2.6 Methodology for Calculating the Density of a Single Layer (SL) of Powder	56
3.3 Results and Discussion	56
3.3.1 Calibrating Zygo Measurements	56
3.3.2 A Relation Between the Packing Factor of SL and Surface Roughness of Substrate	58
3.4 Conclusions	60
References	61
Chapter 4: For Powder Bed Additive Manufacturing Process: Correlations between Sin Layer Density and Powder Properties with the Assistance of Coherence Scanning Interferometry	ngle
Abstract	
4.1 Introduction	
4.1.1 Powder Characterization	
4.1.2 Powder Flow	
4.1.3 The Powder Rheometer	
4.1.4 Powder Spreading	73
4.2 Experimental Methods	75
4.2.1 Instruments	75
4.2.1.1. Coherence Scanning Interferometry (CSI)	75
4.2.1.2. SEM	75
4.2.1.3. Laser Diffraction for Particle Size Measurement PSD	76
4.2.2 Experiments	76
4.2.2.1. Materials	76
4.2.2.2. Procedure to Prepare a Single Layer (SL) of Powder	77
4.3 Results and Discussion	78
4.3.1 Surface Roughness Validation Measurements for Gauge Block (Zygo Vs. Profilometer)	78
4.3.2 Powder Rheometer: Stability and Variable Flow Rate (VFR)	79
4.3.3 The Effect of Vessel Material on the Flow of Powder	82
4.3.4 The Effect of Heat Radiation on Substrate Topography	83
4.3.5 The Effect of Laver Thickness on the Packing Factor	88

4.4 Conclusions	90
Appendix (A4)	91
References	93
Chapter 5: Powder Spreading and Tribocharging for Additive Manufacturing Proce	
Abstract	99
5.1 Introduction	99
5.2 Experimental Methods	102
5.2.1 White-light interferometry (WLI)	102
5.2.2 Light-Optical Microscope (LOM)	102
5.2.3 Powder Rheometer and Tribocharging	
5.2.4 Materials	103
5.2.5 Procedure to prepare a single layer (SL) of powder	103
5.3 Results and Discussion	104
5.3.1 The validation for height profile measurements for single layer of powder (WLI vs. L	
5.3.2 The detection of tribocharging with powder rheometer	
5.3.3 Effects of the layer thickness over packing factors (CS in vacuum chamber)	
5.4 Conclusions	
References	108
Chapter 6: Detection of Tribocharging Effect for Metallic Powders with a Powder R	
Abstract	112
6.1 Introduction	112
6.2 Materials and Methods	115
6.2.1 Rheometer	115
6.2.2 Instruments for Detecting Charging	117
6.2.3 Materials	
6.2.4 Procedure for Tribocharging Experiments	118
6.2.4.1 Method (1)	
6.2.4.2 Method (2)	118
6.3 Results and Discussion	
6.3.1 Method (1)	
6 3 2 Method (2)	121

6.4 Conclusion	124
Appendix (A6)	125
References	126
Chapter 7: The Effect of Tribocharging and Same-material Bipolar Charging on Powder Flowability with the Assistance of Powder Rheometer	
Abstract	130
7.1 Introduction	130
7.1.1 Flowability	131
7.1.2 Physics of Tribocharging	132
7.1.2.1 Different-material Tribocharging	133
7.1.2.2 Same-material Bipolar Charging	133
7.1.2.2.1 Same-material Charging and Segregation	134
7.1.3 Tribocharging in Hall Flowmeter	134
7.2 Materials and Methods	135
7.2.1 Powder Characterization	135
7.2.2 Powder Rheometer	136
7.3 Results	139
7.3.1 The Energy Values for the CFR Test for Inconel 718	139
7.3.1.1 Charging Effect between the Vessel and Powder (Variants 1 & 2)	139
7.3.1.2 Flow Measurements Before and After the CFR Test	140
7.3.2 The Effect of Vessel Material on Tribocharging	141
7.3.3 The Effect of Same-material Bipolar Charging	143
7.3.4 Same-Material Bipolar Charging for a Non-Conductive Material	144
7.4 Discussion	145
7.4.1 Effect of Tribocharging on Total Flow Energy	145
7.4.2 Same-Material Bipolar Charging for a Non-Conductive Material	147
7.5 Conclusions	148
Appendix (A7)	149
References	150
Chapter 8	155
8.1 Global Discussion	155
8.1.1 The Effect of Tribocharging on Spreading	155

References	
8.2 Conclusions	
8.3 Future work	

List of Figures

Figure 2.1: (a) Schematic diagram of Electron Beam Powder bed fusion (EB-PBF) process with three major steps [7]; and (b) industrial electron beam powder bed fusion (Arcam system) with some process parameters and design detail [5,10]
Figure 2.2: (a) Setup for measuring the angle of repose; (b) ASTMB212-13 the Hall funnel-flowmeter apparatus with dimensions; (c) Image for the utilized Hall flowmeter at NRC-Boucherville; (c and d) Images for two angles of repose for cohesive and very-free-flowing powders [31].
Figure 2.3: (a) Schematic diagrams for two dynamic angles of repose for cohesive and very-flowing powders, and (b) variations for same powders with respect to their rotational speeds [23]
Figure 2.4: (a) Phase diagram determining the transition between the flow regimes as a function of particle diameter [38]; and (b) Diagram of revolution powder analyzer [6]
Figure 2.5: (a) Flow times of PS304 feedstock powders with 45 to 106μm angular and spherical BaF2-CaF2 particles as a function of percent relative humidity; (b) Flow times of PS304 feedstock with angular 45 to 53μm and 90 to 106μm; and (c) Experimental setup for controlled humidity powder flow tests [28].
Figure 2.6: (a) Image for the FT4 powder rheometer set-up instrument, (b) four blades utilized with the rheometer, (c) principle of flow-energy diagram, (d) experiment measurements [37], and (e) experiment measurements [41]
Figure 2.7: (a and b) schematic of AM spreading processes [6], (c) the cross section of one style of the industrial electron beam powder bed fusion (Arcam system) spreading system [15], and (d) dual-inclined combs for the EBSM Chinese system [45]
Figure 2.8: Scheme of the apparatus used by Kwetkus and Sattler [54]
Figure 2.9: Charging curves for Ni powder plotted with respect to number of contacts [54] 29
Figure 2.10: Charging curves for La, Cr and Nb powder plotted with respect to the number of contacts [54]
Figure 2.11: A schematic diagram of the WLI used to measure the surface features with Mirau interferometer [88]
Figure 3.1: Schematic diagrams for two dynamic angles of repose for cohesive and very-flowing

gure 3.2: (a and b) schematic of AM spreading processes, (c) the cross section of one style e industrial electron beam powder bed fusion (Arcam system) spreading system, and (d) du clined combs for the EBSM Chinese system.		
gure 3.3: A measured Inconel 718 substrate with White-light interferometry. The color conton this image was 20 μ m per color division, and the surface roughness Ra = 3.44 μ m		
Figure 3.4: (a) Image for the utilized stainless-steel 316L puck, and (b) the measured surface with White-light interferometry (right). The color contour for this image was 10 μ m per color division, and the flatness of the puck was around \pm 9 μ m.		
Figure 3.5: (a) the lower side of a funnel used to pour powder particles with a 2.48 mm outlet diameter, (b) dimensions of the precise-machine cavity that was fabricated with a definite height, and (c) an image for set-up.		
Figure 3.6: (a) A diagram for the set-up and (b) the procedure to prepare a single layer of powder.		
Figure 3.7: (a) image via the window of chamber during the contact-sintering, (b) image of contact-sintered Cp-Ti over the substrate with Zygo NewView 8000 and 50x Mirau lens, and (c) SEM image of contact-sintered Cp-Ti over the substrate		
Figure 3.8: (a) Gauge block used for this measurement with three scanning positions at two terminals and center A, C, and B; (middle-image) the scanning results for the gauge block surface with a direction from B-to-A with No-Form and Plane Form removes (right-image); (b) variation of surface' depth (μm) without a form remove with respect to the length of gauge block (mm); and (c) variation of surface's depth (μm) with a plane-form remove with respect to the length of gauge block (mm).		
Figure 3.9: Images for three measured surfaces with color contour scale (20µm /color div) and their related height profiles.		
Figure 4.1: Image for the powder rheometer during the stability and variable flow rate (VFR) 71		
Figure 4.2: (a) A diagram for the set-up and the procedure to prepare a SL of powder, and an upper image for a SL powder sample before the CS process, (b) with the assistance of CSI, the measured SL of Ti-6Al-4V (grade 23, PSD: 15-45 μ m, powder lot 2) sample with color contour of 20 μ m/div and 4 cross-sections,(c) the extracted height profiles according to the 4 cross-sections, and (d) an SEM image for the same CS measured sample (The edge between powder-bed and substrate). 77		
Figure 4.3: (a) Image for the gauge block, (b) Examples of the Ra measuring process with Zygo, and (c) Surface roughness Ra for measured area as a function to its related area (Test 2) at a fixed reference remove region (Test 1)		

Figure 4.4: The graphs of the VFR test for three powder lots, (a) round 1 and (b) round 2 81
Figure 4.5: Flowchart for the test conducted to examine the repeatability of VFR (dynamic) test
Figure 4.6: (a) Image for the custom-made stainless steel vessel, (b) the effect of the vessel material on VFR test for powder lot 3 samples, and (c) the values for obtained test parameters
Figure 4.7: (a) The value of BFE for powder lot 3 with respect to number of repeats, and (b) the values of different VFR test parameters for the same powder were obtained for 6 repeats 83
Figure 4.8: The fixture to hold the substrate with 4 legs.
Figure 4.9: Measured substrates for 3 samples (a, b and c) for Ti-6Al-4V, and Inconel 718 (sample d) before and after the heat treatment.
Figure 4.10: Two SL samples from powder lot 2: (a) sample 4 with Ti-6Al-4V substrate, and (b) sample 5 with Inconel 718 substrate; both surfaces were obtained with color contour 20 μm/div.
Figure 5.1: (a) A diagram for the set-up and the procedure to prepare a single layer of powder, and the side image for a SL powder sample before contact-sintering, (b) with the assistance of WLI, the measured SL of Inconel 718 powder sample with color contour of 20 μm/div and four cross-sections,(c) the extracted height profile with respect to the four cross-sections, and (d and e) SEM images for the CS samples inside electrical furnace for Inconel 718 and SS316L
Figure 5.2: (Left) Surface measurement for a definite single layer (SL) of powder with WLI, and (Right) the surface measurement for the same sample with LOM
Figure 5.3: (a) The effect of the material of vessel over VFR test for Inconel 718 samples, and (b) the value of BFE for powder Inconel 718 with respect to 12 repeats
Figure 6.1: (a) Image for the FT4 powder rheometer during the VFR Repeat with the split mechanism, (b) the graph for the calculation of total flow energy, and (c) CP-Ti powder neutralized with the AC ionizing bar
Figure 6.2: SEM images for different powders (a) Inconel 718 powder Gas atomized, (b) Ti-6Al-4V (PSD =15 - 45 μ m) gas atomized, (c) Ti-6Al-4V (grade 23) with PSD = 15-45 μ m plasma atomized, (d) CP-Ti with PSD=63-90 μ m plasma atomized, (e) aluminium alloy A357 PSD=45-PSD=45-53 μ m, and (f) gas atomized stainless-steel PSD=32 - 66 μ m.
Figure 6.3: Values of BFE for two powders plotted with respect to the number of repeats 120
Figure 6.4: The VFR Repeat performed before and after ionization

Figure 6.5: BFE values for Inconel 718 and SS316L powders plotted with respect to the number of repeats.
Figure 6.6: BFE values for Ti-6Al-4V, CP-Ti, aluminum H-15, A357 and glass microspheres powders plotted with respect to the number of repeats
Figure 7.1: SEM images for different powders (a) Inconel 718 powder sample, and (b) stainless steel SS316L powder
Figure 7.2: (a) Image for the borosilicate glass vessel with representations for torque and force, (b) image for the custom-made stainless steel vessel, and (c) the graph for the calculation of total flow energy
Figure 7.3: The energy values for the continuous flow rate (CFR) test for a fresh sample of Inconel 718 powder
Figure 7.4: The total flow energy values of CFR test for Inconel 718 powder with effects of variants 1 and 2
Figure 7.5: The effect of vessel material (borosilicate glass and stainless steel) on the tribocharging for Inconel 718 powder
Figure 7.6: For the stainless steel (SS316L) powder: the comparison for the continuous flow rate (CFR) tests for the borosilicate glass and stainless steel vessels.
Figure 7.7: The graph of CFR test for the glass microspheres in the borosilicate glass vessel 144
Figure 8.1: SEM images on the edge for two SL contact-sintering samples of Ti-6Al-4V powder with (a) 15-45 μ m PSD and (b) 45-106 μ m PSD

List of Tables

Table 2.1: Specification for Hausner Ratio and Carr Index [32]
Table 2.2: Carr's method of the Powder Flowability based on their Angle of Repose [31] 15
Table 2.3: A summary of all measured densities [4]
Table 2.4: Triboelectric series [59]; the bold and underline materials listed are important for this research
Table 2.5: The modified triboelectric series based on Kwetkus and Sattler [54] and Freeman and March [59] works
Table 2.6: The constituents of Inconel 718 based on ASTM F3055-14a
Table 3.1: Physical properties for powders
Table 3.2: Samples with their related masses and substrates
Table 3.3: Packing factor values for samples 1, 2, 3, 4, 5 and 6
Table 3.4: Values of surface parameters for substrates and single layer for the 6 samples 60
Table 4.1: Equations (4.1), (4.2) and (4.3) for the spherical diameter calculated according to the projected area, surface area and volume for a powder particle; and equation (4.4) is the sphericity factor (S)
Table 4.2: The flow times for the three Ti-6Al-4V (grade 23) lots
Table 4.3: The D10, D50 and D90 for the three powder lots
Table 4.4: Different VFR tests for three powder lots for two separate rounds
Table 4.5: The stability and variable flow rate (VFR) test outputs for the three samples from powder lot 1
Table 4.6: The surface parameters for the studied substrates
Table 4.7: Packing factors for the different powder samples with related surface parameters for the SL of sample.
Table 5.1: Packing factor values for all single layer of samples
Table 6.1: Positions of Inconel 718, SS316L, Ti-6Al-4V and CP-Ti in the new triboelectric series based on %PD values

Table A6.1: The constituents of Ti-6Al-4V powder based on Carpenter powder certificate	125
Table A6.2: The constituents of CP-Ti powder based its material certificate	125
Table 7.1: The specific total flow energy Sf for Inconel 718 and stainless steel 316L pov samples	
Table 7.2: The specific total flow energy Sf for glass microspheres powder sample	147
Table A7.1: The constituents of Inconel 718 based on Carpenter powder certificate	149
Table A7.2: The chemical compositions of stainless steel SS316L [52]	149

Abstract

Despite the wide applications of powder metallurgy in the additive manufacturing (AM) technologies, the effect of powder characteristics (particle size distribution PSD, surface morphology, etc.) on the spreadability and packing factor in electron beam powder bed fusion (EB-PBF) is not well investigated. Powder spreadability and flowability are controlled by adhesive forces, friction forces (particle-particle interactions due to surface condition and topography) and coulombic forces (van der Waals forces, electrostatic and tribocharging). Currently, there are no standard procedures to measure spreadability. In this thesis, a technique has been proposed to study spreadability in which a single layer of powder is spread by a standard method, 'frozen' in the as spread condition by 'contact-sintering' and then characterized using white-light interferometry (coherence scanning interferometry).

In addition, this thesis concentrates on the effect of powder properties (composition and particle size distribution) on tribocharging, since this is a significant effect in spreadability has not been well documented. A powder rheometer is used to detect tribocharging effects for different AM metallic powders. This work presents a technique to study tribocharging generated inside the powder rheometer. A tribocharging evolution is identified, comprising three 'periods': (i) incubation, (ii) transition, and finally (iii) the electrostatic equilibrium. These characteristics are explained on the basis of powder/vessel interactions and powder/powder interactions. The results are also used to add commercial purity titanium, Ti-6Al-4V and Inconel 718 to the triboelectric series. It is also shown that there is a strong effect of the rheometer vessel material on tribocharging characteristics. Finally, the possible effect of tribocharging on spreading is discussed.

Résumé

Malgré les nombreuses applications de la métallurgie des poudres dans les technologies de fabrication additive (FA), l'effet des caractéristiques des poudres (distribution granulométrique PSD, morphologie de surface, etc.) sur l'étalement et le facteur de remplissage dans la fusion par lit de poudre à faisceau d'électrons (EB-PBF) n'est pas bien étudié. L'étalement et la coulabilité de la poudre sont contrôlées par des forces adhésives, des forces de frottement (interactions particules-particules dues à l'état de surface et à la topographie) et des forces coulombiques (forces de van der Waals, électrostatiques et triboélectriques). À l'heure actuelle, il n'existe pas de procédures standard pour mesurer l'étalement. Dans cette thèse, une technique a été proposée pour étudier l'étalement dans laquelle une seule couche de poudre est étalée par une méthode standard, 'congelée' dans l'état de propagation par 'frittage par contact 'puis caractérisée à l'aide d'interférométrie à la lumière blanche (interférométrie de numérisation de cohérence).

En outre, cette thèse se concentre sur l'effet des propriétés des poudre (composition et distribution granulométrique) sur le triboélectriques, puisqu'il s'agit d'un effet significatif sur l'étalement n'a pas été bien documenté. Un rhéomètre à poudre est utilisé pour détecter les effets triboélectriques sur différentes poudres métalliques FA. Cette recherche présente une technique permettant d'étudier le chargement triboélectrique généré à l'intérieur du rhéomètre à poudre. Une évolution tribochargée est identifiée, comprenant trois « périodes »: (i) incubation, (ii) transition, et enfin (iii) l'équilibre électrostatique. Ces caractéristiques sont expliquées sur la base des interactions poudre/navire et des interactions poudre/poudre. Les résultats sont également utilisés pour ajouter du titane de pureté commerciale, du Ti-6Al-4V et de l'Inconel 718 dans la série triboélectrique. Il est également démontré qu'il y a un fort effet du matériau du navire de rhéomètre sur les caractéristiques de triboélectriques. Enfin, l'effet possible de la triboélectriques sur l'étalement est discuté.

Acknowledgments

This thesis work was completed with the help and support of many people, to all of whom I am deeply thankful. I first thank my supervisor, Prof. Stephen Yue, for offering me this great opportunity to work on this research at McGill University and all his generous support and help and insightful research discussion throughout this study. Also, I would like to extend my sincere grateful for Mr. Louis-Philippe Lefebvre from the Powder Metallurgy research group at the National Research Council (NRC, Boucherville), for his expertise, vision and for the opportunity to work with the powder rheometer.

I would like to thank my previous colleague Dr. Paul Carriere, RadiaBeam Technologies, for his support to initialize the 'contact-sintering' research and to dedicate from his time for the training on the electron beam machine. Also, my appreciation goes to Professor Richard Chromik who provided me with the opportunity to work with the white-light interferometry.

My thanks also goes to Ms. Barbara Hanley, the graduate studies coordinator, who really helped me during the PhD study. I also thank Ms. Leslie Bernier and Ms. June Persaud for their kind assistances.

I also thank Dr. Cindy Charbonneau, Dr. Fabrice Bernier, Shirley Mercier, Patrick England, and Jean-Paul Nadeau from NRC Boucherville who supported this research. I am very thankful for the technical support at McGill including Dr. Florence Paray, Aleksandra Djuric and Robert Paquette. I would like to thank my colleagues at McGill University, Dr. Evelin Barbosa de Melo, Dr. Hanqing Che, André Liberati, Xin Chu, Yang Liu and others who supported me during this study.

I would like to thank my funding agencies without which the research would not have been possible. Acknowledgment is due to Natural Sciences and Engineering Research Council (NSERC) of Canada and Engage Grants Program, and McGill Engineering Doctoral Award (MEDA) for the financial support on my studies.

Finally, I would like to express my sincere grateful for my mother for her love, unlimited support, and motivation during my PhD journey.

Contribution to original knowledge

- A standardized technique to quantify 'spreading' was developed where a single layer (SL)
 of powder was sintered up to the point immediately prior to neck formation by electron
 beam in vacuum, to 'freeze' the packed layer, which could then be measured by white-light
 interferometry to calculate the packing factor; packing factor can be used as a measure of
 spreading.
- 2. The powder rheometer was used to determine tribocharging characteristics for different additive manufacturing (AM) metallic powders.
- 3. A new triboelectric series was obtained with the assistance of powder rheometer, where the positions of Inconel 718, commercial purity titanium and Ti-6Al-4V were proposed in this series.

Contribution of Authors

This thesis was prepared according to the guidelines for a manuscript-based thesis. These guidelines are published by the Graduate and Postdoctoral Studies office of McGill University (http://www.mcgill.ca/gps/thesis/guidelines).

The present thesis is comprised of the following five manuscripts; three of which are published and two have been submitted. The manuscripts are prepared in collaboration with people from different groups. The detailed contribution of people is listed as below.

Chapter 3: A novel method for generating a single layer of powder and calculating the packing factor with the assistance of white-light interferometry, for electron beam powder bed fusion (EB-PBF), ITSC 2019: Proceedings of the International Thermal Spray Conference, New Waves of Thermal Spray Technology for Sustainable Growth, May 26-29, 2019 (Yokohama, Japan), ASM International, pp. 893-900.

<u>Basel Alchikh-Sulaiman</u> selected powders, conducted powder spreading and contact-sintering experiments, substrate early preparations, surface measurements with white-light interferometry, and wrote the manuscript. <u>Paul Carriere</u> designed the spreading process, prepared the puck, selected the specific height cavity, and generated the G-code to run the EB machine for contact-sintering. <u>Professor Stephen Yue</u> supervised the project, provided feedback and comments during the meetings on a bi-weekly basis and edited the manuscript.

Chapter 4: For powder bed additive manufacturing process: correlations between single layer density and powder properties with the assistance of coherence scanning interferometry, *PowderMet 2019: International Conference on Powder Metallurgy & Particulate Materials,* June 23-26, 2019 (Phoenix, AZ, USA), Metal Powder Industries Federation, pp. 285-304.

<u>Basel Alchikh-Sulaiman</u> selected powders, conducted powder spreading and contact-sintering experiments, obtained all FT4 powder rheometer tests, surface measurements with coherence scanning interferometry, and wrote the manuscript. <u>Paul Carriere</u> designed the spreading process, prepared the puck, selected the specific height cavity, and generated the G-code to run the EB machine for contact-sintering. <u>Professor Stephen Yue</u> supervised the entire research, provided comments during the meetings on a bi-weekly basis and edited the manuscript.

Chapter 5: Powder spreading and tribocharging for additive manufacturing process, *Euro PM2019: European Powder Metallurgy Association*, October 13-16, 2019 (Maastricht, The Netherlands), Euro PM 2019, pp. (4347446) 1-6.

<u>Basel Alchikh-Sulaiman</u> selected powders, conducted powder spreading and contact-sintering samples inside the electrical furnace, obtained the FT4 powder rheometer tests, surface measurements with coherence scanning interferometry, and wrote the manuscript. <u>Paul Carriere</u> designed the spreading process, prepared the puck, and selected the specific height cavity. <u>Xin chu</u> helped to conduct the contact-sintering experiments in the thermal furnace. <u>Yang Liu</u> prepared the furnace for these experiments. <u>Professor Stephen Yue</u> supervised the entire research and edited the manuscript.

Chapter 6: Detection of tribocharging effect for metallic powders with a powder rheometer.

<u>Basel Alchikh-Sulaiman</u> selected powders, developed methodologies, conducted the powder rheometer tests, and wrote the manuscript. <u>Louis-Philippe Lefebvre</u> provided comments to improve the experiments. <u>Professor Stephen Yue</u> supervised the work, provided comments during the meetings on a bi-weekly basis and edited the manuscript. This chapter is a manuscript, intended for publication in a journal.

Chapter 7: The effect of tribocharging and same-material bipolar charging on powder flowability with the assistance of powder rheometer.

<u>Basel Alchikh-Sulaiman</u> selected powders, developed a methodology, conducted all the rheometer tests, and wrote the manuscript. <u>Professor Stephen Yue</u> supervised the work, provided comments during the meetings on a weekly basis and edited the manuscript. This chapter is a manuscript, intended for publication in a journal.

Chapter 1: Introduction

Additive manufacturing (AM) technology has raised significant interest in the manufacturing industry and media for the last decades [1], since it can fabricate complex geometrical parts that cannot be obtained with the classical subtractive methods, such as forming or casting [2]. Also, the AM process requires only a CAD description of the part with no need for dies or molds for the production process [2]. Although the AM technology is perfect for mass customization, it is not suitable for mass production [3]. In addition, metal processing by additive manufacturing (AM) processes has raised a lot of attention in the last decade [4].

The AM technology fabricates parts from sheets, wires or powders [5]; for metal powders, AM is classified into blown powder technology and powder bed fusion technology. In particular, blown powder technology consists of directed energy deposition (DED) and laser metal deposition (LMD) [6]. The DED process feeds the powder or wire feedstock into a melt pool to produce parts [5]. Moreover, the deposit powder for the LMD process is melted by a laser source [7].

Powder bed fusion (PBF) technology applies thermal energy (laser or electron beam) to melt specific locations in the powder bed to fabricate a component from the bottom-to-top [8]. There are two major processes: (i) electron beam powder bed fusion (EB-PBF), and (ii) laser powder bed fusion (L-PBF), which is available in several variants such as selective laser melting (SLM) [9], and direct metal laser sintering (DMLS) [6].

The deployment of powder in the EB-PBF is based on the following steps [10]: (i) storage of powder inside hoppers under vacuum; (ii) flow of powder particles under its own weight from the storage hopper to the build plane; this step is related to the powder flowability, which depends on the weight of the powder required for a single layer [11] (flowability has been investigated extensively and it is, debatable, considered a process specific [12 - 15]); and finally, (iii) powder spreading: once the powders fall from the hopper and accumulate on the build plane, the build 'table' moves downwards a definite height (typically 100 µm to 200 µm) to allow for a layer of powder to be added to the build plane and a rake spreads the powder to fill the space uniformly; this requires the powders to be spreadable. The main objective is to generate single particle layers with dense, homogenous packing characteristics, that generates a reproducible process [16, 17].

Spreading of powder and flow would, superficially, appear to be similar processes. However, there are differences between flow and spreading, and these differences have not been fully examined. The main differences between spreadability and flowability for the first layer are concerned with the build plane characteristics: topography and temperature [18, 19].

The flowability of powder can be described as the ease with which a powder flows under defined conditions [20]. Flowability cannot be quantified by a single test or be expressed as a single value or index [13, 21]. In fact, a powder might exhibit a good flow with one measurement method but exhibit poor flow with another testing method. Therefore, the quantification of flowability of powder is related to a specific test and equipment [22]. Powder flow is a function of various particle parameters: e.g. shape of particles, particle size distributions, chemical composition, as well as external factors, such as humidity, temperature [23, 24], and the effect of the equipment used for handling, storing and processing the powder.

Powder spreadability and flowability are controlled by adhesive forces (solid and liquid bridges), friction forces (particle-particle interactions due to surface condition and topography) and coulombic forces (electrostatic, van der Waals and tribocharging) [24 - 26]. In fact, electrostatic and tribocharging forces depend on differing electric potentials of the particle surfaces, and the van der Waals forces are due to electric dipoles of molecules and atoms. For the powder particles, the force intensity depends on the distance between particles, the surface chemistry of interacting particles and the particle size [26].

With regard to tribocharging, when two materials are rubbed against each other, their surface may exchange electrons. The material with the stronger affinity for negative charge can gain electrons after the two materials are separated, and the second material will have an equal amount of positive charge [27]. Tribocharging is a phenomenon that occurs in any powder process, where the charging forces acting on particles might significantly affect the process. Thus, the control of charging is important for powder handling and industrial applications (electrostatic separation, dry powder coating and electrophotography) [28]. For PBF process, the effect of tribocharging on powder flow and spreadability has not been studied or investigated.

Since the PBF is a layer-by-layer technology, the layer thickness is one of the key components of this process. The single layer powder melting is a defined research methodology for laser PBF, where several research articles have been published on this topic [9, 29 - 31]. In fact, the thickness

of a deposited layer is somewhat dictated by the beam energy. Also, the mechanical properties of a component manufactured by SLM technology depend on the properties of each single layer. To define a suitable layer thickness, the shrinkage extent during fabrication and particle size need to be considered [29].

Electron beam powder bed fusion (EB-PBF) is an additive manufacturing process in which a component is manufactured in a layer-upon-layer by melting and solidifying specific locations of each layer using a high energy electron beam in vacuum. To be able to manufacture components with the highest desirable properties, powder packing should be as dense as possible and must also be highly reproducible. However, because of challenges with powder pre-heating, thermal isolation, system architecture and build platform leveling, the characterization of a single layer of powder has never been done for EB-PBF. McGill university houses a fully customized electron beam (EB) unit, with the ability of generating a single layer of powder. In addition, the McGill system offers a full control of processing variables such as beam current, focus offset, scan strategy, accelerating voltages, etc., providing users with great flexibility to design the state-of-arts experiments.

Thus, the objective of this research was to quantitatively define spreadability and relate this to powder characterization metrics, including surface conditions, particle size distribution (PSD) and flowability. For this reason, the initial approach was to characterize flowability with a powder rheometer. In addition, the packing factor was introduced as a tool to evaluate spreadability. However, the packing factor is a difficult parameter to measure because the as-spread powder bed is unstable. We present in this thesis a novel approach to calculate the packing factor, where, the single layer of powder was produced by a standardized 'spreading' technique and then 'contact-sintered', i.e. the sintering stage immediately prior to neck formation, by electron beam in a vacuum chamber, to 'freeze' the packed layer. The heating schedule was obtained in the McGill EB unit. Then, the single layer sample was examined by the white-light interferometry to determine the packing characteristics, which was the basis of the quantification of 'spreadability'. As a result, correlations between powder characteristics, flowability and spreadability were generated.

By satisfying the above-stated objective, the following research goals were achieved in this thesis; (i) three surface topography parameters $(R_a, Skewness and S_{dq})$ were determined to compare

between the substrates before spreading. (ii) The powder rheometer was utilized to investigate relations between powder properties and flow, (iii) for different AM metallic powders, the tribocharging effect on flow was determined with the assistance of a powder rheometer, and (iv) a new triboelectric series was obtained, where the positions of Inconel 718, commercial purity titanium and Ti-6Al-4V were proposed in this series.

This thesis is a manuscript-based dissertation divided into eight chapters. A general background and the research objective, as well as the outline of the thesis, are provided in the current chapter. Chapter 2 presents a literature review concerning flowability and spreadability for AM processes, tribocharging and same-material bipolar charging, and the effect of powder properties on tribocharging. In chapter 3, a technique is introduced to examine spreadability in which a single layer of powder was spread by a standard method, 'frozen' in the as spread condition by 'contact-sintering' and then characterized using the white-light interferometry. Thus, a method to calculate the powder-bed density was established.

As a result of the contact-sintering process, different surface measurements (powder height distribution, R_a , RMS, S_{sk} and S_{dq}) are obtained with the white-light interferometry (coherence scanning interferometry) in chapter 4. The value of surface roughness (R_a) obtained with white-light interferometry was validated with a stylus profiler. Also, three surface topography parameters (R_a , Skewness and S_{dq}) were applied to compare between substrates. Finally, the powder rheometer was utilized to examine the relations between powder properties and flow.

In chapter 5, the definition of contact-sintering was expanded towards single layer of powder samples inside the electrical furnace in atmospheric pressure. To continue the validation process obtained in the previous chapter, the height profile for powder-bed and cross-section of powder-layer obtained with the white light interferometry were validated with a digital light-optical microscope. Finally, tribocharging was indirectly detected by the powder rheometer.

A technique is presented in chapter 6 to study tribocharging generated inside the powder rheometer and assess its effect on the powder flowability using the change in basic flow energy (BFE), i.e. the mean percentage difference in BFE (%PD) from Repeat 1 to the plateau. Two methods are introduced to determine the effects of particle size distribution and powder composition. Thus, the positions of commercial purity titanium (CP-Ti), Ti-6Al-4V and Inconel 718 in the new triboelectric series are proposed.

In chapter 7, the continuous flow rate (CFR) test is applied to determine the charging effects of the rheometer vessel material (borosilicate glass and stainless steel). In addition, the evolution of CFR test in the borosilicate glass vessel reveals the following periods: the incubation period, the transition period, and the electrostatic equilibrium. The incubation period disappears with the stainless steel vessel, but the other periods are maintained during the CFR test.

Finally, chapter 8 is divided into three main sections: (8.1) a global discussion is made in order to discuss the link between the chapters, and the possible effect of tribocharging on spreading is discussed. (8.2) The conclusion resulting from this thesis is provided and (8.3) the proposed future work is stated.

References

- [1] N. Hopkinson, R. Hague and P. Dickens, *Rapid Manufacturing: An Industrial Revolution* for the Digital Age. West Sussex, UK: John Wiley & Sons Ltd, 2006.
- [2] H. E. Helmer, C. Korner, and R. F. Singer, "Additive manufacturing of nickel-based superalloy Inconel 718 by selective electron beam melting: processing window and microstructure," *J. Maters. Res.*, vol. 29, pp. 1987-1996, 2014.
- [3] B. Baufeld, "Mechanical properties of Inconel 718 parts manufactured by shaped metal deposition (SMD)," *J. Mater. Eng. Perf.*, vol. 21, pp. 1416-1421, 2012.
- [4] Z. H. Liu, D. Q. Zhang, S. L. Sing, C. K. Chua, and L. E. Loh, "Interfacial characterization of SLM parts in multi-material processing: Metallurgical diffusion between 316L stainless steel and C18400 copper alloy," *Materials Character.*, vol. 94, pp. 116-125, 2014.
- [5] W. J. Sames V, "Additive manufacturing of Inconel 718 using electron beam melting: processing, post-processing and mechanical properties," Ph.D. dissertation, Dept. Nucl. Eng., Texas A&M Univ., College Station, Texas, 2015.
- [6] C. Aumund-Kopp and A. Riou, *Introduction to Additive Manufacturing Technology: A guide for Designers and Engineers*, 2nd ed. Shrewsbury, UK: EPMA, 2018.
- [7] R. M. Mahamood and E. T. Akinlabi, "Laser metal deposition of functionally graded Ti6Al4V/TiC," *Materials and Design*, vol. 84, pp. 402-410, 2015.
- [8] ASTM International, "ISO/ASTM52910-18: Additive manufacturing, design, requirements, guidelines and recommendations," *in Annual book of ASTM standards 2018*. West Conshohocken, PA: American Society for Testing and Materials, 2018.

- [9] U. S. Bertoli, A. J. Wolfer, M. J. Matthews, J. P. R. Delplanque and J. M. Schoenung, "On the limitations of volumetric energy density as a design parameter for selective laser melting," *Materials and Design*, vol. 113, pp. 331-340, 2017.
- [10] A. Klassen, T. Scharowsky, and C. Korner, "Evaporation model for beam based additive manufacturing using free surface lattice Boltzmann methods," *J. Phys. D: Appl. Phys.*, vol. 47, pp. 1-12, 2014.
- [11] ASTM International, "ASTM B213-13: standard test methods for flow rate of metal powders using the Hall flowmeter funnel," *in Annual book of ASTM standards 2013 (pp. 27-30)*. West Conshohocken, PA: American Society for Testing and Materials, 2013.
- [12] Q. Li, V. Rudolph, B. Weighl and A. Earl, "Interparticle van der Waals force in powder flowability and compactibility," *Int. J. Pharam.*, vol. 280, pp. 77-93, 2004.
- [13] A. Hassanpour and M. Ghadiri, "Characterisation of flowability of loosely compacted cohesive powders by indentation," *Part. Part. Syst. Charact.*, vol. 24, pp. 117-123, 2007.
- [14] V. Ganesan, K. A. Rosentrater, and K. Muthukumarappan, "Flowability and handling characteristics of bulk solids and powders-a review with implications for DDGS," *Biosystems Eng.*, vol. 101, pp. 425-435, 2008.
- [15] C. Pleass and S. Jothi, "Influence of powder characteristics and additive manufacturing process parameters on the microstructure and mechanical behaviour of Inconel 625 fabricated by selective laser melting," *Add. Manuf.*, vol. 24, pp. 419-431, 2018.
- [16] H. P. Zhu, Z. Y. Zhou, R. Y. Yang, and A. B. Yu, "Discrete particle simulation of particulate systems: a review of major applications and findings," *Chem. Eng. Sci.*, vol. 63, pp. 5728-5770, 2008.
- [17] Z. Xiang, M. Yin, Z. Deng, X. Mei, and G. Yin, "Simulation of forming process of powder bed for additive manufacturing," *J. Manuf. Sci. Eng.*, vol. 138, pp. 081002, 2016.
- [18] L. Loewgren and M. Wildheim, "Method for improved powder layer quality in additive manufacturing", U.S. Patent 2016/0129501 A1, May 12, 2016.
- [19] E. Parteli and T. Pöschel, "Particle-based simulation of powder application in additive manufacturing," *Powder Tech.*, vol. 288, pp. 96-102, 2016.
- [20] Mercury Scientific Inc, "Flowability analysis with the revolution," 15 June 2012. [Online]. Available: http://www.mercuryscientific.com/instruments/revolution-powder-analyzer. [Accessed: 06 November 2019].

- [21] M. Leturia, M. Benali, S. Lagarde, I. Ronga, and K. Saleh, "Characterization of flow properties of cohesive powders: A comparative study of traditional and new testing methods," *Powder Tech.*, vol. 253, pp. 423-426, 2014.
- [22] J. K. Prescott and R. A. Barnum, "On powder flowability," *Pharm. Tech.*, vol. 1, pp. 60-86, 2000.
- [23] A. Adler, "Flow properties of metal powders," Int. J. Powder Met., vol. 5, pp. 7-20, 1969.
- [24] M. K. Stanford and C. DellaCorte, "Effects of humidity on the flow characteristics of a composite plasma spray powder," *J. Therm. Spray. Tech.*, vol. 15, no. 1, pp. 33-36, 2006.
- [25] M. K. Stanford and C. DellaCorte, "Effects of humidity on the flow characteristics of PS304 plasma spray feedstock powder blend," NASA Center for Aerospace Information, Hanover, MD, May 2002.
- [26] D. Schulze, *Powders and Bulk Solids: Behavior, Characterization, Storage and Flow.* Berlin, Germany: Springer-Verlag Berlin Heidelberg, 2008.
- [27] G. Freeman and N. March, "Triboelectricity and some associated phenomena," *Mater. Sci. Tech.*, vol. 15, pp. 1454-1458, 1999.
- [28] S. Matsusaka, "Control of particle tribocharging," *KONA Powder Part. J.*, vol. 29, pp. 27-38, 2011.
- [29] I. Yadroitsev and I. Smurov, "Selective laser melting technology: from the single laser melted track stability to 3D parts of complex shape," *Physics Procedia*, vol. 5, pp. 551-560, 2010.
- [30] I. Yadroitsev, P. Bertrand and I. Smurov, "Parametric analysis of the selective laser melting process," *App. Surf. Sci.*, vol. 253, pp. 8064-8069, 2007.
- [31] T. T. Roehling, S. Wu, S. A. Khairallah, J. D. Roehling, S. S. Soezeri, M. F. Crumb and M. J. Matthews, "Modulating laser intensity profile ellipticity for microstructural control during metal additive manufacturing," *Acta Materialia*, vol. 128, pp. 197-206, 2017.

Chapter 2: Literature Review

Additive manufacturing (AM) delivers numerous design and manufacturing advantages including (i) the capability to construct complicated internal topographies and shapes, (ii) integration and optimization of functional features, (iii) a high degree of customization, (iv) reduction of post processing operations, and (v) high degree of efficiency in the usage of powders [1, 2].

Additive manufacturing technologies are classified according to source of energy, materials and joining mechanism. Materials are in the form of wires or powders; source of applied energy is either electron beam or high-energy laser [2]. Additive manufacturing, which can be performed with polymer, ceramic, and metals powders, begins with a CAD description of the component. Using this file, the machine lays down successive layers of powder in a layer-upon-layer fashion to generate the required 3D object [2]. The particles are spread onto a platform and melted by a high-energy beam (electron, plasma, or laser), leading to the geometry buildup of a part layer-by-layer [1].

For metal powders, additive manufacturing is classified into powder bed fusion (PBF) technology or blown powder technology (Directed energy deposition (DED), and Laser metal deposition (LMD)). Alternatively, PBF technology is considered more for industrial applications and has two processes: (i) laser powder bed fusion (L-PBF) is available in several variants such as direct metal laser sintering (DMLS) and selective laser melting (SLM). (ii) Electron beam powder bed fusion is dominated by Arcam AB systems (GE additive, Mölndal, Sweden), Fig. 2.1-b [2, 3].

A suitable selection of powder is a very important step to obtain required mechanical properties and microstructures for fabricated parts [4]. The following properties of powders will affect building components with EB-PBF process: (i) particle size distribution (PSD) affects the ability to generate layers with the appropriate characteristics [5]. (ii) Shape and its variation with particle size: spherical particles are needed for EB-PBF and the existence of irregular shapes and satellites can affect the powder flowability and the building process [2]. (iii) Surface roughness of particles can affect the properties of final object including density, hardness, tensile strength and surface texture; and finally (iv) the apparent and tap densities are considered important properties to ensure a 'good' layer deposition [6], a high packing density with homogeneous surface texture.

The deployment of powder in electron beam powder bed fusion (EB-PBF) is based on three major steps [7]: (a) storage of powder inside hoppers under vacuum, (b) flow of powder from storage tanks to PBF bench, a process requiring flowability, and (c) spreading of powder over the working station with a coating system, which is dependent on spreadability, **Fig. 2.1-a**. The main outcome is to generate a well packed layer; the phenomenon of particle packing is an important research area for many physical and engineering fields [8, 9].

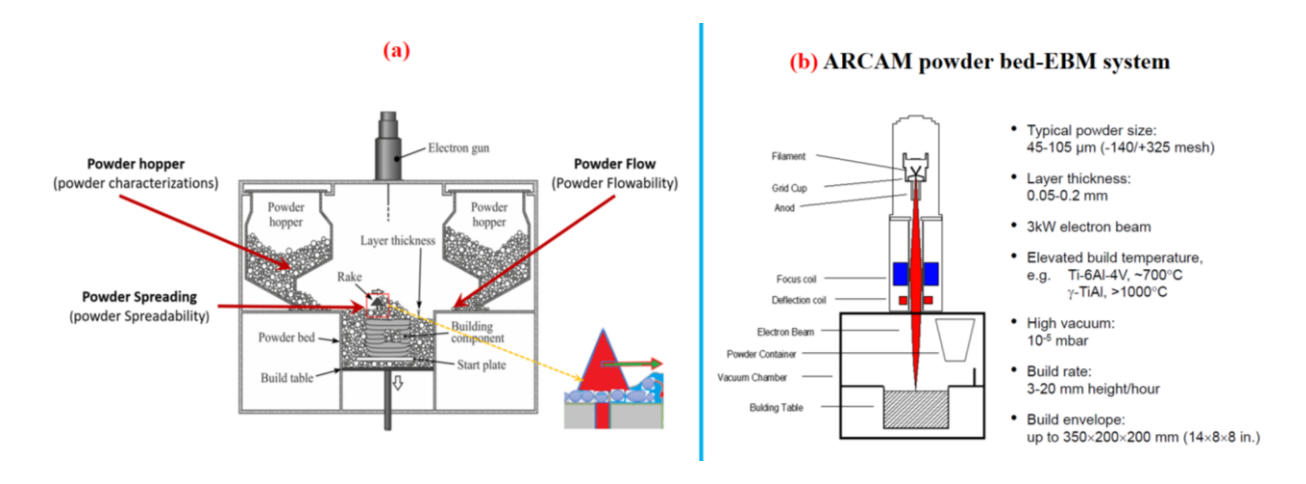


Figure 2.1: (a) Schematic diagram of Electron Beam Powder bed fusion (EB-PBF) process with three major steps [7]; and (b) industrial electron beam powder bed fusion (Arcam system) with some process parameters and design detail [5,10].

When the powder falls from hopper to the bench under its own weight, this step is related to ability of powder to flow, or flowability. Also, the flowability measurement is related to sample weight [11]. Flowability is the ability of powders to flow and is a consequence of the combination of three factors [12]: (i) the physical properties of powder, (ii) environmental conditions such as temperature of powders and relative humidity, (iii) the equipment used for handling, storing and processing these materials. Due to the influence of handling on measurement results and complex nature of powders (i.e. a powder is a group of three components together: solid particles, liquid, and trapped gas), flowability cannot be fully quantified with a single measurement technique [13]. Once the powder particles fall from hoppers and accumulate on the build plane, a rake spreads the particles over the working station and generates a powder layer with a known height; this process requires a powder to be able to spread, i.e. spreadability [14].

The physics behind the formation of a powder bed for AM has not thoroughly investigated [9]. Flowability has been studied in depth [4-6, 8, 12, 13] but there are clearly differences between flowability and spreadability, although these have not been fully distinguished.

The main differences between spreading and flow processes are concerned with the following two factors, where (i) surface characteristics (roughness and temperature [15, 16]), and (ii) the stresses experienced by the powder particles are caused by raking the particles at a constant velocity [9]. The following factors might disturb the quality of spreading process: particles morphology, surfaces roughness for particles, PSD, relative humidity for powder, chemical compositions and surface oxidation of particles. In addition, the powder spreadability is controlled by frictional forces, adhesive forces and van der Waals and electrostatic forces [11]. Nevertheless, the effect of powder mass has not determined or investigated clearly.

Electron beam powder bed fusion (EB-PBF) and other AM processes are generally operated with "fixed" parameters for a specific part. This means that inconsistent input powder characterization will translate immediately into inconsistent characterization of the printed part. Moreover, a powder with poor quality may generate defects in the product including pores, cracks, residual stresses and suboptimal surface roughness. Understanding relations between powder properties, spreading process and final-part properties are essential study, both to select suitable powders and control the spreading consistency. This will raise the question of which properties are important in terms of defining a robust powder specification [17].

The National Additive Manufacturing Innovation Institute (America Makes), and American National Standards Institute (ANSI) published on June 2018 the standardization roadmap [18] for additive manufacturing, and highlighted issues of the lacking knowledge about spreadability and electrical hazards (electro-static systems) for the environmental health and safety for the protection of operators. More research is needed to measure and quantify spreadability, as well as to connect in-between powder characteristics with spreadability. The priority of spreadability research is a medium (3-5 years); "There is no known description of spreadability or standard for how to quantitatively assess powder spreadability". In addition, the priority of electro-static hazards research is a high (0-2 years) [18].

2.1 Powder Characterization

For any AM process, it is essential to understand the powder properties and process parameters which control the quality of printed parts. A suitable selection of powder is important to obtain the required mechanical properties and microstructures [4].

To characterize powder, the following properties are considered: (i) particle size and its distribution, (ii) shape and its variation with particle size, (iii) interparticle friction and surface area, (iv) packing and flow, and (v) the internal particle structure.

For particle size analysis, the principle is to apply a spherical particle shape assumption and use a geometrical parameter (i.e. surface area, projected area, volume, minimum cross-sectional area, or maximum dimension). The equivalent spherical diameter is determined from the surface area, volume or projected area. If a particle has a projected area (A), the equivalent spherical projected diameter (D_A) is calculated with Equation (2.1) [19].

$$D_A = \sqrt{\frac{4A}{\pi}} \tag{2.1}$$

Spherical powder particles are utilized with PBF process. However, the existence of particles with irregular shapes and satellites will disturb flowability and the printing process. If the (L) is the perimeter of a particle, the sphericity factor percentage (S) is defined in Equation (2.2). It is also applied to quantify the deviation from the spherical shape of particle, where the (S) value will be between 0 and 100%; the larger the value, the more spherical shape of particles, and (S) is recommended to be above 80% [4].

$$S = \frac{4\pi A}{L^2} \times 100\% \tag{2.2}$$

Prior to the development of the method of powder production generally known as atomization, the chemical properties and morphology for powders were not fully controlled [19]. Thus, most metallic powders are fabricated with the atomization process, where this method is flexible for different alloys, easy to control, and provide flexibility in the melt purification, feedstock and chemical properties [19].

For SLM and EB-PBF, the recommended powder sizes are between 15 - 45 µm and 45 - 106 µm, respectively [4, 17], where powders with a smaller average diameter can cause process instabilities [5]. Feedstock powder contributes a significant role in determining shape and physical properties of final components; shape of particles, particle size distribution (PSD) and existence of traces of impurities inside the powder will disturb flowability and formation of powder beds, affecting the development melt pools and microscopic homogeneity [20, 21].

For EB-PBF, it is essential to use a metallic powder with a regular spherical shape and a specific particle size distribution PSD, with the minimum presence of defects such as, voids, satellites,

irregular morphology, or particle agglomerations [2]. The fraction of 'small' particles and particularly of satellites must be as small as possible because this leads to a strong reduction of density, flowability and electric conductivity. Accordingly, powders produced by plasma rotation electrode PREP have a high flowability due to a perfectly round shape free of satellites [5]. However, gas atomized powders are cheaper [22].

Powder properties such as PSD, flowability, apparent and tapped densities affect directly the ability to generate layers [6]. Several studies for PBF process reported evidences that the particle size distribution PSD used in a process had played an important role in determining final part properties [23 - 25]. For parts fabricated by SLM, investigations were conducted on the PSD effect on the density, mechanical properties, and surface roughness [26]. Flowability and apparent density control layer deposition, with a high packing density for individual layers will produce a dense component [2].

2.2 Powder Flowability

The ability to forecast powder flow behavior is significant in numerous manufacturing applications, such as powder metallurgy, ceramics, pharmaceuticals, food, and cosmetics [27 - 29]. Flowability is debatably more related with the process efficiency [17].

A quantitative representation for flowability is proposed to consider all shear stresses of powder particles that are responsible for its flow behavior. A description for powder flowing through Hall flowmeter, a powder is buckled plastically due to the weights acting on it [11]. Powder flow is controlled by density, surface chemistry, shape of particles and particle size distributions, as well as environmental conditions (bulk temperature and humidity) [28, 30].

Unfortunately, an expression for flow behavior has not yet been determined as a function of the previous parameters. Accordingly, it is essential to measure the flow properties with appropriate devices [11, 27, 28].

The powder flow depends on the adhesive forces between particles. In the Hall flowmeter, powder cannot flow under the impact of its weight when the forces between particles exceed gravitation [28].

These interparticle forces are classified into: (i) adhesive forces: solid and liquid bridges (surface tension), (ii) friction forces: particle-particle interactions due to surface condition and topography, and (iii) coulombic forces: electrostatic, van der Waals and tribocharging [11, 28].

In case of dry powder, the coulombic force due to van der Waals interactions plays an essential role. On the other hand, for moist powder, the liquid bridges are established between the contact area of particles [11].

When powders store at rest under compression stresses, such as their own weight for a long time, the adhesive forces between particle gain more strength due to the time consolidation effect [11].

Two stainless steel samples were compared and studed by Choi et al. [4], where one sample failed the Hall flowmeter test and powder flow was not measured. For this sample, a wide particle size distribution PSD with large amount of small particles and low sphericity had increased interparticle frictions. Apparent and tapped densities for non-flowable powder were lower than densities for the other flowable powder sample. However, both powder samples were successfully spread with a coater blade for SLM process, and delivered different layer thicknesses (25, 50 and 75 µm).

It was concluded that the Hall flow meter, apparent and tapped densities were not sufficient tools to describe actual packing state of powder particles across powder bed substrate.

Hausner Ratio (H_R) is the ratio between the tapped density (ρ_{tap}) over their related bulk density (ρ_{bulk}). It is defined in Equation (2.3) [31].

$$H_R = \frac{\rho_{tap}}{\rho_{bulk}} = \frac{V_{bulk}}{V_{tap}}$$
 (2.3)

Values for Hausner ratio were calculated for both samples, where values for non-flowable and flowable powders were 1.20 and 1.13 [4]. **Table 2.1** [32] indicates that an (H_R) value between 1.12-1.18 is free-flowing, whereas for (H_R) between 1.19-1.25, the powder only has a 'fair' flow characteristic.

However, the (H_R) value ranges did not describe the flow of powder samples that were recorded by Choi et al. [4]. In particular, for the non flowable powder, the (H_R) value was 1.20.

This result overlaps with similar results by Hao [33]. Thus, (H_R) is not considered to be suitable for powder-bed AM applications [6]. Moreover, it was reported that (H_R) correlate poorly with more sophisticated measurement techniques [34].

Table 2.1: Specification for Hausner Ratio and Carr Index [32]

Powder Flowability	Hausner Ratio (H_R) %	Carr Index (C _I) %
Very-Free-Flowing	1.00 - 1.11	0 - 10
Free-Flowing	1.12 - 1.18	11 - 15
Fair	1.19 - 1.25	16 - 20
Passable	1.26 - 1.34	21 - 25
Cohesive	1.35 - 1.45	26 - 31
Very Cohesive	1.46 - 1.59	32 - 37
Very, very Cohesive	> 1.60	> 38

Other researchers [6] defined three powder properties important for AM: particle shape, maximum particle diameter and particle size distribution. Powder density and flowability control powder layer properties. Powder density is determined by apparent and tap densities, and flowability is determined with avalanche angle and surface fractal. The powder layer properties are based of four factors: powder layer density, layer thickness, absorption properties and thermal conductivity [6].

The static angle of repose delivers a fast and reliable method to quantity the flowability of powder. Higher angle of repose designates a poor or cohesive flowing powder, while the lower angle indicates to freely flowing powders. It is important to mention that ISO 3435 employs this method for quantifying the free flow, or cohesiveness of powders [31, 35].

Carr's method categorized powders with respect to their flowability using the angle of repose, as shown in the following **Table 2.2** [36]. Angle of repose is another friction index, **Figure 2.2-a**.

It is formed by pouring a powder into a pile, where the tangent of α is the height divided by radius of the loose powder pile [19]. The test is conducted by closing the funnel outlet pouring 200 grams of powder and then opening the outlet [31].

Figures 2.2-d and **2.2-e** show two images of measured angle of repose for cohesive and very-free-flowing powders.

Carr (1965) proposed that the compressibility of the powder is an indicator of powder flow; this is generated by the Carr Index (C_I) in Equation (2.4) [33]:

$$C_I = \left(1 - \frac{1}{H_R}\right) \times 100\%$$
 (2.4)

According to ASTM B213-13, particle flowability can be defined by the Hall flow rate (s/50 g) as the time required for 50 grams of powder released through the funnel of the Hall flowmeter [4]. **Figures 2.2-b** and **2.2-c** show the image and dimensions of the Hall flowmeter.

Alternatively, tap density delivers an indication for flowability of a powder from measurements of the change in bulk density induced by one directional tapping [37].

Table 2.2: Carr's method of the Powder Flowability based on their Angle of Repose [31]

Angle of Repose	Powder Flowability
Greater than 55°	Very-Cohesive
45° - 55°	Cohesive
38° - 45°	Fair-to-Passable-Flow
30° - 38°	Free-Flowing
25° - 30°	Very-Free-Flowing

The interparticle cohesion forces for fine cohesive powders (Diameter_{particle} $\leq 30 \,\mu\text{m}$) might be greater than the weight of powder. Due to the interparticle cohesion, some powders cannot pass through the funnel of Hall flowmeter (i.e., no flow) [38]. Also, the ambient gas affects the flow behavior of powder.

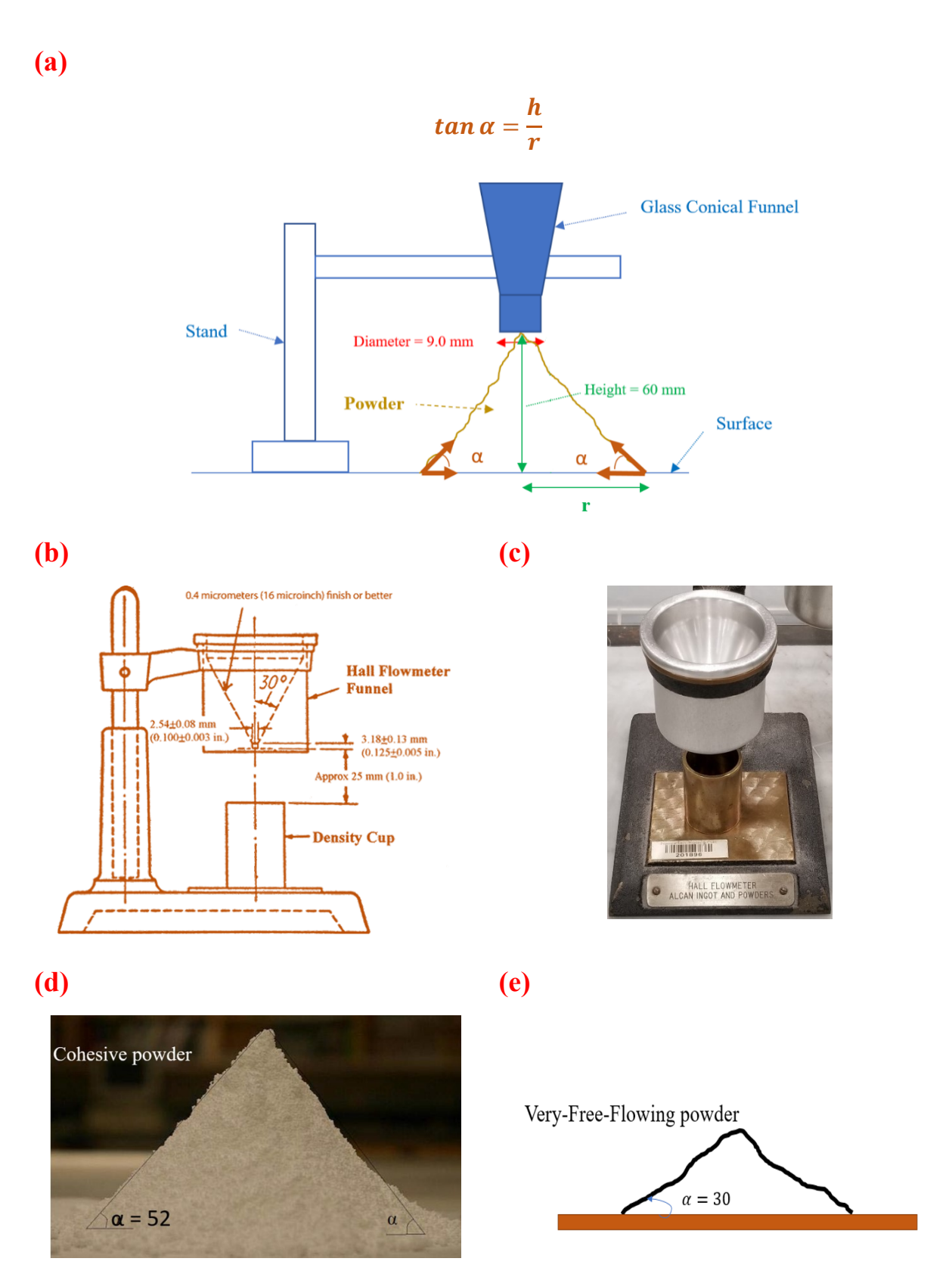


Figure 2.2: (a) Setup for measuring the angle of repose; (b) ASTMB212-13 the Hall funnel- flowmeter apparatus with dimensions; (c) Image for the utilized Hall flowmeter at NRC-Boucherville; (c and d) Images for two angles of repose for cohesive and very-free-flowing powders [31].

2.2.1. Flowability Characterized by Dynamic Angle of Repose

Dynamic angle of repose apparatus consists of a rotating, transparent cylinder filled with a specific mass of powder and a camera in front of a backlight. The camera records images of the free surface of powder, and powder cross-sectional area inside the cylinder. At the end of rotations, powder images give the dynamic angle of repose [6] (Bodhmage [31] and Gu et al. [39]) or avalanche angle, which is the angle made by the inclined surface of a powder with the horizontal when rotated inside the cylinder; a large avalanche angle means poor flowability (**Figure 2.3-a** [23]).

It is thought that the powder flow mechanism that generates an angle of repose inside a rotational powder analyzer is somewhat similar to the spreading process in the AM powder-bed process (SLM, and EB-PBF), in comparison to other flowability techniques [6].

This technique was utilized for plastic powders for selective laser sintering (SLS) by Amado et al. [23], and two different tests were presented in **Figure 2.3-b**. The flowability test was performed at 0.003 mm/sec, where 'discrete' behavior was characterised by periodic avalanches. However, 'fluidization' was obtained for the range between 77 to 177 mm/sec, where a continuous flow of powder was achieved and characterized by a steady state angle of repose. For a powder within dynamic angle of repose, a nearly similar stress state condition to spreading process with rotating roller could be achieved in comparison to other flowability techniques [23]. **Figure 2.7-b** shows a diagram for the rotating roller for AM process.

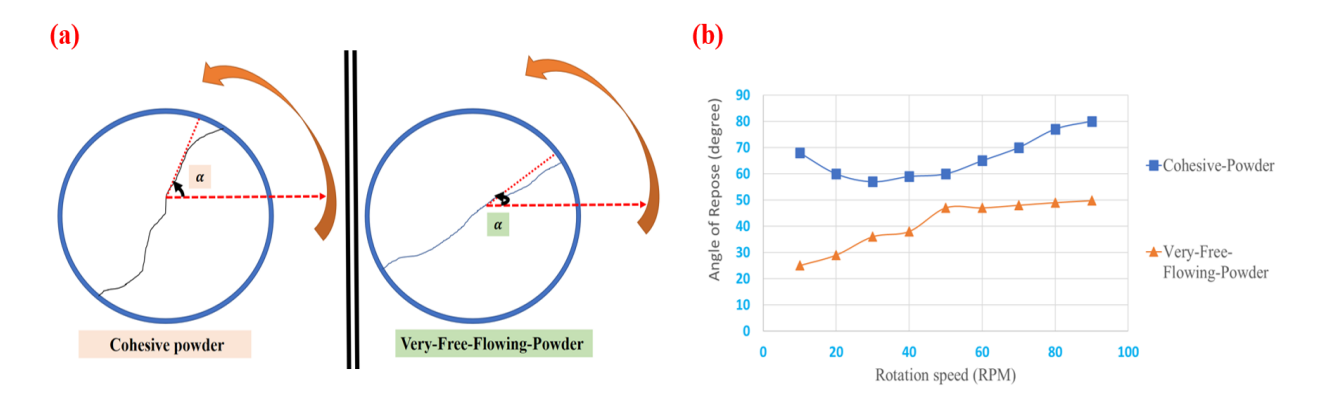


Figure 2.3: (a) Schematic diagrams for two dynamic angles of repose for cohesive and very-flowing powders, and (b) variations for same powders with respect to their rotational speeds [23].

2.2.2 Powder Flowability in Vacuum

The effect of interparticle forces was dominant for the fine cohesive powders with a particle diameter less than 100 µm. In addition, the ambient gas showed an important role in the behavior of the powder. Castellanos et al. [38] defined the following flow regimes for powders: (i) inertial flow, (ii) solid-plastic flow, (iii) fluidization, and (iv) suspension flow regime, **Fig. 2.4-a**. The flow regimes were defined by the particle size distribution (PSD), density, cohesivity, and the flow of fluid [38].

- (i) Solid-plastic regime: this regime defined by a small spacing between adjacent particles, where velocity of particles was small, and stresses were independent of velocity for simple geometries.
- (ii) Fluidization flow regime: the fluidized bed is the most known example of this regime. If the cohesive forces between particles were weak, the powder fluidized with the fluid. In fact, the spacing between particles was on the same order of magnitude as PSD. The fluid was the medium to transfer the momentum between particles and to control stresses in powder. For the fluidized bed process, a gas was purged through the powder bed, and caused a pressure drop across the bed. When the pressure drop was sufficient to support the powder weight and to overcome the interparticle cohesive forces, the powder bed became fluidized [38].
- (iii) Suspension regime: the distance between particles for this regime was much greater than PSD, and the interaction forces between particles were neglected; the average velocity of the powder is close to the fluid velocity [38].

Finally, (iv) the inertial regime: the space between particles was greater than in the plastic regime but was smaller than the particle size. The stresses between particles were due to the transport of momentum by interparticle collisions [38].

From Fig 2.4, the motion of large particles ($Diameter_{particle} \ge 5 \times 10^{-3} m$) is characterized by transition from solid-plastic regime to inertial flow [38]. For the motion of fine particles ($Diameter_{particle} \le 10^{-4} m$) at atmospheric pressure is characterized by the transition from solid-plastic to fluidization flow regime. However, the fluidization process in vacuum was suppressed [38].

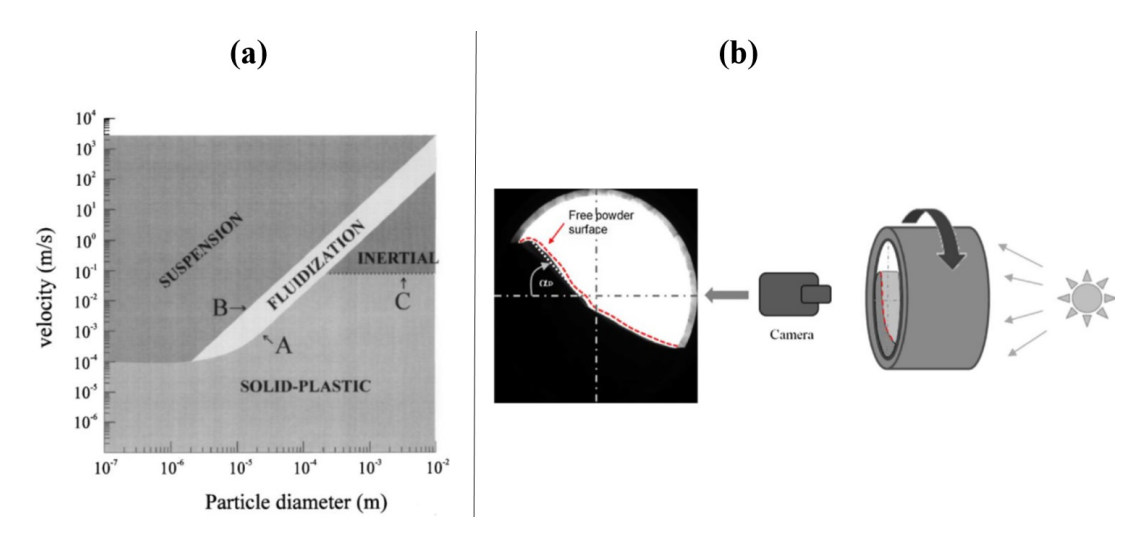


Figure 2.4: (a) Phase diagram determining the transition between the flow regimes as a function of particle diameter [38]; and (b) Diagram of revolution powder analyzer [6].

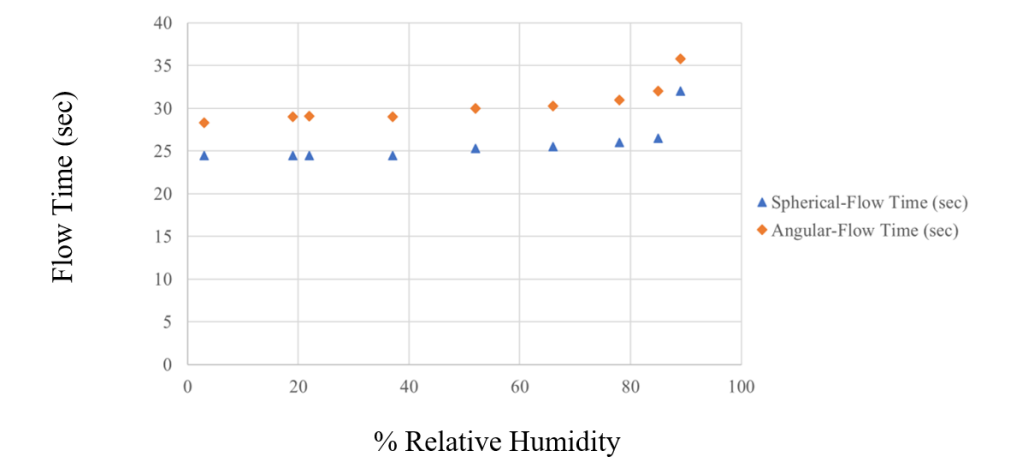
2.2.2. Effects of Humidity on Powder Flowability

The effect of humidity was investigated by comparing the powder flow characteristics at a constant temperature while modifying relative humidity (RH%) [28]. The humidity effect on a powder was examined according to the following setup in **Fig. 2.5-c**. Flow times of PS304 feedstock powders with 45 to 106 µm BaF2-CaF2 particle with respect to humidity were obtained by Stanford and DellaCorte [28].

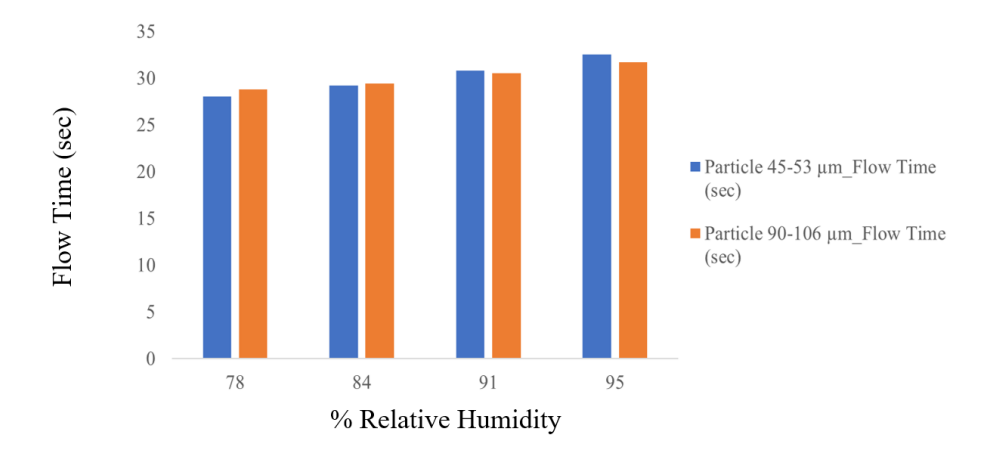
According to **Fig 2.5-b**, flow time increases with increasing relative humidity (RH%). Between 0 to 66 % relative humidity, flow was only slightly degraded with increasing humidity, but humidity had a greater effect on powder flow from 66 % to 88 % RH. The powder did not flow when relative humidity was higher than 88%.

It can be seen from **Fig. 2.5-a**, that the variation in the flow time measurement for feedstock using powder of spherical particle (Fluorides) tends to be lower than with powder of angular particle for same material. Spherical fluorides powder may provide better control and repeatability of coating deposition over a typical range of laboratory atmospheric conditions [28]. Because of relative humidity effects on flowability, it is recommended to dry powders before running process to remove absorbed moisture [4].





(b)



(c)

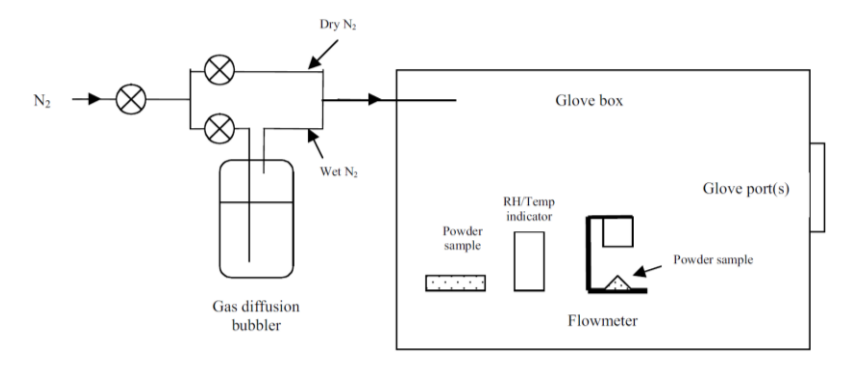


Figure 2.5: (a) Flow times of PS304 feedstock powders with 45 to 106 μ m angular and spherical BaF2-CaF2 particles as a function of percent relative humidity; (b) Flow times of PS304 feedstock with angular 45 to 53 μ m and 90 to 106 μ m; and (c) Experimental setup for controlled humidity powder flow tests [28].

2.2.3. Powder Rheometer: Stability and Variable Flow Rate test (Dynamic test)

This test obtains measurements from particles in motion. **Figures 2.6-a** and **2.6-b** shows an image for the instrument with four different set-up blades to hold different tests. As shown in **Fig. 2.6-c**, measurements of axial forces and rotational torques acting are performed [37, 40].

The stability and variable flow rate (VFR) test is defined as the resistance to motion of a specialized blade as it rotates downwards through a volume of conditioned powder through a definite pathway [37].

During the initial conditioned step, cell is split to remove any material above a bed height of 80 mm. As a result of that, total flow energy corresponds to a penetration depth of H = 70 mm (10 mm from the base) [40]. Experimental set-up was explained in detail by Hare et al. [40], where the vessel (50 mm diameter) with the impeller (48 mm diameter) was utilized. Standard test procedure was applied to the bed of particles, whereby the bed is initially conditioned by rotating the impeller clockwise to gently slice the bed surface and produce a reproducible, low stress packing state. Test is carried out with a tip speed of 100 mm/s and a helix angle of 5° .

Stability and variable flow rate (VFR) test can detect subtle differences between used and fresh powders. Where, processing has significantly increased the flow energy of the used powder [37]; as it shown in **Fig. 2.6-d**. According to a literature [41], three samples of stainless steel powder from same manufacture, which had same particle size distribution (PSD) and similar flowability response in the Hall flowmeter and angle of repose, showed different performances in AM process.

While powders A and B showed "acceptable behavior" during spreading, powder C caused poor deposition and blockages, and resulting in low-quality final parts. However, evaluating three samples with the powder rheometer highlighted several differences between powders A, and B that correlated well with the process performance.

Specific Energy (SE), i.e., one of the VFR tests available with the blade, **Fig. 2.6-b-1**, clearly differentiated powder *C* during dynamic testing, with the higher value indicating increased particle-particle friction and mechanical interlocking, in **Fig. 2.6-e**.

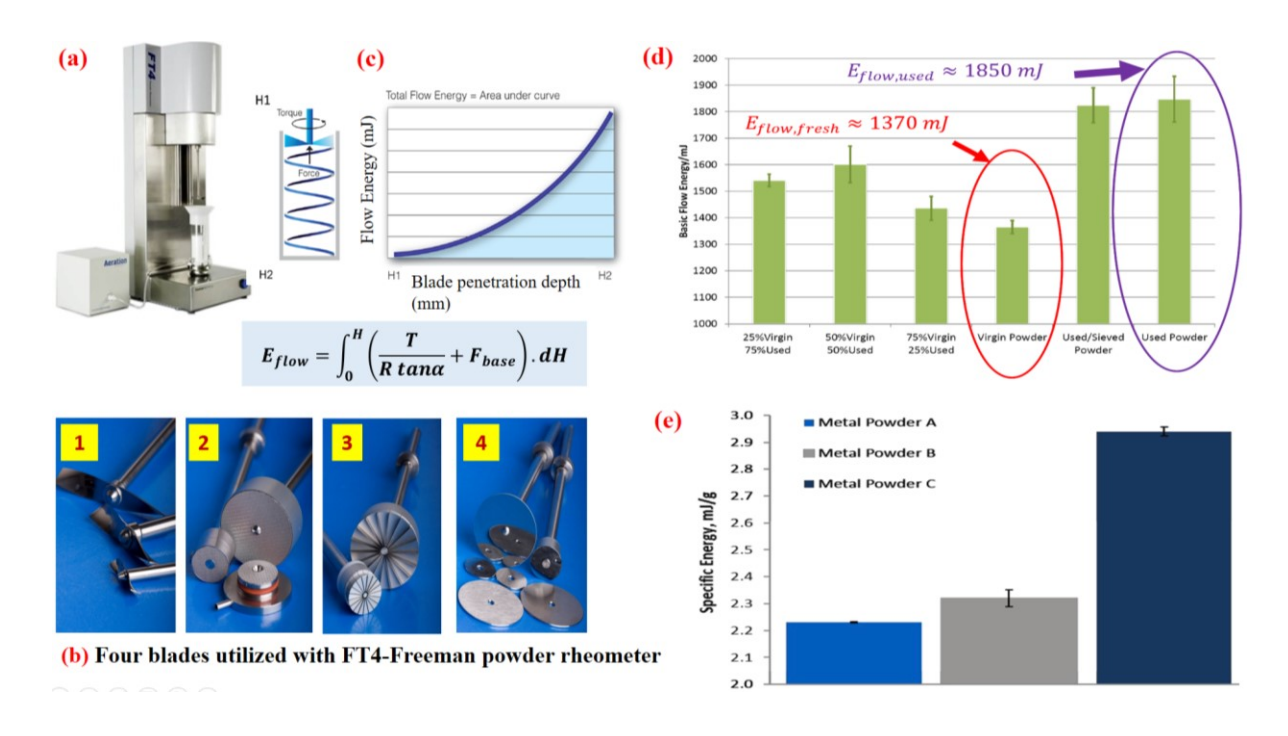


Figure 2.6: (a) Image for the FT4 powder rheometer set-up instrument, (b) four blades utilized with the rheometer, (c) principle of flow-energy diagram, (d) experiment measurements [37], and (e) experiment measurements [41].

2.3 Powder Spreading and Surface Characterization

For PBF, very thin powder layers are needed with 'good' layer properties, i.e. a high packing density with homogeneous surface texture. In order to achieve thin layers, fine powders are utilized extensively to form beds. Powder spreading characteristics are then dependant on the packing fraction of the bed and smoothness of the substrate, since high porosity, or rough surface might create weaker bonding between layers and poor mechanical properties of the printed part [4, 42].

Spreadability is affected by the van der Waals attractive forces, powder weight and humidity [6, 17]. It was reported by Choi et al. [4] that the powder layer density affects the density of 3D object, and the importance of layer compactness and smoothness for a new grade of polymer (PEEK) powder was shown by Berretta et al. [43]. Surface roughness of the powder bed, and surface quality of the part are strongly related. The solid volume fraction of a raw thermoplastic-elastomers powder, and porosity of sintered parts were also found to be connected [44]. Thus, a dense and homogeneous powder layer is advisable, and it is therefore important to have a good flow characteristic [4].

Figure 2.7 shows a variety of spreading devices [6,15,45]. Electron beam powder bed fusion (EB-PBF) is one style from the additive manufacturing processes. This printing method is preferable

for aerospace and implants medical applications because the vacuum minimizes impurities [2]. Besides industrial electron beam powder bed fusion (Arcam system), there are research activities on self-built EB-PBF machines, which have not reached the performance of Arcam system [5, 45, 46]. **Figure 2.1-b** shows a diagram of Arcam system with some process parameters and design detail. EBSM is a scientific name for electron beam selective melting machine developed by Guo et al. [45].

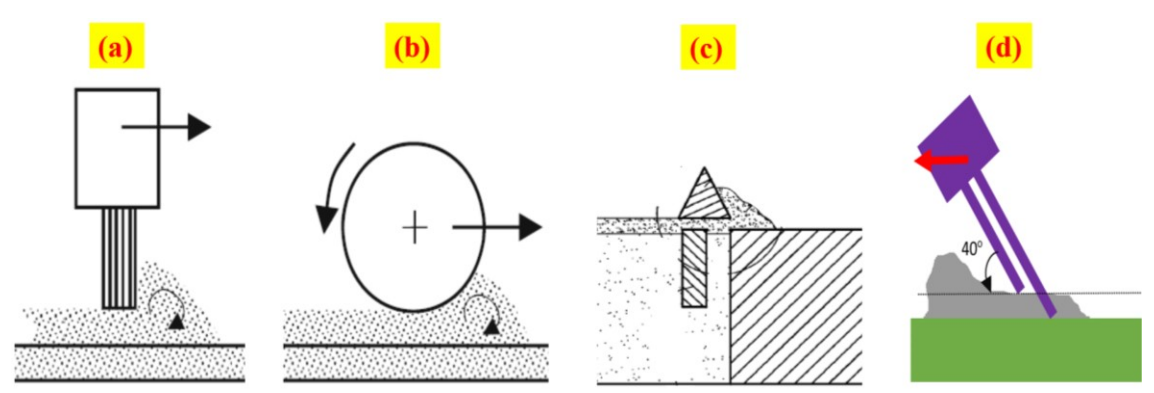


Figure 2.7: (a and b) schematic of AM spreading processes [6], (c) the cross section of one style of the industrial electron beam powder bed fusion (Arcam system) spreading system [15], and (d) dual-inclined combs for the EBSM Chinese system [45].

One of the outcomes of spreading is powder layer density, which strongly affects final part properties. Powder layer densities for two types of gas atomized 316L stainless steel powders, one which flowed and one which did not flow, were evaluated by Choi et al. [4] for three layer thicknesses, **Table 2.3**. It was found that both powders showed specific layer densities which had values between tapped and apparent densities and that powder layer density is independent of the layer thickness range used [4].

Table 2.3: A summary of all measured densities [4]

	Apparent	Tapped	Hall			
	density (g/cm ³)	density (g/cm ³)	Flowmeter (seconds/50g)	Layer Thickness (25 μm)	Layer Thickness (50 μm)	Layer Thickness (75 μm)
				Powder layer density (g/cm³)	Powder layer density (g/cm³)	Powder layer density (g/cm³)
Sample 1	4.45	5.04	17.13	4.62	4.56	4.65
Sample 2	4.08	4.88	No Flow	4.39	4.41	4.45

Granular materials often have a tendency to segregate owing to differences in particle properties, such as the shape, size, and density (e.g. smaller particles cluster together) [47]. The level of

segregation in a layer of powder might be taken as a measure of spreadability. Segregation for metallic powders in powder beds has, to the best of our knowledge, not been studied extensively. It was reported that powder particles according to their size distribution for AM segregated depending on the location in the machine [48]. Segregation in a powder bed was examined by Whiting and Fox [25]. They found a slight change in PSD at different elevations of the powder in the bulk containers and minor changes in PSD at different locations along the spreading direction of a loose powder bed. Significant differences in the particles collected from sides of solidified parts were reported.

In order to evaluate spreadability, the packing factor is introduced as a tool to compare powder spreading. Analysis of a single layer of powder for electron beam melting has not been investigated, but a powder bed parameter was distinguished by Van den Eynde et al. [49], where the effectiveness of the spreading process was indicated by the packing factor (\emptyset) , which is the ratio of single layer density to solid density [49].

$$\emptyset = \frac{\rho_{powder-bed-layer}}{\rho_{solid}}$$
 (2.5)

Tap density (ρ_{tap}) delivers an indication for flowability of a powder from measurements of the change in bulk density induced by one directional tapping [37].

Van den Eynde et al. [49] have defined the maximum packing factor (\emptyset_{max}) as the ratio of tap density to solid density for the same material. This ratio delivers the upper limit for the packing factor (\emptyset) and it is limited by particle geometry and size distribution [49].

$$\left(\emptyset_{max} = \frac{\rho_{tap}}{\rho_{solid}}\right) \ge \left(\emptyset = \frac{\rho_{powder-bed-layer}}{\rho_{solid}}\right)$$
 (2.6)

According to the above, the packing factor (Ø) is an index for the packing quality of a single powder layer in PBF; higher packing factor will lead to a denser sintered part [37].

2.4 Tribocharging

Although tribocharging or triboelectrification is one of the earliest phenomena observed in natural science, studied by some famous scientists, such as Cavendish, Faraday, and Franklin, a quantitative analysis for tribocharging has not been obtained [50].

Tribocharging is existed whenever two surfaces rub, roll or slide on each other [51]. The resulting charges on both surfaces provide electrostatic forces at the interaction regions [52]. The electrostatic forces attract the surfaces as a result of oppositely charged regions [53].

Although, research in the tribocharging field has progressed during the recent years, the mechanism of triboelectrification has not well discovered. The influence of different process parameters could affect the charge exchange and generate different charging mechanisms. In fact, the hazardous (ignition of dust in a flammable atmosphere, or electrostatic damage in the semiconductor chip), and benefits (powder coating, electrostatic separation of minerals and electro-photography) aspects of tribocharging have been considered in literature [54].

In the literature, the set of experiments on tribocharging of metals is very limited. Moreover, the role of oxide layer at the metal's surface has not clearly defined for the charge exchange. After contacts between surfaces, the measured charge was linearly related to the contact potential differences (driving forces) measured in the same experiment, and the quantum mechanical tunneling of electrons would define the charge exchange [54].

If two materials are rubbed against each other, their surfaces exchange electrons. After the two materials are separated, the material with the stronger affinity for negative charge will be charged negatively (gain electrons). The other material will have an equal positive charge (lose electrons) [55].

Tribocharging is affected by the environmental conditions such as relative humidity and temperature [56]. Greason [57] measured the charge on a metal sphere with a Faraday cage after contact with an insulating material under various conditions. The charge increased with decreasing relative humidity at a definite temperature. When the relative humidity was low, the charge decreased with increasing temperature [57]. If the charged particles were maintained at a high relative humidity, the charge decreased quickly [58].

Freeman and March [59] reported the triboelectric series of different materials in **Table 2.4**, where the order in the list could be changed due to the condition of surfaces and frictional forces.

Asbestos and Teflon were specified as the most electro-positive and electro-negative materials, respectively. When two of the listed materials in **Table 2.4** were rubbed together, the upper material in the series gained a negative charge and the lower one became positive [59].

Although **Table 2.4** listed some materials (metals, alloys, ceramics, and polymers), this table did not mention the tribocharging behavior for important alloys and metals for additive manufacturing processes, such as Inconel 718, commercial purity titanium CP-Ti, Ti-6Al-4V, and aluminum alloy A357. For this reason, one of the research objectives was to identify the location of the mentioned alloys at the modified triboelectric series.

The tribocharging is classified into three categories: (i) metal/metal, (ii) metal/insulator and (iii) Insulator/insulator contacts [60]. For this research, the third category will not be considered.

2.4.1. Metal/Metal Contact

If metal A with a work function γ_A (eV) and metal B with a work function γ_B (eV) were brought into contact and then separated. To maintain the thermodynamic equilibrium, the contact surfaces exchanged electrons by tunneling [61]. If e was the elementary charge, a contact potential difference V_C across the interface was defined by Supuk et al. [60]:

$$V_C = \frac{\gamma_B - \gamma_A}{e} \qquad (2.7)$$

If C_{AB} was the contact capacitance [Farad] [61]; the charge after separation q was calculated by the following equation:

$$q = C_{AB} V_C \qquad (2.8)$$

When surface B separated from surface A, the q and C_{AB} decreased and the charge exchange by tunneling stopped. Thus, the cutoff of tunneling current was with 1 nm distance.

For a sphere plane geometry, z was the separation's distance when the tunneling stopped, r was the radius of sphere and ε_o was the vacuum permittivity.

Table 2.4: Triboelectric series [59]; the bold and underline materials listed are important for this research

More Negative (-)						
Teflon						
Silicon						
Polyvinylchloride						
Polyethylene						
Polystyrene						
Cellulose Acetate (Rayon)						
Sulphur						
Gold, Platinum						
<u>Nickel</u> , Copper						
Natural Rubber (Latex)						
Amber						
Borosilicate glass, ground surface						
Wood						
<u>Steel</u> , Iron						
Cotton						
<u>Aluminum</u>						
Silk						
Silica (fire polished)						
Wool						
Nylon						
Mica						
Window glass						
Borosilicate glass (fire polished)						
Silicone elastomer with silica filler						
Rabbit fur						
Asbestos						
More Positive (+)						

Harper [61] derived the following equation, where C_{AB} was a function of the distance Z:

$$C_{AB} = 4\pi\varepsilon_o r \left(0.577 + \frac{1}{2} \ln\left(\frac{2r}{z}\right)\right) \quad (2.9)$$

If the tunneling cutoff distance was $(z_1 = 1 \times 10^{-9} meter)$, a "semi-quantitative" agreement between experiment and theory was obtained [61].

For rough surfaces, the two surfaces were separated by much larger distances when the closest point of separation was at z_1 . A good quantitative agreement between the metal/metal charging experiment and theory was obtained with $(z_2 \approx 100 \times 10^{-9} meter)$ [62].

The metal/metal charging experiments which was obtained by Harper [61] and Lowell [62], had metal balls of different diameters and contacted only once under controlled pressure [63].

Kwetkus and Sattler [54] obtained tribocharging experiments for oxidized metals and gold under high vacuum conditions. The oxidized metal powder samples of (Ni, Cr, Nb and La) were contacted with a gold plate, while the transfer of charge was detected on the gold plate and samples, Fig. 2.8.

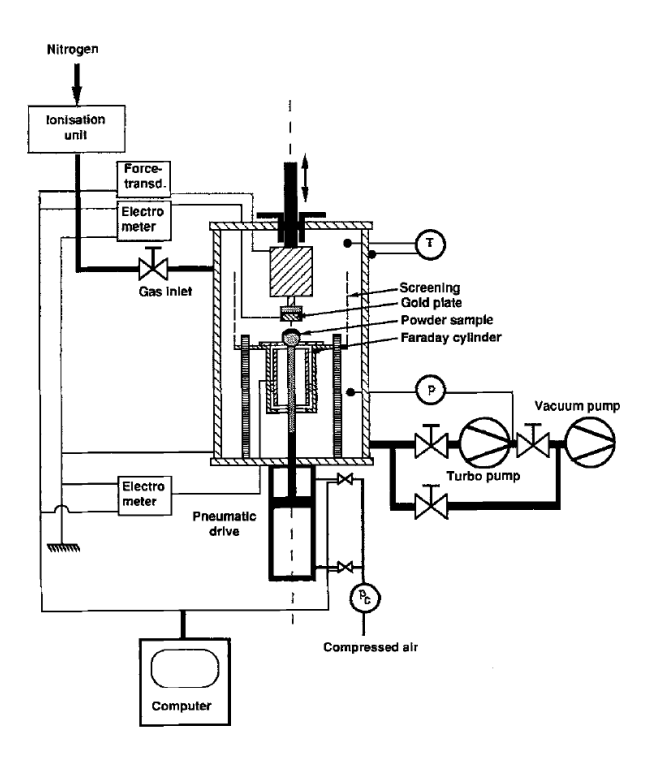


Figure 2.8: Scheme of the apparatus used by Kwetkus and Sattler [54]

Figure 2.9 shows the charge acquired by nickel powder after repeated contacts with the gold plate (Ni/Au). At the 1st contact, nickel powder charged positive (saturation value), and this charge kept constant with further contacts. On the other hand, the gold plate charged negative.

Based on the triboelectric series in **Table 2.4**, when nickel and gold were rubbed together, gold (the upper material in the series) gained a negative charge and nickel (the lower material in the series) became positive.

The agreement between the result obtained by Kwetkus and Sattler [54] and the triboelectric series [59] might help to predict the charging behavior for other alloys and metals.

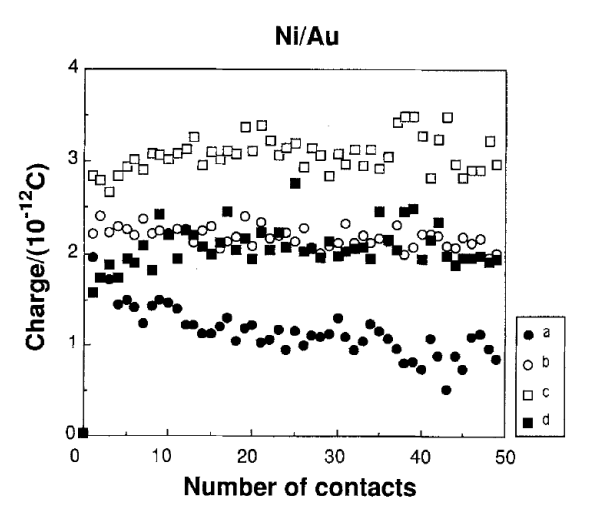


Figure 2.9: Charging curves for Ni powder plotted with respect to number of contacts [54]

Figure 2.10 presented the contact electrification curves for Cr/Au, Nb/Au and La/Au. At the 1st contact, the powders reached a "saturation charge".

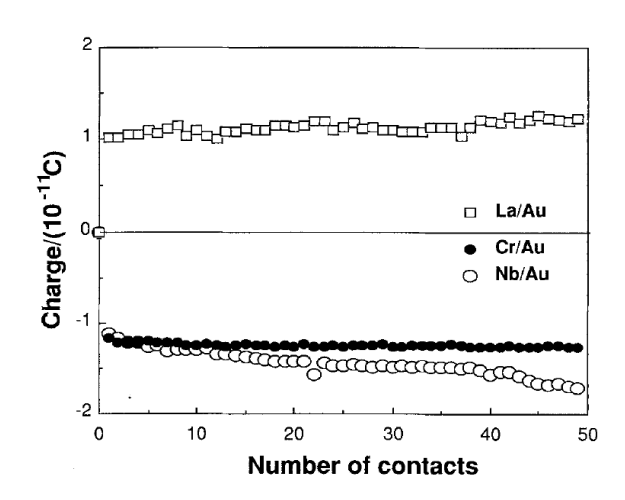


Figure 2.10: Charging curves for La, Cr and Nb powder plotted with respect to the number of contacts [54].

From Fig. 2.10, lanthanum charged positively ($+1 \times 10^{-11}$ coulomb) in contact with gold which charged negatively (gained electrons) [54].

This result was compared with the triboelectric series in **Table 2.4**, where lanthanum was not mentioned, and nickel had a charging value of $(+0.3 \times 10^{-11} \text{ coulomb})$. The first material is located further away from second material on the list, a greater charging value will be transferred during the tribocharging process. The proposed location of lanthanum was below the nickel at the modified triboelectric series, **Table 2.5**.

Chromium and niobium charged negatively after contacted by gold as shown in **Figure 2.10**. These results were compared with the triboelectric series in **Table 2.4**, where both metals were not mentioned. As a result of the fact that both metals charged negative, chromium and niobium should be located above the gold at the modified triboelectric series [54], **Table 2.5**.

Also, the saturation charges for chromium and niobium were $(-1.1 \times 10^{-11} \text{ coulomb})$ and $(-1.5 \times 10^{-11} \text{ coulomb})$, respectively. This indicated that niobium was located above chromium at the modified triboelectric series in **Table 2.5**.

The previous observations helped to distinguish the possible tribocharging effects for nickel and chromium, which are essential constituents for the Nickel-based superalloys.

Table 2.5: The modified triboelectric series based on Kwetkus and Sattler [54] work.

More Negative (-)
Niobium (Nb)
Chromium (Cr)
Gold (Au)
Nickel (Ni)
Lanthanum (La)
More Positive (+)

According to the standard specification for additive manufacturing nickel alloy with powder bed fusion ASTM F3055-14a, Inconel 718 is consisted of the following constituents (**Table 2.6**), where nickel and chromium have the highest weight percentages.

Table 2.6: The constituents of Inconel 718 based on ASTM F3055-14a.

Element	Weight Percentage %		
Nickel	maximum = 50 - 55		
Chromium	range = 17 - 21		
Carbon	maximum = 0.08		
Manganese	maximum = 0.35		
Silicon	maximum = 0.35		
Phosphorus	maximum = 0.015		
Sulfur	maximum = 0.015		
Cobalt	maximum = 1.0		
Molybdenum	range = $2.80 - 3.30$		
Tantalum + Niobium	range = $4.75 - 5.50$		
Titanium	range = $0.65 - 1.15$		
Aluminium	range = $0.20 - 0.80$		
Copper	maximum = 0.3		
Boron	maximum = 0.006		
Iron	Balance		
Oxygen	not specified		
Nitrogen	not specified		

With the assistance of powder rheometer, the tribocharging behavior of Inconel 718 and its location at the triboelectric series are delivered in chapters 6 and 7.

Based on the results of Kwetkus and Sattler [54], the tribocharging phenomenon for metallic powders occurs in vacuum, and it might affect powder spreadability at the powder bed electron beam fusion process.

2.4.2. Metal/Insulator contact

For a metal/ insulator contact, the transfer of charges was explained by a similar hypothesis of the metal/ metal electron transfer with the assumption of an "effective work function" was assigned to the insulator [56]. The charge after separation q was calculated by the following equation:

$$q = C_M \frac{\gamma_{Metal} - \gamma_{Insulator}}{e}$$
 (2.10)

where, the effective capacitance C_M was related to the characteristics of insulator. Also, γ_{Metal} and $\gamma_{Insulator}$ were the effective work functions of metal and insulator, respectively.

During friction mechanism between metal/insulator surfaces, the possible material transfer from a surface to the other, such as fragments of the bodies, contaminated small dusts or surface impurities, might be able to move charges [64]. Nevertheless, there is no mathematical model of charge transfer and its equilibrium state based on the material transfer mechanism [56].

2.5 Size-Dependent Same-Material Tribocharging

Tribocharging can be generated by interaction between particles made of the same material [65]. Same-material tribocharging has been recorded at some natural phenomena (dust storms [66]) and industrial applications (pneumatic conveying [67]).

Some observations showed that the mechanism for same-material tribocharging in powders is related to particle size distribution (PSD). Where, smaller powder particles will be charged negatively, and larger particles will be charged positively [68, 69].

Zhao et al. [70] reported a trend for different powders when the charge to mass ratio for a sample traversed from positive to negative as the particle diameter decreased.

The following set of experiments for same-material polymeric tribocharging was prepared by Lowell and Truscott [71]; where, polytetrafluoroethylene (PTFE), polystyrene and polymethylmethacrylate (PMMA) were used to make spherical particles and planes. A spherical particle slid over the plane of the same material in vacuum and atmospheric pressure, and the total charge transferred to the plane as a function of sliding distance was measured.

2.5.1 Same-Material Tribocharging and Segregation

Segregation of powder particles might have a huge impact at the process. For instance, it could be necessary to separate materials in a process, but a source of instability in other process [72].

Alchikh-Sulaiman et al. [29, 47] demonstrated that the mixing of polydisperse powder particles at the rotary drum and slant cone mixers were combined with segregation mechanisms. If, powders with different particle size distributions are mixed by any mixer, segregation is combined with mixing.

Mixing for powders is based on three mechanisms: convective, shear and diffusive [73]. On the other hand, powders often have a tendency to segregate owing to differences in particle properties, such as the shape, size, and density (e.g. smaller particles cluster together) [47].

If powders have different densities or particle size distributions, it is often difficult to mix them homogeneously due to density segregation or size segregation [74]. Where, recent studies specified that the main reason for segregation of powder particles is the particle size difference [29, 47, 75].

The following 13 segregation mechanisms were defined in the literature: rolling, concentration-driven displacement, agglomeration, sieving, displacement, trajectory, percolation, angle of repose, air current, push-away, embedding, fluidization and impact-bouncing [76 - 79].

The sieving segregation, which belongs to the top to bottom segregation, has the following pattern: the small particles relatively move down while the large particles move up. Also, percolation and displacement segregations can be considered as special cases of the sieving segregation [80].

Four segregation mechanisms based on the particle size distribution were proposed by Tang and Puri [80]: (i) side-to-side (large particles), (ii) sieving (small particles), (iii) agglomeration (cohesive fine) and (iv) fluidization (fine). Moreover, the side-to-side segregation is named the trajectory since the small particles relatively move in a direction while the large particles move in the other direction [80].

Forward et al. [81] observed charge segregation for a bimodal system, where this segregation relied on the proportion of the particle sizes. In other words, the segregation was discussed as a result of same-material bipolar charging phenomenon.

Powders at the presence of shear forces will self-organize into separate regions where particles with similar density, particle size, shape or surface characteristics [82, 83]. This observation needs to be addressed according to the same-material tribocharging phenomenon. For a process, the segregation of metallic powder particles due to particle size should take in account the bipolar charging, where smaller particles will become negatively charged and larger particles will become positively charged.

The tribocharging effect on the homogeneity of powder blending was examined by Pu et al. [84] for binary mixtures. It was found that the minimization, or the elimination if it is possible, of the electrostatic charges can disturb the homogeneity of the mixture. On the other hand, the segregation phenomenon for the rotary drum is induced by vertical and horizontal mechanical vibration flow [79].

During the stability and variable flow rate (VFR) test, segregation occurred when smaller particles moved and stored on the back surface of the impeller due to the downward and upward cycles. The segregation patterns inside the powder rheometer, the larger particles stayed at the upper section of the powder column. On the other hand, smaller particles occupied the lower section of the column and filled the upper side of the impeller [72]. Based on this analysis, the segregation mechanism during the VFR test was sieving. Thus, the existence of tribocharging effect for metallic powder in the powder rheometer should be expected due to the correlation between segregation and same-material tribocharging.

2.6 White Light Interferometry (WLI)

During this research, the surface characteristics and parameters have been measured with the assistance of white-light interferometry. For this reason, the principle and important elements of this technology were provided.

The white-light interferometry, or also named the coherence scanning interferometry (CSI), is a known technique of optical surface metrology utilizing low temporal coherence light, such as the solid-state light emitting diode or a tungsten-halogen lamp [85, 86].

To characterize a surface with this technology, two steps will take place in-order. (i) Beam splitter divides light beam into two paths, one goes to the measured surface and the other to Mirau interferometer. (ii) The two beams are reflected to splitter and joined to generate interference fringes. A charge-coupled device camera records those fringes and surface characterization is produced from interference pattern. Along the z-axis, the constructive fringes at specific location produce the related surface's height. Whereas variations of constructive fringes along the surface delivers information about roughness of the measured surface [87].

Mirau alone is not an instrument, but rather a specific class of objective which changes any microscope into an interferometer [85]. In fact, Mirau interferometer involves the microscope objective, semitransparent and reference mirrors [87].

Where, the reference mirror consists of a small metallic coating on a transparent reference plate [85]. **Figure 2.11** provides a schematic diagram of the WLI with Mirau interferometer [88].

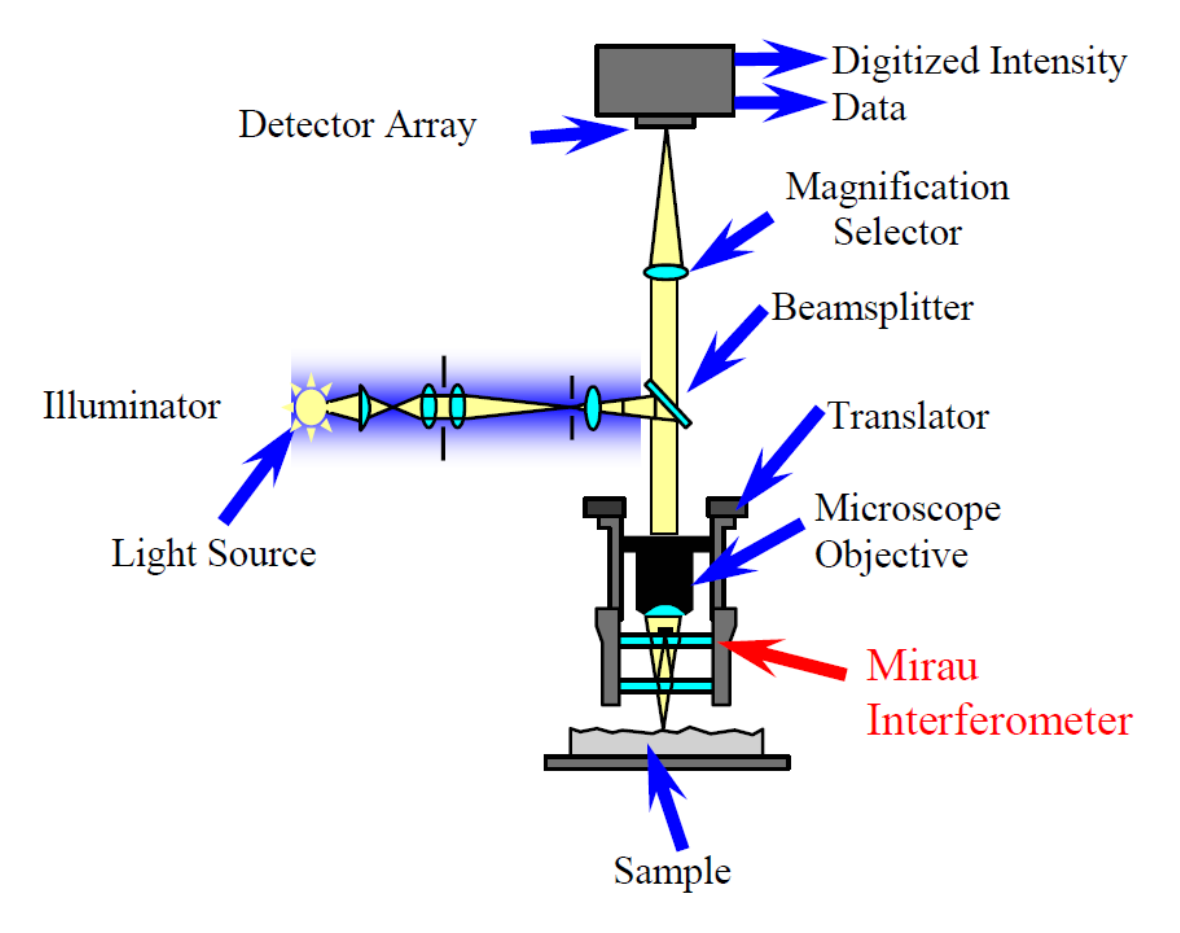


Figure 2.11: A schematic diagram of the WLI used to measure the surface features with Mirau interferometer [88].

Noncontact optical profilometry (ZygoTM NewView 8000) using scanning white-light interferometry offers a rapid and reliable as well as convenient way of performing surface roughness measurements, characterizations of the contact-sintered and sintered titanium powder in a puck, powder thickness, and large area image stitching with superior 3D surface visualization. The optical surface profile provides a fast, reliable, and non-contact measurements. All measurements are non-destructive and require no sample preparation [87]. Along the z-axis in non-contact method, white-light-interferometry requires scanning the surface, and computing the degree of coherence (visibility of interference fringes) at every pixel in the image [89].

Three different objective lenses, with magnifications of 50x, 10x and 2.75x were provided with the Zygo 8000 and combined with 0.5x and 2.0x zoom lenses. In addition, the 2.75x Michelson and 10x Mirau objective lenses were utilized to scan complete contact-sintered surfaces and to measure height-profiles for defined slices with a higher magnification, respectively.

For a specific application, the selection of an interference objective depends on many factors including the field of view, which is determined by camera format, objective magnification and zoom lens. Also, the working distance and lateral resolution for 10x Mirau are 7400 µm and 0.86 µm, respectively [85]. On the other hand, measuring a highly shiny surface with scattering features (high reflectivity variations) can disturb the measurement accuracy for the WLI, and to generate poor results [90].

2.7 Conclusions

A comprehensive literature review for powder characterization, powder flowability and spreadability has been presented. The classical flowability tests (angle of repose, Hall flowmeter, etc.) and the recent flow instruments (revolution analyzer and FT4 Freeman powder rheometer) were reviewed with respect to their internal stresses and flow mechanism.

The main differences between powder spreadability and flowability for additive manufacturing powder bed fusion (AM-PBF) processes were distinguished. In addition, powder flow and spreading can be controlled by these forces; friction forces, adhesive forces and coulombic forces (van der Waals forces, electrostatic and tribocharging).

The packing factor was utilized as a tool to evaluate spreadability, and its maximum value (upper limit) was discussed. For electron beam powder bed fusion (EB-PBF) process, the available industrial spreading mechanisms in the market were presented. Finally, the theoretical background for tribocharging between different materials and same-material bipolar charging were discussed in detail.

References

- [1] Y. Sun, S. Gulizia, C. Oh, C. Doblin, Y. Yang, and M. Qian, "Manipulation and characterization of a novel titanium powder precursor for additive manufacturing applications," *The Minerals, Metals & Materials Soc.*, vol. 67, pp. 564-572, 2015.
- [2] G. Baudana, S. Biamino, D. Ugues, M. Lombardi, P. Fino, M. Pavese, and C. Badini, "Titanium aluminides for aerospace and automotive applications processed by electron beam melting: contribution of Politecnico di Torino," *Metal Powder Report*, vol. 71, pp. 193-199, 2016.
- [3] C. Aumund-Kopp and A. Riou, *Introduction to Additive Manufacturing Technology: A guide for Designers and Engineers*, 2nd ed. Shrewsbury, UK: EPMA, 2018.
- [4] J. P. Choi, G. H. Shin, H. S. Lee, D. Y. Yang, S. Yang, C. W. Lee, M. Brochu, and J. H. Yu, "Evaluation of powder layer density for the selective laser melting (SLM) process," *Mater. Trans.*, vol. 58, pp. 294-297, 2017.
- [5] C. Körner, "Additive manufacturing of metallic components by selective electron beam melting, a review," *Inter. Materials Rev.*, vol. 61, pp. 361-377, 2016.
- [6] A. B. Spierings, M. Voegtlin, T. Bauer, and K. Wegener, "Powder flowability characterization methodology for powder-bed-based metal additive manufacturing," *Prog. Addit. Manuf.*, vol. 1, pp. 9-20, 2016.
- [7] A. Klassen, T. Scharowsky, and C. Korner, "Evaporation model for beam based additive manufacturing using free surface lattice Boltzmann methods," *J. Phys. D: Appl. Phys.*, vol. 47, pp. 1-12, 2014.
- [8] H. P. Zhu, Z. Y. Zhou, R. Y. Yang, and A. B. Yu, "Discrete particle simulation of particulate systems: a review of major applications and findings," *Chem. Eng. Sci.*, vol. 63, pp. 5728-5770, 2008.
- [9] Z. Xiang, M. Yin, Z. Deng, X. Mei, and G. Yin, "Simulation of forming process of powder bed for additive manufacturing," *J. Manuf. Sci. Eng.*, vol. 138, pp. 081002, 2016.
- [10] U. Ackelid, M. Svensson, P. Gennaro, M. Filippini, S. Beretta, S. Biamino, A. Penna, M. Pavese, S. Marchisio, P. Fino and C. Badini, "Additive Manufacturing of Gamma Titanium Aluminide Parts by Electron Beam Melting EBM," *Presentation session presented. Titanium 2010 conference, Orlando, FL, 2010.*
- [11] D. Schulze, *Powders and Bulk Solids: Behavior, Characterization, Storage and Flow.* Berlin, Germany: Springer-Verlag Berlin Heidelberg, 2008.

- [12] V. Ganesan, K. A. Rosentrater, and K. Muthukumarappan, "Flowability and handling characteristics of bulk solids and powders-a review with implications for DDGS," *Biosystems Eng.*, vol. 101, pp. 425-435, 2008.
- [13] A. Santomaso, P. Lazzaro, and P. Canu, "Powder flowability and density ratios: the impact of granules packing," *Chem. Eng. Sci.*, vol. 58, pp. 2857-2874, 2003.
- [14] G. Berkebile, K. Creehan, S. Deutsch, R. Gorham, E. Morris, H. Cheung, S. Doucet, J. F. Forte, I. Kiselyer, J. McCabe, L. Neiman, L. Rajchel, F. Schrotter, M. Voizard, and D. Wiser, "Standardization roadmap for additive manufacturing," National Additive Manufacturing Innovation Institute (America Makes), and American National Standards Institute (ANSI), Ohio, USA, 2017.
- [15] L. Loewgren and M. Wildheim, "Method for improved powder layer quality in additive manufacturing", U.S. Patent 2016/0129501 A1, May 12, 2016.
- [16] E. Parteli and T. Pöschel, "Particle-based simulation of powder application in additive manufacturing," *Powder Tech.*, vol. 288, pp. 96-102, 2016.
- [17] J. Clayton, J. Dawes, and C. Langley, "Optimizing metal powders for additive manufacturing: exploring the impact of particle morphology and powder flowability," *additivemanufacturing.media*, May 26, 2017. [Online]. Available: http://www.additivemanufacturing.media/blog/post/optimizing-metal-powders-for-additive-manufacturing-exploring-the-impact-of-particle-morphology-and-powder-flowability. [Accessed Sept. 20, 2017].
- [18] G. Berkebile, K. Creehan, S. Deutsch, R. Gorham, E. Morris, H. Cheung, S. Doucet, J. F. Forte, I. Kiselyer, J. McCabe, L. Neiman, L. Rajchel, F. Schrotter, M. Voizard and D. Wiser, "Standardization roadmap for additive manufacturing," National Additive Manufacturing Innovation Institute (America Makes), and American National Standards Institute (ANSI), Ohio, USA, 2018.
- [19] R. German, *Powder Metallurgy Science*. Princeton, NJ: Metal Powder Industries Federation, 1984.
- [20] N. Pohlman, J. Roberts, and M. Gonser, "Characterization of titanium powder: microscopic views and macroscopic flow," *Powder Tech.*, vol. 228, pp. 141-148, 2012.
- [21] A. Bauereiß, T. Scharowsky, and C. Körner, "Defect generation and propagation mechanism during additive manufacturing by selective beam melting," *J. Mater. Proc. Tech.*, vol. 214, pp. 2522-2528, 2014.

- [22] C. McCracken, C. Motchenbacher, and R. Deeter, "Plasma Spheroidized Titanium Powders," *cdn.ymaws.com*, Oct. 7, 2012. [Online]. Available: https://cdn.ymaws.com/titanium.org/resource/resmgr/2010_2014_papers/McCrackenColin_2012.pdf. [Accessed April. 17, 2017].
- [23] F. Amado, M. Schmid, G. Levy, and K. Wegener, "Advances in SLS powder characterization,": *Proceedings of the Annual International Solid Freeform Fabrication Symposium, Austin, TX, USA, August 8-10, 2011, D.L. Bourell, R.H. Crawford, C.C. Seepersad, J.J. Beaman, H. Marcus, Ed. Austin: The University of Texas at Austin, 2011. pp. 3-5.*
- [24] B. Liu, R. Wildman, C. Tuck, I. Ashcroft, and R. Hague, "Investigation the effect of particle size distribution on processing parameters optimization in selective laser melting process," : *Proceedings of the Annual International Solid Freeform Fabrication Symposium, Austin, TX, USA, August 8-10, 2011,* D.L. Bourell, R.H. Crawford, C.C. Seepersad, J.J. Beaman, H. Marcus, Ed. Austin: The University of Texas at Austin, 2011. pp. 227-238.
- [25] J. Whiting and J. Fox, "Characterization of feedstock in the powder bed fusion process: sources of variation in particle size distribution and the factors that influence them,": *Proceedings of the 26th Annual International Solid Freeform Fabrication Symposium, Austin, TX, USA, August 8-10, 2016,* D.L. Bourell, R.H. Crawford, S. Fish, J.J. Beaman, H. Marcus, Ed. Austin: The University of Texas at Austin, 2016. pp. 1-12.
- [26] A. B. Spierings, N. Herres and G. Levy, "Influence of the Particle Size Distribution on Surface Quality and Mechanical Properties in Additive Manufactured Stainless Steel Parts,": *Proceedings of the 21st Annual International Solid Freeform Fabrication Symposium, Austin, TX, USA, August 29-31, 2010,* D.L. Bourell, R.H. Crawford, C.C. Seepersad, J.J. Beaman, H. Marcus, Ed. Austin: The University of Texas at Austin, 2010. pp. 1-10.
- [27] R. Freeman, "Measuring the flow properties of consolidated, conditioned and aerated powders-a comparative study using a powder rheometer and a rotational shear cell," *Powder Tech.*, vol. 174, pp. 25-33, 2007.
- [28] M. K. Stanford and C. DellaCorte, "Effects of humidity on the flow characteristics of PS304 plasma spray feedstock powder blend," NASA center for aerospace information, Hanover, MD, May 2002.
- [29] B. Alchikh-Sulaiman, F. Ein-Mozaffari, and A. Lohi, "Evaluation of poly-disperse solid particles mixing in a slant cone mixer using discrete element method," *Chem. Eng. Res. Des.*, vol. 96, pp. 196-213, 2015.
- [30] A. Adler, "Flow properties of metal powders," *Intern. J. Powder Meta.*, vol. 5, pp. 7-20, 1969.

- [31] A. Bodhmage, "Correlation between physical properties and flowability indicators for fine powders," Ph.D. dissertation, Dept. Chem. Eng., University of Saskatchewan, Saskatoon, SK, 2006.
- [32] M. R. Shishir, F. S. Taip, N. A. Aziz, and R. A. Talib, "Physical properties of spray-dried pink guava (Psidium guajava) powder," *Agriculture and Agricultural Science Procedia*, vol. 2, pp. 74-81, 2014.
- [33] T. Hao, "Understanding empirical powder flowability criteria scaled by Hausner ratio or Carr index with the analogous viscosity concept," *RSC Advances*, vol. 5, pp. 57212-57215, 2015.
- [34] J. L. Soh, C. V. Liew, and P. W. Heng, "New indices to characterize powder flow based on their avalanching behavior," *Pharmaceutical Development and Technology*, vol. 11, pp. 93-102, 2006.
- [35] J. Cain, "An alternative technique for determining ANSI/CEMA standard 550," *Powder Handling & Processing*, vol. 14, pp. 218-220, 2002.
- [36] G. S. Riley, S. Mann, and R. O. Jesse, "Angle of repose of cohesive powders," *J. Powder & Bulk Solids Tech.*, vol. 2, pp. 15-18, 1978.
- [37] J. Clayton and R. Deffley, "Optimizing metal powders for additive manufacturing," *Metal Powder Rep.*, vol. 69, pp. 14-17, 2014.
- [38] A. Castellanos, J. M. Valverde, A. T. Perez, A. Ramos, and P. k. Watson, "Flow regimes in fine cohesive powders," *Physical Review Letters*, vol. 8, pp. 1156-1159, 1999.
- [39] H. Gu, H. Gong, J. J. Dilip, D. Pal, A. Hicks, H. Doak, and B. Stucker, "Effects of powder variation on the microstructure and tensile strength of Ti-6Al-4V parts fabricated by selective laser melting,": *Proceedings of the 25th Annual International Solid Freeform Fabrication Symposium, Austin, TX, USA, August 10-12, 2014*, D.L. Bourell, R.H. Crawford, S. Fish, J.J. Beaman, H. Marcus, Ed. Austin: The University of Texas at Austin, 2014. pp. 470-483.
- [40] C. Hare, U. Zafar, M. Ghadiri, T. Freeman, J. Clayton, and M. J. Murtagh, "Analysis of the dynamics of the FT4 powder rheometer," *Powder Tech.*, vol. 285, pp. 123-127, 2015.
- [41] AZO materials and Freeman Technology, "Additive manufacturing using powder rheometry to improve print quality," 9 December 2016. [Online]. Available: https://www.azom.com/article.aspx?ArticleID=13391. [Accessed: Oct. 11, 2018].
- [42] S. Haeri, Y. Wang, O. Ghita, and J. Sun, "Discrete element simulation and experimental study of powder spreading process in additive manufacturing," *Powder Tech.*, vol. 306, pp. 45-54, 2016.

- [43] S. Berretta, O. Ghita, and K. Evans, "Morphology of polymeric powders in laser sintering (LS): from Polyamide to new peek powders," *European Polymer J.*, vol. 59, pp. 218-229, 2014.
- [44] S. Ziegelmeier, P. Christou, F. Wollecke, C. Tuck, R. Goodridge, R. Hague, E. Krampe, and E. Wintermantel, "An experimental study into the effects of bulk and flow behavior of laser sintering polymer powders on resulting part properties," *J. Mater. Proc. Tech.*, vol. 215, pp. 239-250, 2015.
- [45] C. Guo, F. Lin, W. J. Ge and J. Zhang, "Development of novel EBSM system for high-tech material additive manufacturing research,": *Proceedings of the 25th Annual International Solid Freeform Fabrication Symposium, Austin, TX, USA, August 10-12, 2014,* D.L. Bourell, R.H. Crawford, S. Fish, J.J. Beaman, H. Marcus, Ed. Austin: The University of Texas at Austin, 2014. pp. 298-308.
- [46] C. Guo, W. Ge, and F. Lin, "Dual-material electron beam selective melting: hardware development and validation studies," *Engineering*, vol. 1, pp. 124-130, 2015.
- [47] B. Alchikh-Sulaiman, M. Alian, F. Ein-Mozaffari, A. Lohi and S. R. Upreti, "Using the discrete element method to assess the mixing of polydisperse solid particles in a rotary drum," *Particuology*, vol. 25, pp. 133-142, 2016.
- [48] J. A. Slotwinski, E. J. Garboczi, P. E. Stutzman, C. F. Ferraris, S. S. Watson, and M. A. Peltz, "Characterization of metal powders used for additive manufacturing," *Journal of Research of the National Institute of Standards and Technology*, vol. 119, pp. 460-493, 2014.
- [49] M. Van den Eynde, L. Verbelen, and P. Van Puyvelde, "Assessing polymer powder flow for the application of laser sintering," *Powder Tech.*, vol. 286, pp. 151-155, 2015.
- [50] S. Trigwell, N. Grable, C. U. Yurteri, R. Sharma, and M. K. Mazumder, "Effects of surface properties on the tribocharging characteristics of polymer powder as applied to industrial processes," *IEEE Transactions on Industry applications*, vol. 39, pp. 79-86, 2003.
- [51] A. F. Diaz and R. M. Felix-Navarro, "A semi-quantitative tribo-electric series for polymeric materials: the influence of chemical structure and properties," *J. Electrostatics*, vol. 62, pp. 277-290, 2004.
- [52] R. G. Horn and D. T. Smith, "Contact electrification and adhesion between dissimilar materials," *Science*, vol. 256, pp. 362-364, 1992.
- [53] T. A. Burgo, C. A. Silva, L. B. Balestrin, and F. Galembeck, "Friction coefficient dependence on electrostatic tribocharging," *Sci. Rep.*, vol. 3, pp. 1-8, 2013.

- [54] B. A. Kwetkus and K. Sattler, "Contact charging of oxidized metal powders," *Z. Phys. B Condensed Matter*, vol. 82, pp. 87-93, 1991.
- [55] B. Lee and D. Orr, "The TriboElectric Series,". *alphalabinc.com*, 2018. [Online]. Available: https://www.alphalabinc.com/triboelectric-series/. [Accessed July 14, 2019].
- [56] S. Matsusaka, H. Maruyama, T. Matsuyama, and M. Ghadiri, "Triboelectric charging of powders: A review," *Chemical Engineering Science*, vol. 65, pp. 5781-5807, 2010.
- [57] W. D. Greason, "Investigation of a test methodology for triboelectrification," *Journal of Electrostatics*, vol. 49, pp. 245-256, 2000.
- [58] T. Nomura, T. Satoh, and H. Masuda, "The environment humidity effect on the tribocharge of powder," *Powder Tech.*, vol. 135, pp. 43-49, 2003.
- [59] G. Freeman and N. March, "Triboelectricity and some associated phenomena," *Mater. Sci. Tech.*, vol. 15, pp. 1454-1458, 1999.
- [60] E. Supuk, C. Seiler, and M. Ghadiri, "Analysis of a simple test device for tribo-electric charging of bulk powders," *Part. Syst. Charact.*, vol. 26, pp. 7-16, 2009.
- [61] W. R. Harper, "The volta effect as a cause of static electrification," *Proc. R. Soc. Lond. A*, vol. 205, pp. 83-103, 1951.
- [62] J. Lowell, "Contact electrification of metals," *J. Phys. D, Appl. Phys.*, vol. 8, pp. 53-63, 1975.
- [63] P. G. Castle, I. I. Inculet, G. S. Sines, and L. B. Schein, "Contact charging between metals revisited," *IEEE Trans. Indust. Appl.*, vol. 40, pp. 1226-1230, 2004.
- [64] K. Tanoue, A. Ema, and H. Masuda, "Effect of material transfer and work hardening of metal surface on the current generated by impact of particles," *J. Chem. Eng. Japan.*, vol. 32, pp. 544-548, 1999.
- [65] L. Xie, G. Li, N. Bao, and J. Zhou, "Contact electrification by collision of homogenous particles," *J Applied Physics*, vol. 113, pp. 1-7, 2013.
- [66] A. I. Ette and E. U. Utah, "Studies of point-discharge characteristics in the atmosphere," *J. Atoms. Terr. Phys.*, vol. 35, pp. 1799-1809, 1973.
- [67] P. Cartwright, S. Singh, A. G. Bailey, and L. J. Rose, "Electrostatic charging characteristics of polyethylene powder during pneumatic conveying," *IEEE Transact. Ind. App.*, vol. IA-21, pp. 541-546, 1985.

- [68] S. R. Waitukaitis, V. Lee, J. M. Pierson, S. L. Forman, and H. M. Jaeger, "Size-dependent same-material tribocharging in insulating grains," *American Physical Society*, pp. 218001(1-5), 2014.
- [69] H. Zhao, G. S. Peter Castle, I. I. Inculet, and A. G. Bailey, "Bipolar charging of polydisperse polymer powders in fluidized beds," *IEEE Trans. Ind. Appl.*, vol. 39, pp. 612-618, 2003.
- [70] H. Zhao, G. S. Castlel, and I. I. Inculet, "The measurement of bipolar charge in polydisperse powders using a vertical array of Faraday pail sensors," *J. Electrostatics*, vol. 55, pp. 261-278, 2002.
- [71] J. Lowell and W. S. Truscott, "Triboelectrification of identical insulators: I. An experimental investigation," *J. Physc. D: Appl. Phys.*, vol. 19, pp. 1273-1280, 1986.
- [72] Z. Yan, S. K. Wilkinson, E. H. Stitt, and M. Marigo, "Investigating mixing and segregation using discrete element modelling (DEM) in the Freeman FT4 rheometer," *Int. J. Pharm.*, vol. 513, pp. 38-48, 2016.
- [73] P. M. Lacey, "Developments on the theory of particle mixing," *J Applied Chemistry*, vol. 4, pp. 257-268, 1954.
- [74] M. Jiang, Y. Zhao, G. Liu, and J. Zheng, "Enhancing mixing of particles by baffles in rotating drum mixer," *Particuology*, vol. 9, pp. 270-278, 2011.
- [75] B. Remy, J. G. Khinast, and B. J. Glasser, "Polydisperse granular flows in a bladed mixer: Experiments and simulation of cohesionless spheres," *Chemical Engineering Science*, vol. 66, pp. 1811-1824, 2011.
- [76] J. Mosby, S. R. de Silva, and G. G. Enstad, "Segregation of particulate materials-Mechanisms and testers," *KONA Powder*, vol. 14, pp. 31-42, 1996.
- [77] D. McGlinchey, "Assessment of segregation in industrial processes," *Powder Bulk Solids Technology*, vol. 22, pp. 54-56, 1998.
- [78] S. Zigan, R. B. Thorpe, U. Tuzun, G. G. Enstad, and F. Battistin, "Theoretical and experimental testing of a scaling rule for air current segregation of alumina powder in cylindrical silos," *Powder Tech.*, vol. 183, pp. 133-145, 2008.
- [79] B. Alchikh-Sulaiman, "Assessment of the mixing of polydisperse solid particles in the rotary drum and slant cone mixers using discrete element method," M. S. thesis, Dept. Chem. Eng., Ryerson University, Toronto, ON, 2014.

- [80] P. Tang and V. M. Puri, "Methods for minimizing segregation: a review," *Particulate Science and Technology*, vol. 22, pp. 321-337, 2004.
- [81] K. M. Forward, D. J. Lacks, and R. M. Sankaran, "Triboelectric charging of granular insulator mixtures due solely to particle—particle interactions," *Ind. Eng. Chem. Res.*, vol. 48, pp. 2309-2314, 2009.
- [82] P. Porion, N. Sommier, A. Faugere, and P. Evesque, "Dynamics of size segregation and mixing of granular materials in a 3D-blender by NMR imaging investigation," *Powder Tech.*, vol. 141, pp. 55-68, 2004.
- [83] B. Remy, J. G. Khinast, and B. J. Glasser, "Discrete element simulation of free flowing grains in a four-bladed mixer," *AlChE Journal*, vol. 55, pp. 2035-2048, 2009.
- [84] Y. Pu, M. Mazumder, and C. Cooney, "Effects of electrostatic charging on pharmaceutical powder blending homogeneity," *J. Pharm. Sci.*, vol. 98, pp. 2412-2421, 2009.
- [85] P. de Groot, "Principles of interference microscopy for the measurement of surface topography," *Adv. Opt. Photon.*, vol. 7, pp. 1-65, 2015.
- [86] Y. Lu, J. Park, L. Yu, and S.W. Kim, "3D Profiling of rough SiC surfaces by coherence scanning interferometry using femtosecond laser," *OSA Optical Society*, vol. 57, no. 10, pp. 2584-2589, 2018.
- [87] S. Adi, H. Adi, H. Chan, P. Young, D. Traini, R. Yang, and A. Yu, "Scanning white-light interferometry as a novel technique to quantify the surface roughness of micron-sized particles for inhalation," *Langmuir*, vol. 24, pp. 11307-11312, 2008.
- [88] J. C. Wyant, "White Light Interferometry," *University of Arizona*, Tucson, AZ, 2016.
- [89] S. Kuwamura and I. Yamaguchi, "Wavelength scanning profilometry for real-time surface shape measurement," *App. Opt.*, vol. 36, pp. 4473-4482, 1997.
- [90] L. C. Chen, D. H. Duong and C. S. Chen, "Optical 3D profilometry for measuring semiconductor wafer surfaces with extremely variant reflectivities," *Appl. Sci.*, vol. 9, pp. 1-18, 2019.

Chapter 3: A Novel Method for Generating a Single Layer of Powder and Calculating the Packing Factor with the Assistance of White-Light Interferometry, for Electron Beam Powder Bed Fusion (EB-PBF)

Basel Alchikh-Sulaiman, Paul R. Carriere, and Stephen Yue

Abstract

Despite the wide applications of powder metallurgy in the field of additive manufacturing (AM), knowledge on spreadability of powder particles in electron beam powder bed fusion (EB-PBF) is lacking. This study provides a literature review for flowability and spreading for AM processes. Different flowability tests are discussed in detail according to their mechanisms. Powder spreading mechanisms for different powder-bed AM are reviewed. A technique is proposed to study spreadability in which a single layer of powder is spread by a standard method, 'frozen' in the as spread condition by 'contact-sintering' and then characterized using white-light interferometry. As a result of this technique, a standard method to calculate the powder-bed density is defined, and correlations between powder-bed density, packing factor and flowability are established.

3.1 Introduction

Additive manufacturing (AM) delivers numerous design and manufacturing advantages including (i) the capability to construct complicated internal topographies and shapes, (ii) integration and optimization of functional features, (iii) a high degree of customization, (iv) reduction of post processing operations, and (v) high degree of efficiency in the usage of powders [1, 2].

AM technologies are classified according to source of energy, materials, and joining mechanism. Materials are in the form of wires or powders; source of applied energy is either electron beam or high-energy laser [2]. AM, which can be performed with polymer, ceramic and metals powders, begins with a CAD description of the component. Using this file, the machine lays down successive layers of powder in a layer-upon-layer fashion to generate the required 3D object [2]. The particles are spread onto a platform and melted by a high-energy beam (electron, plasma or laser), leading to the geometry buildup of a part layer-by-layer [1]. AM with powders are classified

into powder bed or direct deposition systems, where powder bed AM is considered more for industrial applications. AM with laser is available in several variants such as direct metal laser sintering (DMLS) and selective laser melting (SLM). On the other hand, industrial electron beam powder bed fusion is dominated by the Arcam system from Sweden [2, 3].

A suitable selection of powder is very important step to obtain required mechanical properties and microstructures for fabricated parts [4]. The following properties of powders will affect building components with electron beam powder bed fusion (EB-PBF) process. (i) Particle size distribution (PSD) affects the ability to generate layers with the appropriate characteristics [5]; (ii) Shape and its variation with particle size; spherical particles are desirable for EB-PBF; the existence of irregular shapes and satellites could affect flowability and the building process [2]; (iii) Surface roughness of particles can affect properties of final object including density, hardness, tensile strength, and surface texture; and (iv) tap and apparent densities are considered as essential characterizations to ensure a good layer deposition [6].

The deployment of powder in EB-PBF is based on three major steps [7]: (a) storage of powder inside hoppers under vacuum, (b) flow of powders from storage hopper to PBF build plane, a process requiring flowability, and (c) spreading the powder over the build 'table' with a rake, which is dependent on spreadability. The main outcome is to generate a well packed layer; the phenomenon of particle packing is an important research area for many physical and engineering fields [8, 9].

When powder falls from the hopper to the build plane under its own weight, this step is related to ability of powder to flow, or powder flowability. Also, the flowability measurement is related to the weight of the sample [10]. Flowability is the ability of powders to flow and is a consequence of the combination of three factors [11]: (i) Physical properties of powder particles, (ii) environmental conditions, such as temperature of powders and relative humidity, (iii) the equipment used for handling, storing, and processing these materials. Due to the influence of handling on measurement results and the complex nature of powders, flowability cannot be fully quantified with a single measurement technique [12]. Flowability is more related to the specific manufacturing process [13]. Once the powders fall from the hopper and accumulate on the build plane, a rake spreads the particles over the build 'table' and generates a powder layer with a known height; this process requires powders to be as spreadable [14].

The physics behind the formation of a powder bed for AM has not thoroughly investigated [9]. Flowability has been studied in depth but there are clearly differences between flowability and spreadability, although these have not been fully distinguished. The single layer (SL) of powder properties are based of four factors: powder layer density, layer thickness, absorption properties and thermal conductivity [6].

In the case of the first layer, the main differences between spreading and flow processes are concerned with build table (start-plate, or substrate) surface characteristics:(i) temperature, (ii) topography [15, 16]. For subsequent layers, it is the surface characteristics (roughness and temperature) of the previous layer that will be important. For all layers, the other main difference between spreading and flow is that the stresses experienced by the powder particles are caused by raking the particles at a constant velocity [9].

Additive manufacturing powder bed fusion (AM-PBF) technologies are usually operated with "fixed" process parameters to print a part. This means that inconsistent input powder characterizations will translate immediately into inconsistent quality of the finished part. Understanding relations between powder properties, spreading process and final-part properties are essential to define a robust powder specification [13].

The National Additive Manufacturing Innovation Institute (America Makes), and American National Standards Institute (ANSI) published on February 2017 the standardization roadmap for additive manufacturing and highlighted the issue of spreadability. "There is no known description of spreadability or standard for how to quantitatively assess powder spreadability": the suggested time-frame for spreadability research is 3-to-5 years [14].

The ability to measure and forecast powder flow behavior is important in powder metallurgy, ceramics, pharmaceuticals, food, and cosmetics [17, 18, 19]. Flow of a powder is affected by density, surface chemistry, shape and particle size distributions, and environmental conditions [20, 18].

A quantitative representation for flowability is proposed to consider all shear stresses of powder particles that are responsible for its flow behavior. A description for powder flowing through Hall flowmeter, a powder falls due to its weight [10]. Flow property of a powder is a function of various parameters, e.g. shape of particles, particle size distributions, bulk temperature, chemical

composition of particles and humidity. Unfortunately, an expression for flow behavior has not yet been determined as a function of the above parameters.

Accordingly, it is essential to measure the flow properties with appropriate devices [10, 17, 18]. The flowability of a granule depends on adhesive forces between particles. Powder particles cannot flow under the impact of their weight in the Hall flowmeter when forces between individual particles exceed gravitation. These forces are classified into: (i) interparticle friction, (ii) geometrical interlocking, (iii) adhesion due to liquid or solid bridging, (iv) electrostatic forces, and (v) van der Waals forces [10].

In case of dry particles, the forces due to van der Waals interactions play an essential role [10]. The classical approach to evaluate the powder flow is to measure the discharging time for 50 grams of a powder through the funnel of the Hall flowmeter. Recently, new approaches to evaluate the flow of a powder are dynamic angle of repose and the dynamic test for FT4 powder rheometer (Tewkesbury, United Kingdom) [17].

Where, the dynamic angle of repose apparatus consists of a rotating, transparent cylinder filled with a definite mass of powder and a camera in front of a backlight. The camera records images of the free surface of powder, and powder cross-sectional area inside the cylinder. At the end of rotations, powder images give the dynamic angle of repose [6] (Bodhmage [21] and Gu et al. [22]) or avalanche angle, which is the angle made by the inclined surface of a powder with the horizontal when rotated inside the cylinder; a large avalanche angle means poor flowability (**Fig. 3.1**) [23].

It is thought that the powder flow mechanism that generates an angle of repose inside a rotational powder analyzer is somewhat similar to the spreading process in the AM powder-bed process (SLM, and EB-PBF), in comparison to other flowability techniques [6].

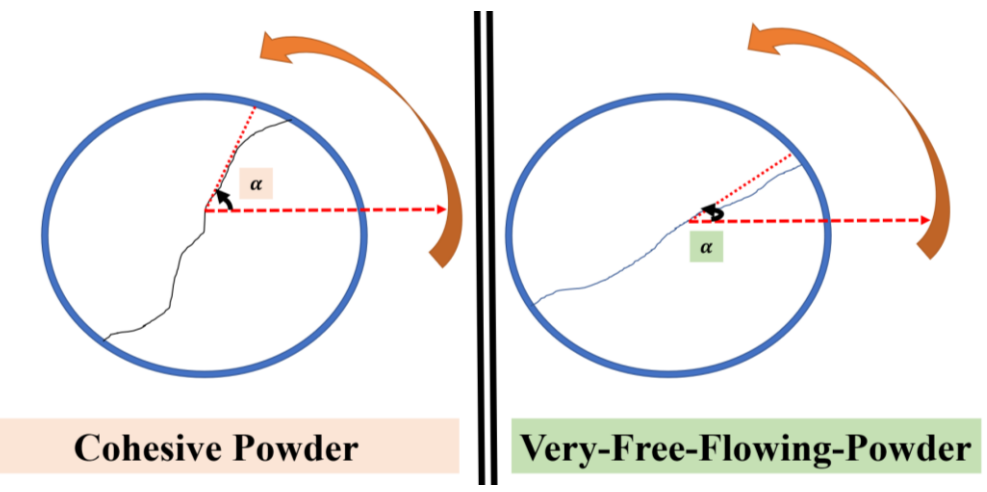


Figure 3.1: Schematic diagrams for two dynamic angles of repose for cohesive and very-flowing powders.

This technique was utilized for plastic powders for selective laser sintering (SLS) by Amado et al. [23], and two different tests were presented. The flowability test was performed at 0.003 mm/sec, where 'discrete' behavior was characterised by periodic avalanches. However, 'fluidization' was obtained for the range between 77 to 177 mm/sec, where a continuous flow of powder was achieved and characterized by a steady state angle of repose. For a powder within dynamic angle of repose, a nearly similar stress state condition to spreading process with rotating roller could be achieved in comparison to other flowability techniques [23].

3.1.1. Powder Spreading and Surface Characterization

For powder bed fusion (PBF), very thin powder layers are needed with good layer properties. In order to achieve thin layers, fine powders are utilized extensively to form beds. The spreading characteristics are then dependant on smoothness of the substrate and the powder volume fraction of the bed, i.e. packing factor, since rough surface, or high porosity could cause poor mechanical properties of the final product and softer bonding between layers [4, 5].

Spreadability is affected by van der Waals attractive forces, weight of powder particles and humidity [6, 13]. It was reported by Choi et al. [4] that powder layer density affects the density of 3D object, and the importance of layer compactness and smoothness for a new grade of polymer (PEEK) powder was shown by Berretta et al. [24].

Surface roughness of the powder bed, and surface quality of the part are strongly related. The solid volume fraction of a raw thermoplastic-elastomers powder, and porosity of sintered parts were also

found to be connected [25]. Thus, a dense and homogeneous powder layer is advisable, and it is therefore important to have a good flow characteristic [4].

Figure 3.2 shows a variety of spreading devices [6, 15, 26]. EB-PBF is one style from the additive manufacturing processes. This printing method is preferable for aerospace and implants medical applications because the vacuum minimizes impurities [2]. Besides industrial electron beam melting (Arcam system), there are research activities on self-built EB-PBF machines, which have not reached the performance of Arcam system [5, 26]. EBSM is a scientific name for electron beam selective melting machine developed by Guo et al. [26].

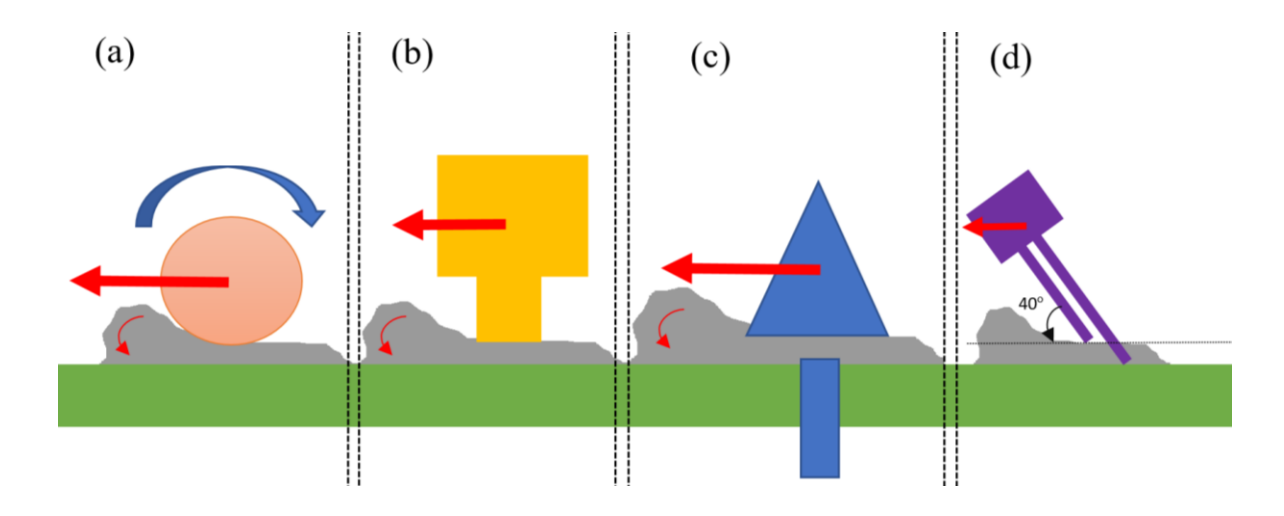


Figure 3.2: (a and b) schematic of AM spreading processes, (c) the cross section of one style of the industrial electron beam powder bed fusion (Arcam system) spreading system, and (d) dual-inclined combs for the EBSM Chinese system.

3.1.2 Packing Factor and Contact-Sintering Mechanism

In order to evaluate spreadability, the packing factor, or dimensionless packing density, is introduced as a tool to compare powder spreading. Analysis of a single layer of powder for electron beam melting has not been investigated, but a powder bed parameter was distinguished by Van den Eynde et al. [27], where the effectiveness of the spreading process was indicated by the packing factor (\emptyset) , which is the ratio of single layer density to solid density [27].

$$\emptyset = \frac{\rho_{powder-bed-layer}}{\rho_{solid}}$$
 (3.1)

Tap density (ρ_{tap}) delivers an indication for flowability of a powder from measurements of the change in bulk density induced by one directional tapping [28]. Van den Eynde et al. [27] have

defined the maximum packing factor (\emptyset_{max}) as the ratio of tap density to solid density for the same material. This ratio delivers the upper limit for the packing factor (\emptyset) and it is limited by particle geometry and size distribution [27].

$$\left(\emptyset_{max} = \frac{\rho_{tap}}{\rho_{solid}}\right) \ge \left(\emptyset = \frac{\rho_{powder-bed-layer}}{\rho_{solid}}\right)$$
 (3.2)

According to the above, the packing factor (\emptyset) is an index for the packing quality of a single powder layer in PBF; higher packing factor will lead to a denser sintered part [28]. The value of packing factor is a difficult parameter to measure because the as-spread powder bed is extremely unstable. In this paper, we present a novel approach to measuring packing factor whereby the asspread powder is stabilized by a contact-sintering (i.e. the sintering stage immediately prior to neck formation) heating schedule performed in a customized electron beam welding unit.

Relevant spreadability parameters, such as powder height distribution and their related packing factor, are then determined by optical profilometry [29].

3.2 Experimental Methods

3.2.1 White-Light Interferometry

Noncontact optical profilometry (ZygoTM NewView 8000, Zygo Corporation, Connecticut, USA) using scanning white-light interferometry offers a rapid, reliable and convenient way of performing surface roughness measurements, characterizations of the contact-sintering samples, and large area image stitching with superior 3D surface visualization.

All measurements are non-destructive and require no sample preparation. White-light interferometry involves scanning the object, through the Z-axis in non-contact mode, using white-light, and measuring the visibility of the interference fringes (degree of coherence) at each pixel in the image [29]. White-light interferometry was utilized to obtain different surface measurements, such as surface roughness (R_a) (µm) [30], root-mean-square roughness (R_a) (µm), and the root mean square gradient of the surface (S_{dq}) (µm/mm) [31]. The areal ISO hybrid (S_{dq}) parameter is a measurement of the slopes that cover a surface and is applied to differentiate between surfaces with similar roughness values. At the end of Chapter 4, **Appendix A4** provided the equations of these surface parameters.

Surfaces were characterized with a 2.75x Michelson lens under an operating condition correlating to a 40 nm bandpass F2 filter [31]; the scan length is extended to 400 μ m and bottom is defined as a scan origin; the related acquisition time for defined scan length is 53 sec/grid, and configuration stitch option with 2.75x lens is utilized extensively to scan the complete area. However, the reference to obtain the three topographical parameters (R_a , RMS, and S_{dq}) was selected to be a plane form remove.

3.2.2 Experiments

Single layer powder experiments were performed by a standardized 'spreading' technique and then 'contact-sintered', i.e. sintered up to the point immediately prior to neck formation, by electron beam, to 'freeze' the packed layer. This was then examined by white-light interferometry to determine the spreading characteristics, such as packing factor, which indicates 'spreadability'. In this way, a relationship between powder characteristics and spreadability can be generated.

3.2.3 Materials

Plasma-atomized Ti-6Al-4V (grade 23) powder particles from a commercial producer were used. According to the powder certificates, the PSD, flow rate, apparent and tap densities are presented in **Table 3.1**.

Grade-5 Ti-6Al-4V, and Inconel 718 plates with 1.53 mm thickness were laser cut into approximately 50mm x 50mm sections, by Baoji Magotan Nonferrous Metals Co. (Shaanxi, China), and were used as substrates on which the powders were spread. The solid density for Ti-6Al-4V is 4.42 g.cm⁻³ [32].

Table 3.1: Physical properties for powders.

Powder	PSD	Flowrate	Apparent density	Tap density
	(μm)	$\left(\frac{sec}{50\ gram}\right)$	$\left(\frac{gram}{cm^3}\right)$	$\left(\frac{gram}{cm^3}\right)$
Ti-6Al-4V	45 - 106	23	2.57	
(grade 23)				2.80
(grade 25)	15 - 45	30	2.50	

3.2.4 Procedure to Prepare a Single Layer of Powder

To facilitate the production of a single layer of powder that has a uniform thickness, the substrate must be as flat and as smooth possible, **Fig. 3.3**.

To spread the powder over this substrate, a stainless steel (316L) metal puck was fabricated (**Fig. 3.4**). A high degree of flatness (\pm 9 μ m) and smoothness was obtained for this puck with a manually operated grinding machine.

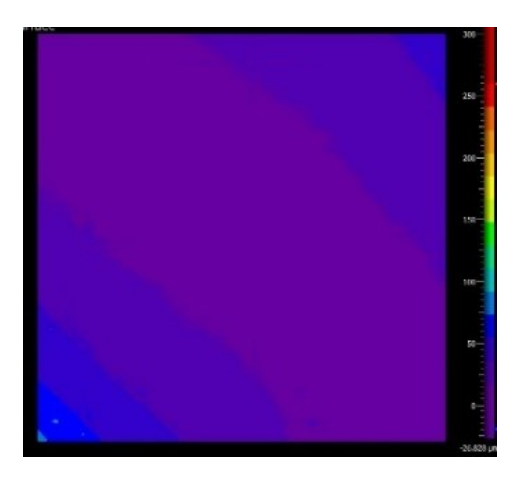


Figure 3.3: A measured Inconel 718 substrate with White-light interferometry. The color contour for this image was 20 μ m per color division, and the surface roughness Ra = 3.44 μ m.

To spread the powder over the prepared substrate, the flat puck was manually rotated for two complete rotations, with an angular velocity of about 0.5 rotation/min.

Powder was slowly poured into a funnel (Fig. 3.5-a) over the substrate for 30 seconds. The puck was then placed gently on top of the powder for 30 seconds before the rotation (Fig. 3.5-c).

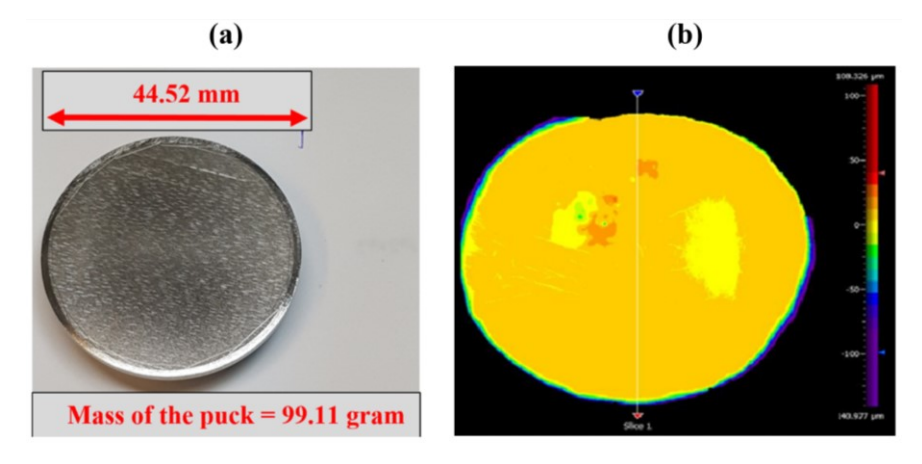


Figure 3.4: (a) Image for the utilized stainless-steel 316L puck, and (b) the measured surface with White-light interferometry (right). The color contour for this image was 10 μ m per color division, and the flatness of the puck was around \pm 9 μ m.

Figure 3.6 represents a diagram for the procedure to prepare a single layer (SL) of powder. The spreading procedure was applied inside the chamber to eliminate specimen transfer problems.

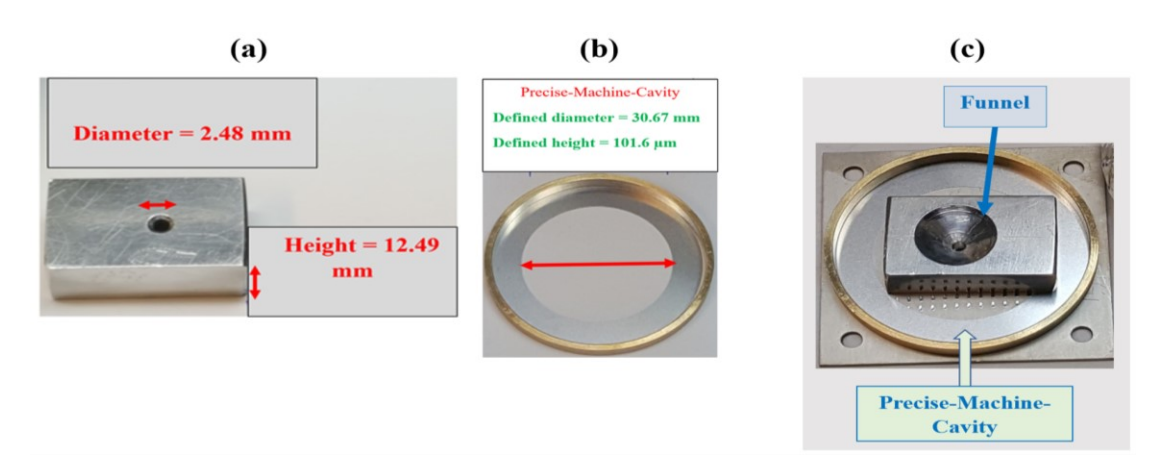


Figure 3.5: (a) the lower side of a funnel used to pour powder particles with a 2.48 mm outlet diameter, (b) dimensions of the precise-machine cavity that was fabricated with a definite height, and (c) an image for set-up.

To simulate spreading in a real AM process when the build 'table' is lowered by a specific height to allow the spreading of a layer, a specific cavity, with height of 76.2 µm or 101.6 µm, was introduced as shown in **Fig. 3.5-b** and **Fig. 3.5-c**. In other words, this specific cavity was utilized to control the height between spreading puck and substrate.

By applying powder according to previous set-up and procedure, powder was spread in a circular shape. Note that the thickness of this 'single' layer is approximately two or three particles thick [33].

3.2.5 Contact-sintering

Contact-sintering, as mentioned previously, is a powder process that is utilized to freeze the powder particles in the as-spread condition, with minimal changes in the morphology of powder particles and packing characteristics and is based on two sequential steps. The first step is to heat the powder using the electron beam inside a vacuum chamber from 25°C to several hundred degrees Celsius in a short period of time without a direct contact between beam and powder to avoid powder smoking [34]. The second step is to maintain this high temperature for four to six minutes only.

Figure 3.7-a showed a sample of powder inside chamber during the contact-sintering process. Thus, particle-particle bonding occurs at the as-spread contact points without any neck formation

between powder particles as seen in (**Fig. 3.7-b**), which was obtained by white-light interferometry (ZygoTM, using a 50x Mirau lens).

To proof a concept, a SEM image was obtained for the sample, **Fig. 3.7-c** (SEM SU3500, Hitachi, Japan); the morphology of powder particles was not changed by this process.

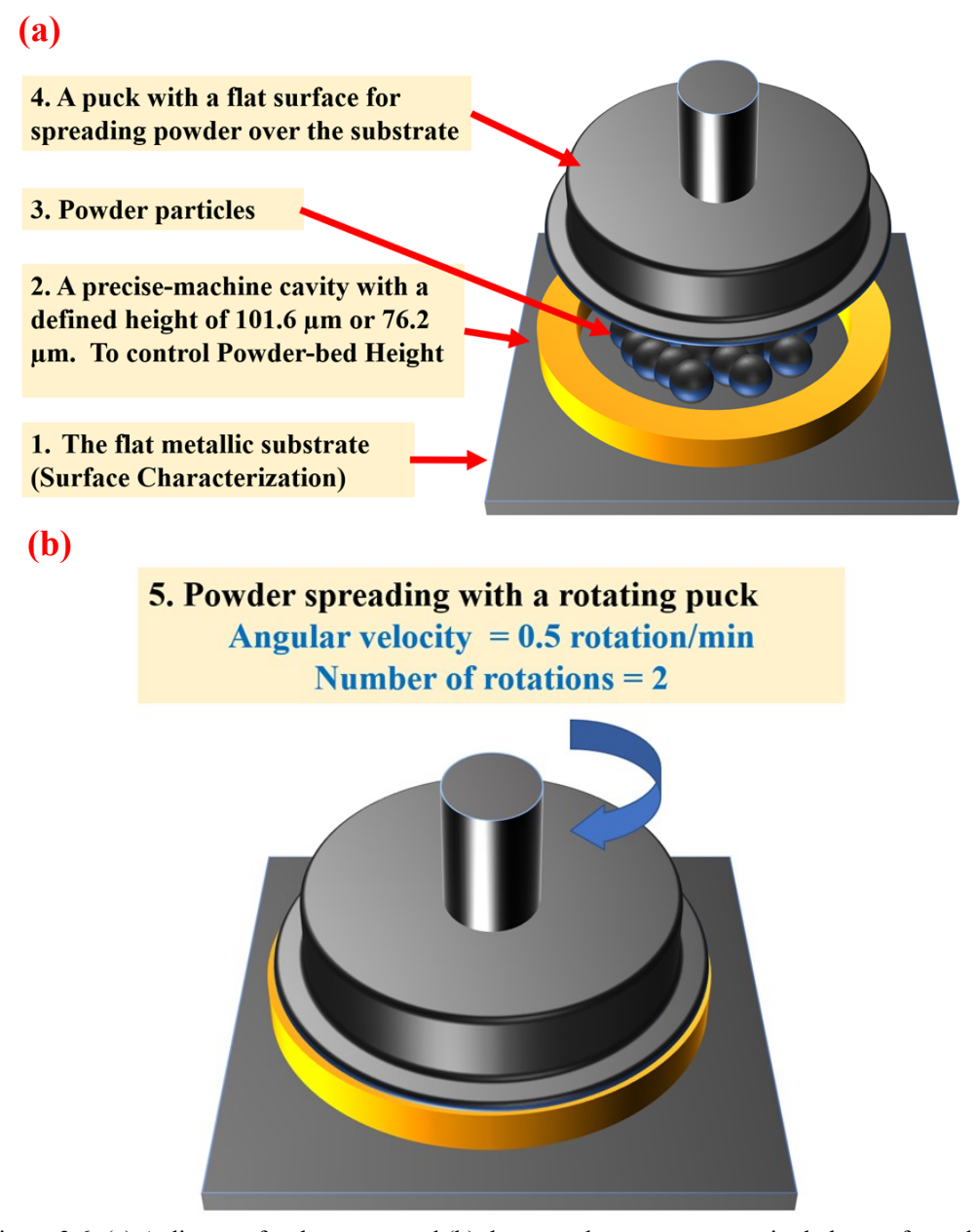


Figure 3.6: (a) A diagram for the set-up and (b) the procedure to prepare a single layer of powder.

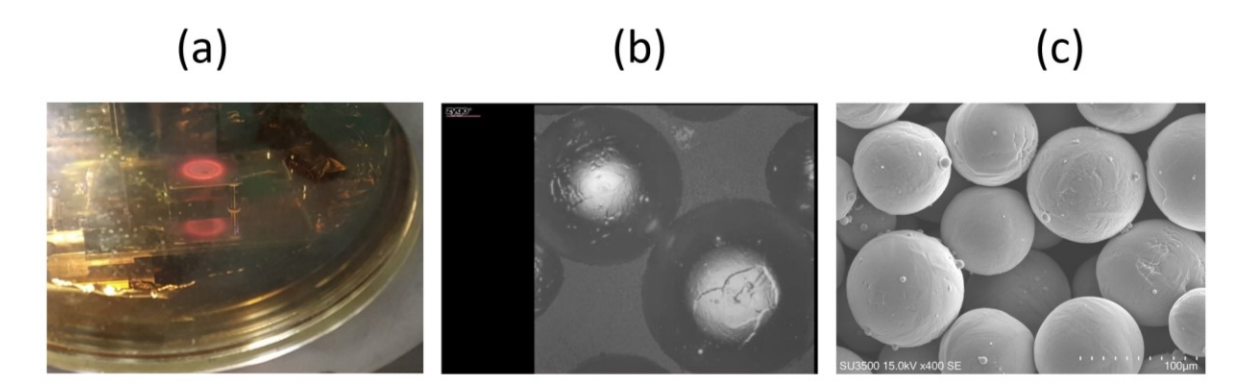


Figure 3.7: (a) image via the window of chamber during the contact-sintering, (b) image of contact-sintered Cp-Ti over the substrate with Zygo NewView 8000 and 50x Mirau lens, and (c) SEM image of contact-sintered Cp-Ti over the substrate

3.2.6 Methodology for Calculating the Density of a Single Layer (SL) of Powder

The weight of powder and substrate is recorded initially. After contact-sintering, the total weight of sample (substrate + contact-sintered powder) is measured. Thus, the utilized mass of powder (m_{SL}) was determined. The shape of the SL was assumed to be a thin disc.

Surface topography of the SL was measured by White-light interferometry. **Figure 3.9** is an example showing the height profiles for four slices (cross-sections) lines with respect to average diameter for sample 1. The maximum powder height (h_{max-1}) was equal to 374 μ m.

From Fig. 3.9-a, area $(area_{SL})$ of best fit circle to SL circumference was determined by the measured surface. Thus, SL density (ρ_{SL}) was calculated according to **Equation (3.3)**.

$$\rho_{SL} = \frac{m_{SL}}{h_{max} \times area_{SL}} \tag{3.3}$$

3.3 Results and Discussion

3.3.1 Calibrating Zygo Measurements

A gauge block is a metallic block that has been precision ground and lapped to a specific thickness. It is utilized to produce precision lengths and has two opposing faces ground precisely flat and parallel, as shown in (Fig. 3.8-a).

It was scanned with the Zygo to validate the profile measurements and surface roughness values. At the beginning of the scan procedure, the Zygo was focused and tilted at the center point C; and measured from terminal point B towards point A.

According to (**Fig. 3.8-b** and **Fig. 3.8-c**), scanning result without a form remove showed that the point B was lower than A with a difference equal to 0.33 µm. The form remove selects a specific surface to remove. Thus, results are deviated from the surface that has removed [35].

If the overall shape is not removed, it might dominate the results making it difficult to determine the actual quality of the surface. When overall surface shape is subtracted, MetroPro (ZygoTM software) analyzes the difference between a mathematical surface and the actual surface and will highlight the surface irregularities [35].

Plane form remove causes the tilted data to be presented flat and allows the vertical scale to be expanded. As a result of that, revealing much greater detail about the surface. On the other hand, the scanning result with the form remove showed that points B, and A are almost on the same height but concave at the center of the surface. The variation between (**Fig. 3.8-a**, **Fig. 3.8-b**, and **Fig. 3.8-c**) showed the effect of form remove. If not mentioned, a plane-form remove is applied for the rest of measurements.

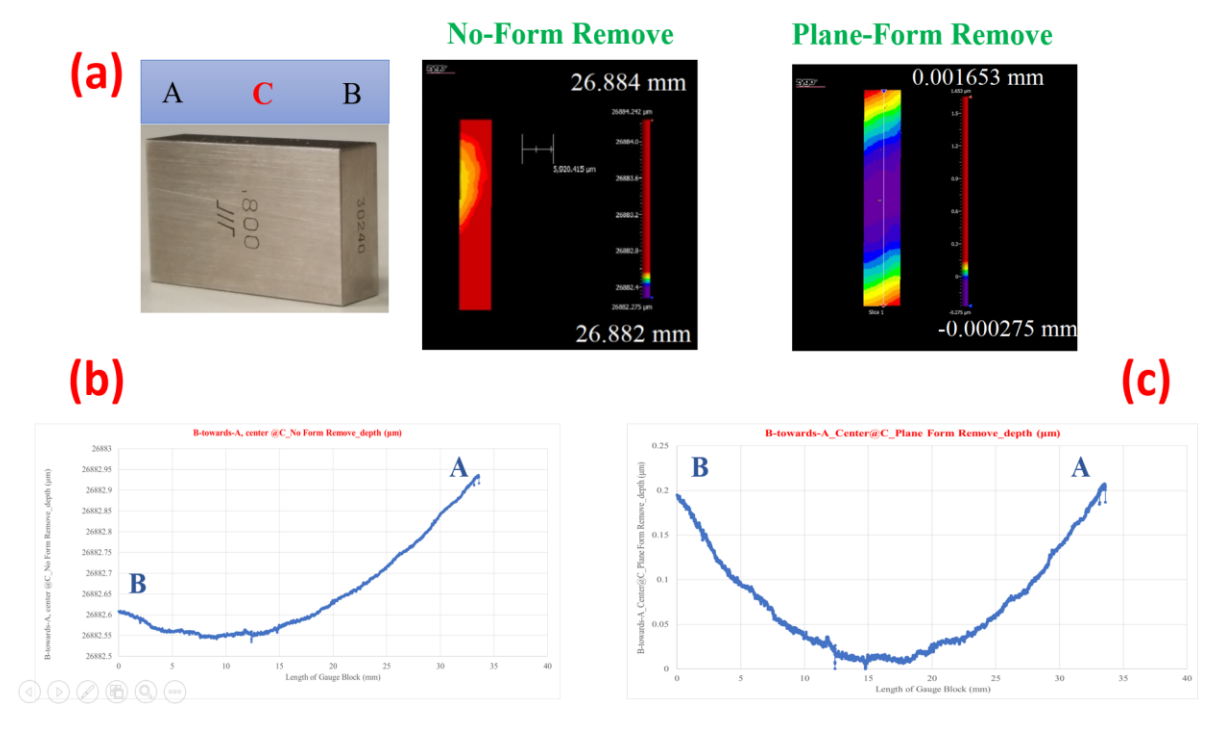


Figure 3.8: (a) Gauge block used for this measurement with three scanning positions at two terminals and center A, C, and B; (middle-image) the scanning results for the gauge block surface with a direction from B-to-A with No-Form and Plane Form removes (right-image); (b) variation of surface' depth (μm) without a form remove with respect to the length of gauge block (mm); and (c) variation of surface's depth (μm) with a plane-form remove with respect to the length of gauge block (mm).

3.3.2 A Relation Between the Packing Factor of SL and Surface Roughness of Substrate

Samples 1, 2, 3, 4, 5 and 6 were prepared according to the method explained earlier in the Experimental Methods and measured with white-light interferometry after contact-sintering at 700 °C, **Table 3.2**. The goal of this set of experiments was to compare powder heights and packing factors for powder samples.

Table 3.2: Samples with their related masses and substra	Table 3.2:	2: Samples v	with their	related	masses	and	substrat
--	------------	--------------	------------	---------	--------	-----	----------

Ti-6Al-4V (Grade 23)	Sample	Substrate	Mass (gram)
	1		0.122
$PSD = 45 - 106 \mu m$	2	Inconel 718	0.097
	3		0.087
	4	Ti-6Al-4V	0.082
$PSD = 15 - 45 \mu m$	5	(Grade 5)	0.083
15D 15 45 μm	3	(Grade 3)	0.063
	6		0.076

From **Table 3.3**, the following measurements were obtained to compare spreadability of samples 1, 2, 3, 4, 5 and 6. Based on **condition (3.2)**, the maximum packing factor (\emptyset_{max}) for Ti-6Al-4V was calculated.

$$\emptyset \le 63.3\%$$
 (3.4)

Thus, the values of packing factor agreed with **condition (3.4)**.

Table 3.3: Packing factor values for samples 1, 2, 3, 4, 5 and 6.

Ti-6Al-4V (Grade 23)	Sample	Height of specific cavity (μm)	Area (mm²)	Maximum height (μm)	$ \frac{\text{SL density}}{\left(\frac{gram}{cm^3}\right)} $	Packing factor (Ø × 100%)
	1	101.6	176	374	1.85	41.9
$PSD = 45 - 106 \mu m$	2		120	316	2.56	57.9
	3	76.2	132	276	2.38	53.8
	4		274	172	1.74	39.4
	5	101.6	409	94	2.15	48.6
$PSD = 15 - 45 \mu m$	6		319	105	2.26	51.2

The maximum powder heights for samples 1, 2 and 3 were 374 μ m, 316 μ m and 276 μ m, respectively. These heights were higher than the heights of specific cavities (101.6 μ m and 76.2 μ m). Also, the maximum heights for samples 4, 5 and 6 were higher than the 101.6 μ m specific cavity.

This could be explained that cohesive forces between particles are stronger than shear forces during spreading with a puck.

Figure 3.9 shows SL surfaces for samples 1, 2 and 3, where the measured surfaces were presented with same color contour scale ($20\mu m$ /color div).

Substrates were not prepared initially to have flat surfaces, as it could be seen in **Fig. 3.9**. A non-flat surface might affect the powder spreading. From **Table 3.3**, the results of packing factor were scattered a bet due to the level of flatness for substrates.

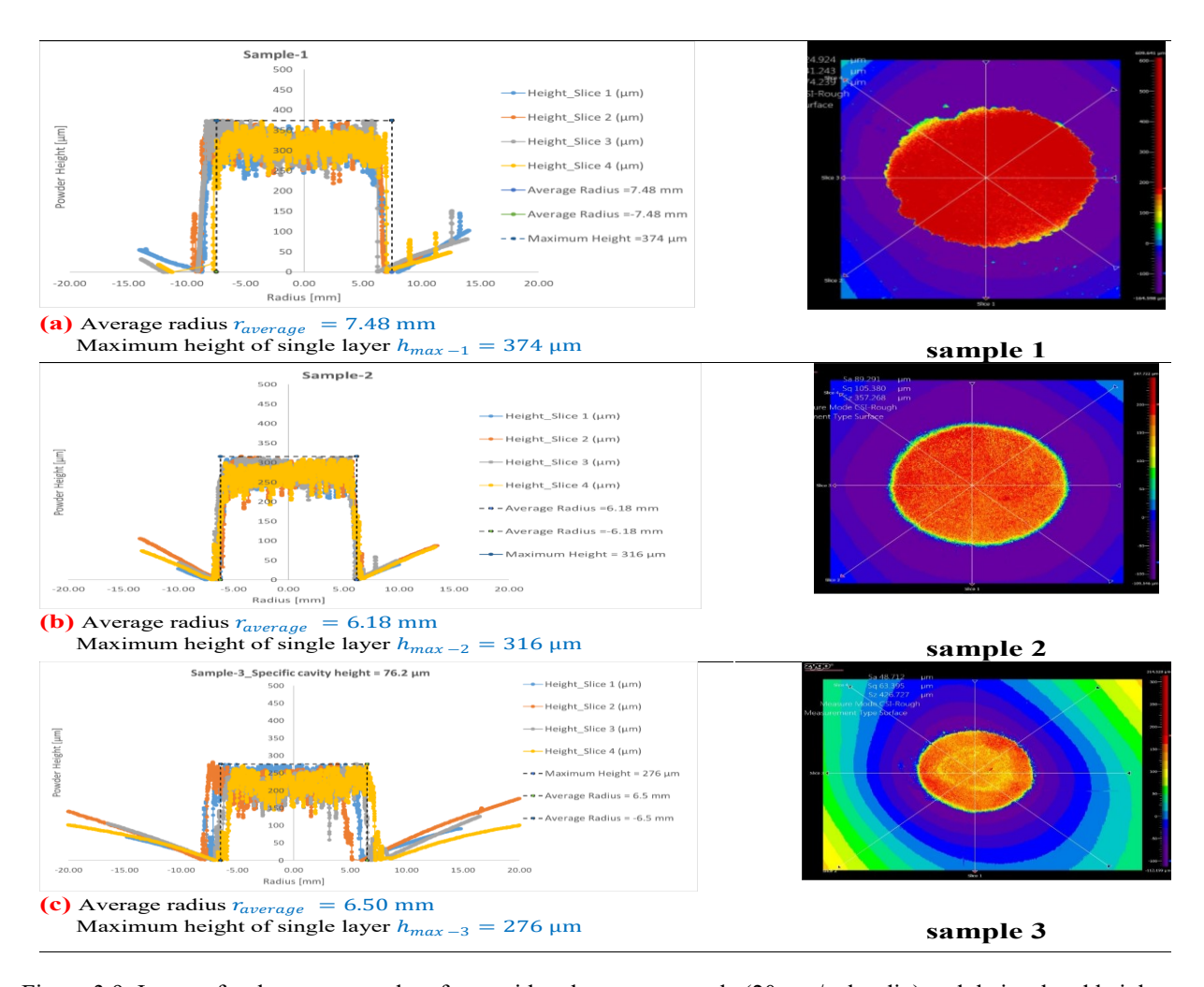


Figure 3.9: Images for three measured surfaces with color contour scale ($20\mu m$ /color div) and their related height profiles.

From **Table 3.4**, the surface texture of SL samples with same PSD had similar values of $(Sdq_{substrate})$. However, the influence of PSD was captured clearly for the values of (RMS_{SL}) where samples 4, 5 and 6 had smoother surfaces in compare with the samples of the larger PSD.

Table 3.4: Values of surface parameters for substrates and single layer for the 6 samples

		Sub	ostrate	Single layer of powder (SL)				
Sample	R_a (μm)	RMS (µm)	$\left(S_{dq}\right)_{substrate} \left(\frac{\mu m}{mm}\right)$	RMS_{SL} (μm)	$\left(S_{dq}\right)_{SL}\left(\frac{\mu m}{mm}\right)$			
1	1.20	4.33	143	34.3	1027			
2	0.82	1.54	97	25.7	1150			
3	0.42	0.53	42	32.7	1178			
4	0.13	0.31	26	23	902			
5	0.20	0.29	20	14	890			
6	0.26	0.32	109	18.7	908			

Thus, spreading mechanism has generated reliable single layers and the fluctuations of packing factors are caused by the topography of substrates.

3.4 Conclusions

This study provided a literature review for different powder flow tests and spreading mechanisms. The packing factor and its upper limit (maximum value) were discussed according to the density of a single layer of powder. This research established a methodology and defined the required tools to study the packing factor as an indication of spreadability.

Contact-sintering mechanism with the assistance of white-light-interferometry created a potential to understand the relation between powder flow, packing factor and surface topography. Finally, the texture for a single layer was evaluated with different topographical parameters.

References

- [1] Y. Sun, S. Gulizia, C. Oh, C. Doblin, Y. Yang, and M. Qian, "Manipulation and characterization of a novel titanium powder precursor for additive manufacturing applications," *The Minerals, Metals & Materials Society*, vol. 67, pp. 564-572, 2015.
- [2] G. Baudana, S. Biamino, D. Ugues, M. Lombardi, P. Fino, M. Pavese, and C. Badini, "Titanium aluminides for aerospace and automotive applications processed by electron beam melting: contribution of Politecnico di Torino," *Metal Powder Report*, vol. 71, pp. 193-199, 2016.
- [3] M. Weglowski, S. Blacha, and A. Phillips, "Electron beam welding-techniques and trends-review," *Vacuum*, vol. 130, pp. 72-92, 2016.
- [4] J. P. Choi, G. H. Shin, H. S. Lee, D. Y. Yang, S. Yang, C. W. Lee, M. Brochu, and J. H. Yu, "Evaluation of powder layer density for the selective laser melting (SLM) process," *Mater. Trans.*, vol. 58, pp. 294-297, 2017.
- [5] C. Körner, "Additive manufacturing of metallic components by selective electron beam melting, a review," *International Materials Reviews*, vol. 61, pp. 361-377, 2016.
- [6] A. B. Spierings, M. Voegtlin, T. Bauer, and K. Wegener, "Powder flowability characterization methodology for powder-bed-based metal additive manufacturing," *Prog. Addit. Manuf.*, vol. 1, pp. 9-20, 2016.
- [7] A. Klassen, T. Scharowsky, and C. Korner, "Evaporation model for beam based additive manufacturing using free surface lattice Boltzmann methods," *J. Phys. D: Appl. Phys.*, vol. 47, pp. 1-12, 2014.
- [8] H. P. Zhu, Z. Y. Zhou, R. Y. Yang, and A. B. Yu, "Discrete particle simulation of particulate systems: a review of major applications and findings," *Chem. Eng. Sci.*, vol. 63, pp. 5728-5770, 2008.
- [9] Z. Xiang, M. Yin, Z. Deng, X. Mei, and G. Yin, "Simulation of forming process of powder bed for additive manufacturing," *J. Manuf. Sci. Eng.*, vol. 138, pp. 081002, 2016.
- [10] D. Schulze, *Powders and Bulk Solids: Behavior, Characterization, Storage and Flow.* Berlin, Germany: Springer-Verlag Berlin Heidelberg, 2008.
- [11] V. Ganesan, K. A. Rosentrater, and K. Muthukumarappan, "Flowability and handling characteristics of bulk solids and powders-a review with implications for DDGS," *Biosystems Engineering*, vol. 101, pp. 425-435, 2008.

- [12] A. Santomaso, P. Lazzaro, and P. Canu, "Powder flowability and density ratios: the impact of granules packing," *Chemical Engineering Science*, vol. 58, pp. 2857-2874, 2003.
- [13] J. Clayton, J. Dawes, and C. Langley, "Optimizing metal powders for additive manufacturing: exploring the impact of particle morphology and powder flowability," *additivemanufacturing.media*, May 26, 2017. [Online]. Available: http://www.additivemanufacturing.media/blog/post/optimizing-metal-powders-for-additive-manufacturing-exploring-the-impact-of-particle-morphology-and-powder-flowability. [Accessed Dec. 20, 2018].
- [14] G. Berkebile, K. Creehan, S. Deutsch, R. Gorham, E. Morris, H. Cheung, S. Doucet, J. F. Forte, I. Kiselyer, J. McCabe, L. Neiman, L. Rajchel, F. Schrotter, M. Voizard, and D. Wiser, "Standardization roadmap for additive manufacturing," National Additive Manufacturing Innovation Institute (America Makes), and American National Standards Institute (ANSI), 2017.
- [15] L. Loewgren and M. Wildheim, "Method for improved powder layer quality in additive manufacturing", U.S. Patent 2016/0129501 A1, May 12, 2016.
- [16] E. Parteli and T. Pöschel, "Particle-based simulation of powder application in additive manufacturing," *Powder Tech.*, vol. 288, pp. 96-102, 2016.
- [17] R. Freeman, "Measuring the flow properties of consolidated, conditioned and aerated powders-a comparative study using a powder rheometer and a rotational shear cell," *Powder Tech.*, vol. 174, no. 1, pp. 25-33, 2007.
- [18] M. K. Stanford and C. DellaCorte, "Effects of humidity on the flow characteristics of a composite plasma spray powder," *J. Therm. Spray. Tech.*, vol. 15, pp. 33-36, 2006.
- [19] B. Alchikh-Sulaiman, F. Ein-Mozaffari, and A. Lohi, "Evaluation of poly-disperse solid particles mixing in a slant cone mixer using discrete element method," *Chemical Engineering Research and Design*, vol. 96, pp. 196-213, 2015.
- [20] A. Adler, "Flow properties of metal powders," *International Journal of Powder Metallurgy*, vol. 5, pp. 7-20, 1969.
- [21] A. Bodhmage, "Correlation between physical properties and flowability indicators for fine powders," Ph.D. dissertation, Dept. Chem. Eng., University of Saskatchewan, Saskatoon, SK, 2006.

- [22] H. Gu, H. Gong, J. J. Dilip, D. Pal, A. Hicks, H. Doak, and B. Stucker, "Effects of powder variation on the microstructure and tensile strength of Ti-6Al-4V parts fabricated by selective laser melting,": *Proceedings of the Annual International Solid Freeform Fabrication Symposium*, *Austin, TX, USA, August 4-6, 2014*, D.L. Bourell, R.H. Crawford, C.C. Seepersad, J.J. Beaman, S. Fish, H. Marcus, Eds. Austin: The University of Texas at Austin, 2014. pp. 470-483.
- [23] F. Amado, M. Schmid, G. Levy, and K. Wegener, "Advances in SLS powder characterization,": *Proceedings of the Annual International Solid Freeform Fabrication Symposium, Austin, TX, USA, August 8-10, 2011,* D.L. Bourell, R.H. Crawford, C.C. Seepersad, J.J. Beaman, H. Marcus, Ed. Austin: The University of Texas at Austin, 2011. pp. 3-5.
- [24] S. Berretta, O. Ghita, and K. Evans, "Morphology of polymeric powders in laser sintering (LS): from polyamide to new peek powders," *European Polymer Journal*, vol. 59, pp. 218-229, 2014.
- [25] S. Ziegelmeier, P. Christou, F. Wollecke, C. Tuck, R. Goodridge, R. Hague, E. Krampe, and E. Wintermantel, "An experimental study into the effects of bulk and flow behavior of laser sintering polymer powders on resulting part properties," *Journal of Materials Processing Technology*, vol. 215, pp. 239-250, 2015.
- [26] C. Guo, F. Lin, W. J. Ge, and J. Zhang, "Development of novel EBSM system for high-tech material additive manufacturing research,": *Proceedings of the Annual International Solid Freeform Fabrication Symposium*, *Austin, TX, USA, August 4-6, 2014*, D.L. Bourell, R.H. Crawford, C.C. Seepersad, J.J. Beaman, S. Fish, H. Marcus, Eds. Austin: The University of Texas at Austin, 2014. pp. 298-308.
- [27] M. Van den Eynde, L. Verbelen, and P. Van Puyvelde, "Assessing polymer powder flow for the application of laser sintering," *Powder Tech.*, vol. 286, pp. 151-155, 2015.
- [28] J. Clayton and R. Deffley, "Optimizing metal powders for additive manufacturing," *Metal Powder Report*, vol. 69, pp. 14-17, 2014.
- [29] S. Adi, H. Adi, H. Chan, P. Young, D. Traini, R. Yang, and A. Yu, "Scanning white-light interferometry as a novel technique to quantify the surface roughness of micron-sized particles for inhalation," *Langmuir*, vol. 24, pp. 11307-11312, 2008.
- [30] Y. Lu, J. Park, L. Yu, and S.W. Kim, "3D Profiling of rough SiC surfaces by coherence scanning interferometry using femtosecond laser," *OSA Optical Society*, vol. 57, no. 10, pp. 2584-2589, 2018.
- [31] C. Gomez, R. Su, A. Thompson, J. DiSciacca, S. Lawes, and R. Leach, "Optimization of surface measurement for metal additive manufacturing using coherence scanning interferometry," *Optical Engineering*, vol. 56, no. 11, pp. 111714 (1-8), 2017.

- [32] K. C. Mills, Recommended Values of Thermophysical Properties for Selected Commercial Alloys. Cambridge, UK: Woodhead Publishing, 2002.
- [33] W. Nan, M. Pasha, T. Bonakdar, A. Lopez, U. Zafar, S. Nadimi, and M. Ghadiri, "Jamming during particle spreading in additive manufacturing," *Powder Tech.*, vol. 338, pp. 253-262, 2018.
- [34] P. R. Carriere, "Energy and charge transfer during electron beam melting," Ph.D. dissertation, Dept. Mater. Eng., McGill Univ., Montreal, QC, 2018.
- [35] K. Turner, "Standard Operating Procedures of Tools in Quattrone Nanofabrication Facility," March 2019. [Online]. Available: https://www.seas.upenn.edu/~nanosop/Zygo Remove.htm. [Accessed Feb. 01, 2018].

Chapter 4: For Powder Bed Additive Manufacturing Process: Correlations between Single Layer Density and Powder Properties with the Assistance of Coherence Scanning Interferometry

Basel Alchikh-Sulaiman, Paul R. Carriere, and Stephen Yue

In chapter 3, a technique was introduced to examine spreadability in which a single layer of powder was spread by a standard method, 'frozen' in the as spread condition by 'contact-sintering' and then characterized using the white-light interferometry. As a result of that, a method to calculate the packing factor was established. In this chapter, with the assistance of the coherence scanning interferometry CSI (white-light interferometry), different surface measurements are conducted and the value of surface roughness (R_a) obtained with CSI will be validated with a stylus profiler. Also, the powder rheometer is used to examine the relations between powder properties and flow.

Abstract

There is a lack of sufficient knowledge regarding the effect of powder properties (particle size distribution PSD, surface morphology, etc.) on the density of single layer for AM powder bed fusion process. Contact-sintering (CS) is a simple, low-cost technique that can be used to evaluate the packing characteristics of a single layer with different particle size distributions (PSDs) and thicknesses. The CS depends heavily on the coherence scanning interferometry to obtain different surface measurements (powder height distribution, R_a and RMS). For this reason, the value of surface roughness (R_a) obtained with coherence scanning interferometry is validated with a stylus profiler. As a result of the CS technique, correlations between the density of single layer and powder properties can be established. The powder rheometer is applied to investigate relations between powder properties and flow. Finally, three surface topography parameters (R_a , Skewness and S_{dq}) are applied to compare between substrates.

4.1 Introduction

Additive manufacturing (AM) begins with a three-dimensional (3D) computer-aided design of the part. Using this file, in powder bed fusion (PBF), the machine lays down successive layers of powder to produce the required 3D part [1]. Additive manufacturing processes are sorted according to the source of materials, joining mechanism, and energy. The source of applied energy is either a high-energy laser (e.g. selective laser melting SLM) or an electron beam; materials are ceramics, polymers or metals in the form of wire or powder [1]. The electron beam powder bed fusion (EB-PBF) technology generally refers to the Arcam AB systems (GE additive company, Mölndal, Sweden) [1, 2].

A group of metals and alloys has been examined by EB-PBF for different applications (i) Ti-6Al-4V alloy for aerospace industry, and (ii) commercially pure titanium CP-Ti for medical applications. For EB-PBF and SLM, the recommended sizes are between 45 - 106 μm and 15 - 45 μm, respectively [3, 4].

The distribution of powder during EB-PBF is based on the following steps [5]: (i) storage of powder inside hoppers under vacuum; the build plane moves downwards a definite height (typically 50 to 100 microns) to allow for a layer of powder to be added to the build plane; (ii) flow of powder particles under its own weight from the storage hopper to the build plane;

this step is related to the powder flowability, which depends on the weight of the powder required for a single layer (SL) [6]. Flowability has been discussed widely and it is debatable considered a process specific [4]; (iii) spreading; once the powder particles fall from the hopper and accumulate, a rake spreads the powder to fill the space uniformly; this requires the powders to be spreadable [7]. The main objective is to generate layers with dense, homogenous packing characteristics, as this accelerates the overall building rate (cm³/hour) and generates a reproducible process. However, the physics behind the formation of this thin layer has not been thoroughly studied.

Based on the previous studies [6, 8, 9], the spreading and flow of powder are controlled by the following interparticle forces: (i) friction (geometrical interlocking and surface morphology), (ii) coulombic forces (van der Waals forces, electrostatic and tribocharging), (iii) adhesive forces: solid bridging, and liquid bridging (surface tension).

It was reported by Choi et al. [3] that powder layer density affects the density of the 3D object. The importance of layer compactness and smoothness for a new grade of polymer powder was shown by Berretta et al. [10]. Surface roughness of the powder bed, and surface quality of the part are strongly related. The solid volume fraction (a method to describe the packing factor) of the feedstock thermoplastic-elastomers powder, and porosity of sintered parts were also found to be connected [11]. Thus, a dense and homogeneous powder layer is advisable.

Spreading of powder and flow used to be considered as similar processes. However, there are differences between flow and spreading, and these differences have not been fully examined. For the first layer, the main differences between spreadability and flowability processes are concerned with build plane (substrate) surface characteristics: (i) topography, and (ii) temperature [12, 13]. However, the surface characteristics (roughness and temperature) of the previous layer will affect spreadability of the next layer. Another difference between powder spreading and flow is the stress situation experienced by the powder particles that is generated by raking the particles at a definite velocity [14]. For instance, the diameter of Hall flow orifice is 2540 μ m, and the average particle diameters for EB-PBF and SLM are 80 μ m and 30 μ m, respectively. The Hall flow orifice is equivalent to 32 particles in diameter for EB-PBF, and 85 particles for SLM. Whereas, the single layer during PBF is generally 2 to 3 particles thick. As a result of that, a large fraction of the contact points is between a solid surface (rake, substrate) and powder.

4.1.1 Powder Characterization

Prior to the development of powder production method generally known as atomization, the chemical properties of powder and morphology were not fully controlled. Thus, most metallic powders are fabricated by atomization, where this production method is suitable for different alloys, easy to control, and flexible in the melt purification, feedstock and chemical properties [15].

For any AM process, powder properties such as PSD, flowability, apparent density, and tapped density affect directly the ability to generate layers [16]. Several research groups reported evidences that the PSD of powder played an important role in determining final part properties for AM processes [17, 18, 19]. Studies have been conducted on the PSD effect on density, mechanical properties, and surface roughness for SLM fabricated parts [20]. Apparent density and flowability control the layer depositions, with a high packing density for individual layers generates a dense part [1].

A suitable selection of powder is important to obtain the required mechanical properties and microstructures. To describe a powder, the following characteristics need to be considered: (i) particle size and its distribution, (ii) shape and its variation with particle size, (iii) surface morphology/roughness and surface area, (iv) packing and flow, (v) particle microstructure (including voids, etc.), and (vi) interparticle forces (coulombic and adhesive) [3, 6].

Particle size metrics are often based on equivalence to spherical particles leading to parameters such as, maximum dimension, surface area, projected area, volume and minimum cross-sectional area. The equivalent spherical diameter can be determined from the projected area, surface area, or volume. If a particle has the projected area (A) [15], surface area (K), and volume (V); then the equivalent spherical diameter (D) is calculated by **Equations 4.1**, **4.2** and **4.3** in **Table 4.1**.

Table 4.1: Equations (4.1), (4.2) and (4.3) for the spherical diameter calculated according to the projected area, surface area and volume for a powder particle; and equation (4.4) is the sphericity factor (S)

4.1	4.1 4.2		4.4
$D_A = \sqrt{\frac{4A}{\pi}}$	$D_K = \sqrt{\frac{K}{\pi}}$	$D_V = \sqrt[3]{\frac{6V}{\pi}}$	$S = \left(\frac{4\pi A}{L^2}\right) \times 100\%$

For AM, a specific PSD with a minimum fraction of 'small' particles, is essential to maximize density. In terms of shape, only spherical powders are used for AM processes to avoid satellites, irregular morphology, or particle agglomerations [1]; because these parameters lead to a strong reduction of density and flowability. In addition, powders produced by plasma rotation electrode (PREP) have a high flowability due to their spherical shape with a minimum number of satellites [21]. However, the gas atomized powders are less expensive [22].

The sphericity factor (S), which was defined by **Equation (4.4)**, has been used to quantify the deviation from the spherical shape of a particle.

If (L) is the perimeter of a particle, the (S) value will be between 0 and 100%, and the larger the value, the more spherical the shape of the particle. In fact, the (S) value is recommended to be above 80% [3].

4.1.2 Powder Flow

Due to the complex nature of powders and the influence of handling on measurement results, the flow of powder, flowability, cannot be fully quantified with a single test [23].

An example of the limitation of the Hall flow test was illustrated by Choi et al. [3]. Two stainless steel samples were studied, and one sample failed the Hall flowmeter test, i.e. the flow was not measured. For this sample, a wide PSD with large number of small particles and low sphericity increased the interparticle frictions. Apparent and tapped densities for the non-flowable powder were lower than densities for the other flowable powder sample. However, for an SLM process, both powder samples were spread by a rake for three different layer thicknesses (25, 50, and 75 µm); but there were differences in the density of the final component. It was concluded that the Hall flowmeter, apparent and tapped densities were not sufficient tools to describe actual packing state of powder across powder bed substrate.

The Hausner Ratio (H_R) is the ratio between the tapped density (ρ_{tap}) over their related bulk density (ρ_{bulk}) [24]. The (H_R) value between 1.12-1.18 is considered to be 'free-flowing', whereas for (H_R) between 1.19-1.25, the powder only has a 'fair' flow characteristic.

In Choi's work, values for the (H_R) were calculated for both samples, where values for non-flowable and flowable powders were 1.20 and 1.13 [3], which indicates that the (H_R) does not

match the Hall flow results. This result is in agreement with similar results obtained by Hao [25]. Thus, (H_R) is not considered to be suitable for powder-bed AM applications [16].

Quantitative metrics of powder flow are a consequence of the forces that are acting as powder particles move. In the Hall flowmeter, a powder falls through a funnel due to its weight [6]. Therefore, the shear stresses are generated by the Particle/Particle and Particle/Funnel interactions. Unfortunately, an expression for the flow has not yet been determined as a function of the previous parameters. Thus, it is essential to measure the flow properties with suitable instruments [6, 8, 26].

4.1.3 The Powder Rheometer

The classical approach to evaluate the flowability is to measure the discharging time for 50 grams of powder through the funnel of the Hall flowmeter. An approach to evaluate flowability is the stability and variable flow rate (VFR) of the FT4 powder rheometer (Freeman Technology, Tewkesbury, UK) [26]. If a powder fails the flowmeter test, the powder rheometer may provide more information about the powder properties.

In the powder rheometer, the stability and variable flow rate (VFR) test is designed to obtain reproducible flow metrics, where it is a series of continuous cycles (conditioning and test). The experimental set-up for the VFR test was explained in detail by Hare et al. [27].

The first step is to fill the rheometer vessel with a powder; this vessel has a definite volume, which allows to control the volume for a studied powder. In fact, a 'splitting' mechanism at the top of the vessel was assembled to control the height of the powder column precisely, **Fig. 4.1**.

Then, the powder sample is preconditioned using the conditioning procedure for the stability and variable flow rate (VFR) test. The conditioning blade provides a gentle disturbance for the powder by using the lifting helix upwards and the slicing helix downwards, where the tip speed of impeller during the conditioning cycle is 40 mm/sec. The purpose of this preparation cycle is to generate a uniformly packed sample with a high level of reproducibility.

The flow is conducted by measuring the resistance of powder when moving the rotating stainless-steel impeller in a glass vessel filled with the powder. different impeller tip speeds are applied during the VFR test, where the tip speed for the impeller is 100 mm/sec from test 1 to 8, and the tip speeds for test 9, 10 and 11 are 70 mm/sec, 40 mm/sec and 10 mm/sec, respectively.

Axial forces and rotational torques acting on the impeller were measured [27, 28], and then the total flow energy (E_{flow}), basic flowability energy (BFE), specific energy (SE), flow rate index (FRI) and stability index (SI) are calculated [29].

The total flow energy (E_{flow}) is defined as the resistance to motion of the impeller as it rotates downwards through a volume of conditioned powder through a definite pathway [29]. The BFE is the total flow energy (E_{flow}) after the seventh test and is used as an index of the flowability.

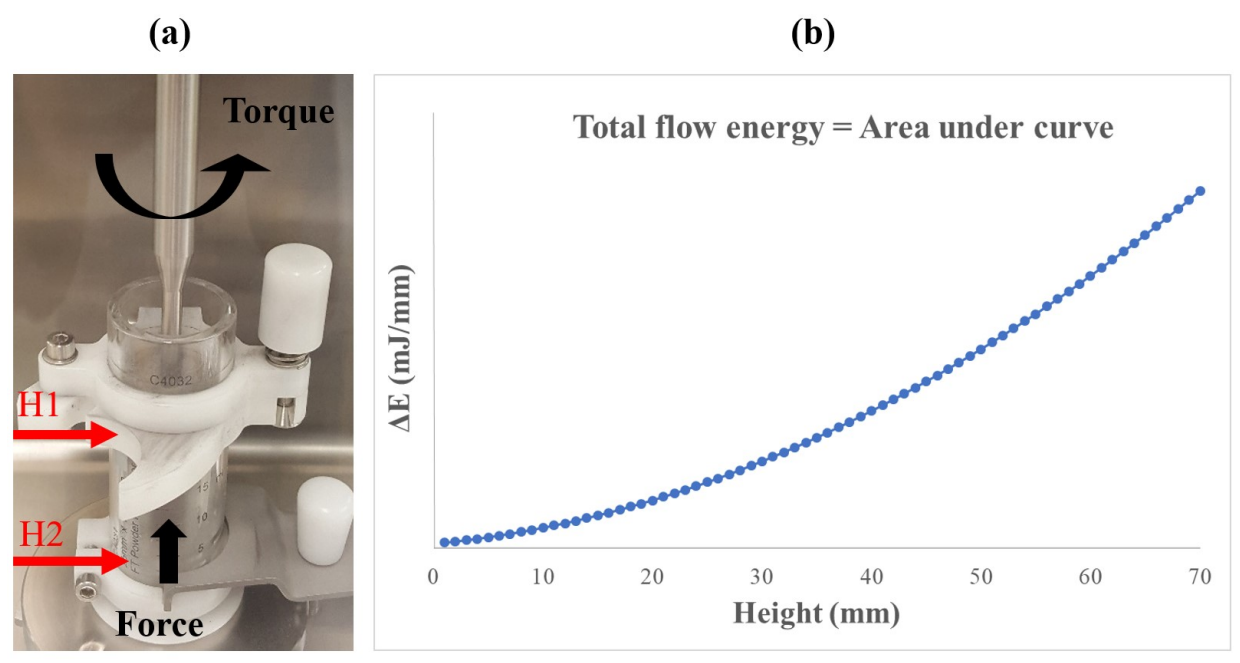


Figure 4.1: Image for the powder rheometer during the stability and variable flow rate (VFR).

The total flow energy (E_{flow}) was introduced by Hare et al. [27]:

$$E_{flow} = \int_0^H \left(\frac{T}{R \tan \alpha} + F_{base} \right) . dH$$
 (4.5)

Where T and F_{base} are the torque and vertical force applied on the impeller, R is impeller radius, α is the helix angle, and H is the penetration depth.

The stability and variable flow rate (VFR) can detect subtle differences between used and fresh powders. Where, processing has significantly increased the flow energy of the used powder [28].

The specific energy (SE) is defined as the measure of how powder flows in a low stress environment, and it is normalized against the mass of the sample [mJ/gram]. Where, the energy is derived when the impeller moves upwards from the bottom, and SE is an average of the energy

measured on the upward traverses of the 6th and 7th conditioning cycles of a standard dynamic flow test [29].

$$SE = \frac{Up \ Energy \ (Cycle \ 6) + Up \ Energy \ (Cycle \ 7)}{2 \times mass}$$
 (4.6)

The stability index (SI) compares the flow-energies measured during the downward movement for the 7th test with respect to 1st test cycle. Theoretically, a qualitative evaluation for the possible change in the flow behavior of a powder might be predicated by the value SI [30].

$$SI = \frac{Flow \ energy \ (Test \ 7)}{Flow \ energy \ (Test \ 1)}$$
 (4.7)

According to the above, the powder is defined as a stable when the value of (SI) is almost equal to 1.0. If the value of SI is greater or smaller than 1.0, this means that flow has an effect over the powder properties [30].

The flow rate index (FRI) is defined by the ratio of the flow energy of test 11 (10 mm/sec) to flow energy of test 8 (100 mm/sec) [30]. FRI has utilized to characterize the sensitivity of a powder to the change of flow rate [29].

$$FRI = \frac{Flow\ energy\ (Test\ 11)}{Flow\ energy\ (Test\ 8)}$$
 (4.8)

Theoretically, if the value of FRI is almost equal to 1.0, this means that powder is less sensitive to flow rate (a non-cohesive), and the flow energy is independent of the flow rate. On the other hand, cohesive powders are expected to be more sensitive for flow rate changes, and the value of FRI should be greater than 1.0 [30].

Three samples of stainless steel powder from the same manufacture, that had same PSD and similar flowability response in the Hall flowmeter and angle of repose, showed variable performances for an AM process. While powders A and B showed "acceptable behavior" during spreading, powder C caused poor deposition, and resulted in a low-quality final part. The evaluation of three samples with a rheometer highlighted an important difference between the two good spreading powders (A and B) and powder C. For powder C, the specific energy (SE) value was the highest in compare to

other powders, which indicated an increase of the particle/particle frictions and mechanical interlocking [31].

4.1.4 Powder Spreading

Spreadability is disturbed by mass of powder, humidity, and van der Waals attractive forces [16, 4]. Berretta et al. [10] showed the importance of layer compactness and smoothness for a new grade of polymer (PEEK) powder.

One of the spreading outcomes is powder layer density, which strongly affects final part properties. Powder layer densities for two types of gas atomized 316L stainless steel powders, one which flowed and one which did not flow, were evaluated by Choi et al. [3] for three layer thicknesses. It was found that both powders showed specific layer densities which had values between tapped and apparent densities and that powder layer density is independent of the layer thickness range used [3].

Powder tends to segregate (separate the particles) owing to differences in particle properties, such as the shape, size, and density (e.g. smaller particles cluster together) [32]. The level of segregation in a layer of powder might be taken as a measure of spreadability. For the additive manufacturing powder bed processes, the segregation of powder in the powder bed has not been studied extensively. It was reported that powder particles according to their size distribution segregated depending on the location in the bed [33]. Whiting and Fox [19] examined the segregation in the powder bed and found a slight change in PSD at different elevations of the powder in the bulk containers (hopper) and minor changes in PSD at different locations along the spreading direction for a powder bed.

Despite the above findings, it is still not clear how to distinguish between good and bad layers. Luckily, two powder bed parameters were proposed by Haeri et al. [34], where the solid volume fraction (a description of the packing factor) and the surface roughness (R_a) (μ m) of powder bed were used to evaluate the effectiveness of powder spreading. A good quality of powder layer is determined by a high solid fraction (high value of the packing factor) and low value of the surface roughness (a smooth surface) [34]. However, the value of solid volume fraction is replaced with the packing factor (\emptyset) because the packing factor (dimensionless packing density) has been widely used for the powder packing [9, 35].

The packing factor (Ø) is defined as the ratio of powder bed layer density to solid density for the same material [36]. Thus, the packing factor (Ø) is an index for the packing quality for a single powder (SL) layer in PBF; the higher packing factor causes a denser sintered part [28].

Tap density (ρ_{tap}) provides an indication for powder flowability from measurements of the change in bulk density induced by one directional tapping [28]. For the same powder, Van den Eynde et al. [36] defined the maximum packing factor (\emptyset_{max}) as the ratio of tap density to solid density. This ratio provided the upper limit for the packing factor (\emptyset) and it was limited by particle morphology and size distribution [36].

$$\left(\emptyset_{max} = \frac{\rho_{(tap)}}{\rho_{(solid)}}\right) \ge \left(\emptyset = \frac{\rho_{(SL-powder)}}{\rho_{(solid)}}\right)$$
 (4.9)

A recent work was introduced by Alchikh-Sulaiman et al. [9] to develop a methodology to generate a single layer (SL) of powder by applying the mechanism of contact-sintering (CS) and measure the related packing factor and surface parameters (RMS (μm) and S_{dq} ($\mu m/mm$)) with the assistance of the coherence scanning interferometry (CSI). In addition to that, this paper has proposed to include the Skewness (S_{sk}) parameter with previous two surface parameters to evaluate the spreading for SL samples.

Contact-sintering (CS) is a simple, low-cost process to freeze the powder particles in the as-spread condition, with minimal changes in the morphology of particles and packing characteristics. The CS is based on two sequential steps. The 1st step is to heat the powder using the electron beam (EB) inside a vacuum chamber from an initial temperature (e.g. 20°C) to several hundred degrees Celsius (T_{CS}) in a short period of time without a direct contact between the powder and EB to avoid smoking [35]. Where, the EB will hit the outer side of the substrate. The 2nd step is to maintain this (T_{CS}) temperature for 4 to 6 minutes only.

Considering the simple substrate geometry and the limited amount of powder needed per tests, the operational cost of generating many samples was less than the cost of a complete powder AM build.

For this research paper, the applicability of the stability and variable flow rate (VFR) to distinguish between different powder lots are examined. A technique is described to investigate the

tribocharging effect in which the contacts between interacted particles [37] are generated by the powder rheometer and the charging effect on the flow is investigated using the value of BFE [mJ].

The tribocharging effect is expanded to cover the following components at the powder rheometer: the vessel material (borosilicate glass and stainless steel), and powders. This research paper will address the results of CS for powders with different flow behavior, and the effect of tribocharging is correlated with powder spreading.

4.2 Experimental Methods

4.2.1 Instruments

4.2.1.1. Coherence Scanning Interferometry (CSI)

Noncontact optical profilometry ($Zygo^{TM}$ NewView 8000) using coherence scanning interferometry (CSI) proposes a dependable, fast and appropriate technique of performing surface roughness measurements, characterizations of the contact-sintered SL of powders, and large area image stitching with 3D surface visualization. The CSI contains scanning the surface, through the Z-axis, using the white-light, and measuring the degree of coherence (visibility of the interference fringes) at each pixel in the image [38]. The measurements do not require an initial preparation and the measured sample does not have any destruction at the end of test. Coherence scanning interferometry (CSI) was applied to measure various surface parameters, such as root-mean-square roughness RMS (μ m), surface roughness R_a (μ m) [39], Skewness parameter S_{sk} [40] and the root mean square gradient of the surface S_{dq} (μ m/mm) [41].

The reference to conduct the surface texture parameters (R_a , RMS, S_{sk} and S_{dq}) was chosen to be a plane form remove. Surfaces are measured with a 2.75x Michelson lens under an operating condition correlating to a 40 nm bandpass F2 filter [41]; the scan length is extended to 400 μ m and the bottom is defined as a scan origin. Also, the related acquisition time for a definite scan length is 53 sec/grid, and the configuration stitch option with 2.75x lens is used to scan the complete surface

4.2.1.2. SEM

The Hitachi SU3500 scanning electron microscope SEM operating at 15 - 20kV was used, where SEM provides gives quasi-3D images at higher magnifications and resolutions. For the metallic powders, images were obtained at the secondary electron SE mode, where low energy electrons scattered by the particle surfaces form high-resolution images of surface topography.

4.2.1.3. Laser Diffraction for Particle Size Measurement PSD

Laser diffraction (LA-960 Analyzer, Horiba, Japan) was used to measure the particle size distribution PSD for three powder lots for Ti-6Al-4V, where angular distributions of the scattered light generated by a laser beam passing through a diluted dispersion of particles were the raw data. Total diffracted light patterns were used to calculate the PSD, and the surface area was determined from the diameter distribution of spherical particles. Thus, laser diffraction needed a dispersion of particles into a liquid (isopropanol). If proper dispersion was obtained, the wet-laser-diffraction method was fast and repeatable. To obtain these measurements, the morphology of particles was assumed to be spherical. This assumption was satisfied with gas and plasma atomized powders [33]. Also, the refractive indices for titanium and isopropanol were 2.50 and 0.72, respectively.

4.2.2 Experiments

The experiment of SL powder was performed by a consistent 'spreading' technique and then 'contact-sintered', i.e. sintered up to the point immediately prior to neck formation, by electron beam, to 'freeze' the packed layer. This was then examined by CSI to examine the spreading characteristics, such as powder height and packing factor, which evaluated 'spreadability'. Thus, a correlation between powder characteristics and spreadability was obtained.

4.2.2.1. Materials

Titanium alloy Ti-6Al-4V (grade 23) powder was utilized for three CS experiments. The PSD for this powder is 45 -106 μ m, and according to the powder certificate, the flow rate, apparent and tap densities were 26 sec, 2.50 g/cm³ and 2.80 g/cm³, respectively.

Also, three different lots of titanium alloy Ti-6Al-4V (grade 23) were used to conduct the powder rheometer tests. The three lots have similar PSDs, apparent and tap densities values; where the PSD was 15 - 45 µm, and the apparent and tap densities were 2.50 g/cm³ and 2.80 g/cm³, respectively. However, the three lots performed differently at the Hall flowmeter (**Table 4.2**), and powder lot 2 had a poor flow.

In addition, Ti-6Al-4V (grade 5) and Inconel 718 substrates with 1.53 mm thick plates, were laser cut into approximately 50 mm x 50 mm sections, by Baoji Magotan Nonferrous Metals Co. (Shaanxi, China), and were used as substrates on which the powders were spread.

Table 4.2: The flow times for the three Ti-6Al-4V (grade 23) lots.	Table 4.2:	The flow	times for	or the three	Ti-6Al-4V	(grade 23)	lots.
--	------------	----------	-----------	--------------	-----------	------------	-------

Ti-6Al-4V (Grade-23) Lot number	Hall flowmeter (sec/ 50 gram)
1	30
2	> 180
3	25

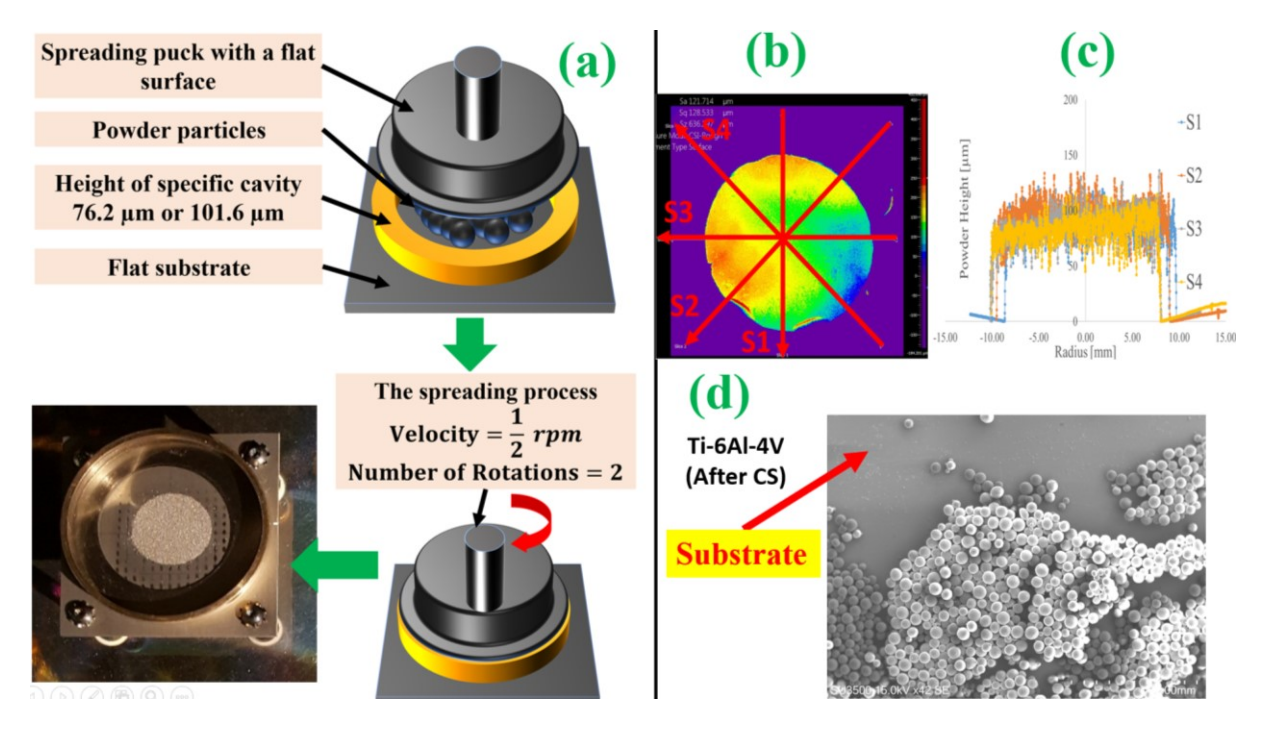


Figure 4.2: (a) A diagram for the set-up and the procedure to prepare a SL of powder, and an upper image for a SL powder sample before the CS process, (b) with the assistance of CSI, the measured SL of Ti-6Al-4V (grade 23, PSD: $15-45 \mu m$, powder lot 2) sample with color contour of 20 μm /div and 4 cross-sections,(c) the extracted height profiles according to the 4 cross-sections, and (d) an SEM image for the same CS measured sample (The edge between powder-bed and substrate).

4.2.2.2. Procedure to Prepare a Single Layer (SL) of Powder

To spread the powder over this substrate, a metal puck of stainless steel 316L was fabricated. A high degree of flatness (\pm 9 μ m) and smoothness (low value for the surface roughness R_a) was obtained for this puck with a manually operated grinding machine. Powder was slowly poured into a funnel over the substrate for half a minute. To simulate spreading at AM process when the build plane is moved downwards by a definite height to allow the spreading of a layer, two specific cavities (101.6 μ m or 76.2 μ m) were introduced (**Fig. 4.2-a**); this specific cavity was applied to control the height between the substrate and spreading puck.

The puck was then placed gently on top of the cavity for half a minute before the rotation. To spread the powder over the prepared substrate, the flat puck was manually rotated for two complete rotations, with an angular velocity about 0.5 rpm, (**Fig. 4.2-a**). By applying powder according to previous set-up and procedure, powder was spread in a circular shape (**Fig. 4.2-a**). Note that the thickness of this 'single' layer is approximately two or three particles thick [9, 42].

To calculate the density for a SL of powder, the weights of substrate and sample of powder were recorded. After CS, the total weight of sample (substrate + CS powder) was measured. Thus, the utilized mass of powder (m_{SL}) was determined, and the shape of the SL was assumed to be a thin disc, (Fig. 4.2-a). Surface topography of SL was measured by CSI, as presented in (Fig. 4.2-b).

The height profiles for 4 cross-sections (slices) lines were plotted with respect to the average diameter for the sample (**Fig. 4.2-c**). As a result of that, the maximum powder height (h_{max}) was determined (**Fig. 4.2-c**). The area ($area_{SL}$) of the best fit circle to SL circumference was determined by the measured surface (**Fig. 4.2-b**). Thus, SL density ($\rho_{(SL-powder)}$) was calculated by **Equation (4.10)**.

$$\rho_{(SL-powder)} = \frac{m_{SL}}{h_{max} \times area_{SL}}$$
 (4.10)

4.3 Results and Discussion

4.3.1 Surface Roughness Validation Measurements for Gauge Block (Zygo Vs. Profilometer)

A gauge block is a metallic block that has been precision ground and lapped to a specific thickness. It is utilized to produce precision lengths and has two opposing faces ground precisely flat and parallel. It was scanned with the Zygo to validate the profile measurements and surface roughness values and a plane-form remove was applied for this measurement.

A Bruker profilometer measurement was utilized to measure the (R_a) surface roughness for the gauge block; the (R_a) was 5.32 nm. The reference area was fixed (Test 1), while the measured area (Test 2) was increased to determine its related surface roughness value.

The surface roughness (R_a) values for a definite region "Measured Area" increases proportionally with its related area (**Fig. 4.3-c**).

For $(4.54 \times 10^5 \ \mu m^2)$ definite area, the related (R_a) value was 4.0 nm and it was close to the profilometer measurement. Thus, the same area was used to determine the surface roughness (R_a) value for other surfaces.

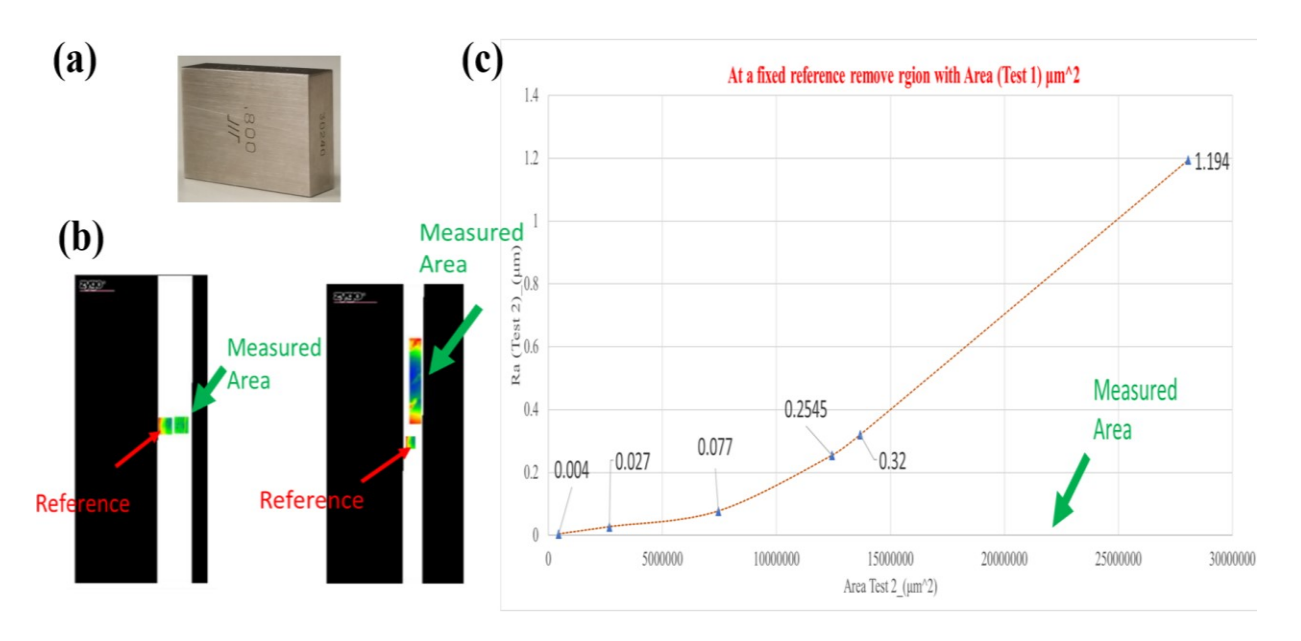


Figure 4.3: (a) Image for the gauge block, (b) Examples of the *Ra* measuring process with Zygo, and (c) Surface roughness *Ra* for measured area as a function to its related area (Test 2) at a fixed reference remove region (Test 1).

4.3.2 Powder Rheometer: Stability and Variable Flow Rate (VFR)

In this work, the VFR test is conducted by measuring the resistance of powder when moving the rotating stainless-steel impeller (23.5 mm diameter) in a glass vessel (borosilicate glass, fire polished, 25 mm internal diameter, 51 mm height) filled with the powder, **Fig. 4.1-a**.

Three different lots have similar PSDs and a spherical morphology, but it cannot explain why lot 2 has a poor flow. The D_{10} , D_{50} and D_{90} for the three lots were measured by laser diffraction for particle size measurement PSD. Each powder lot was measured five times and the results were presented in **Table 4.3**.

Table 4.3: The D_{10} , D_{50} and D_{90} for the three powder lots

Ti-6Al-4V	D ₁₀ [μm]	D ₅₀ [μm]	D ₉₀ [μm]
1	20 ± 1	28 ± 1	43 ± 2
2	22 ± 1	30 ± 2	44 ± 3
3	19.8 ± 0.2	31.5 ± 0.2	53.3 ± 0.16

From **Table 4.3**, three lots have almost same D_{10} and D_{50} and a slight variation in D_{90} for lot 3. However, these measurements did not explain the poor flow behavior for lot 2. As a result of that, the stability and variable flow rate (VFR) test, which can be named as the dynamic test, was applied for the three lots for two separate rounds (**Fig. 4.4**). At the beginning of each test, a fresh powder sample was utilized to obtain the VFR test.

From **Table 4.4**, the FRI value for powder lot 2 was the highest in compare to the lots 1 and 3. Where, the values of FRI for round 1 and 2 were 1.26 and 1.22, respectively. Based on the definition of FRI [30], powder lot 2 was more cohesive with respect to other lots, and the three powder lots were cohesive, because their FRI values were greater than 1.0.

For lot 2, the values of SI for round 1 and 2 were 1.01 and 0.94, respectively. Based on [30], powder lot 2 was a stable powder, which means the flow had an effect over the powder properties for powder lots 1 and 3. However, it was not clear if the stability index (SI) could explain the poor flow for lot 2.

Table 4.4: Different VFR tests for three powder lots for two separate rounds.

		R	ound 1		Round 2					
Powder	BFE	SI	FRI	SE	BFE	SI	FRI	SE		
lot	[mJ]			[mJ/gram]	[mJ]			[mJ/gram]		
1	272	0.92	1.19	2.08	294	0.87	1.10	2.01		
2	315	1.01	1.26	2.48	310	0.94	1.22	2.42		
3	296	0.89	1.15	2.54	277	0.89	1.13	2.43		

The basic flow energy (BFE) for three lots were plotted with respect to the number of test (**Fig. 4.4-a** and **Fig. 4.4-b**). Based on that, the lot 2 had the highest energy values in-compare to lots 1 and 3, and the BFE values for rounds 1 and 2 were 315 and 310, respectively. It could be explained that more energy was required to rotate and move the impeller inside the powder lot 2. Surprisingly, the SE values for lots 2 and 3 had not followed the same trend as other test parameters. The SE value for lot 3 had the highest value in compare to other powders for round 1 and had an almost equal value for powder lot 2 for round 2.

According to **Fig 4.4**, the VFR test was used to deliver more information about the powder characteristics for three powder lots with different flow behavior, and the value of BFE agreed with the Hall flowmeter measurements.

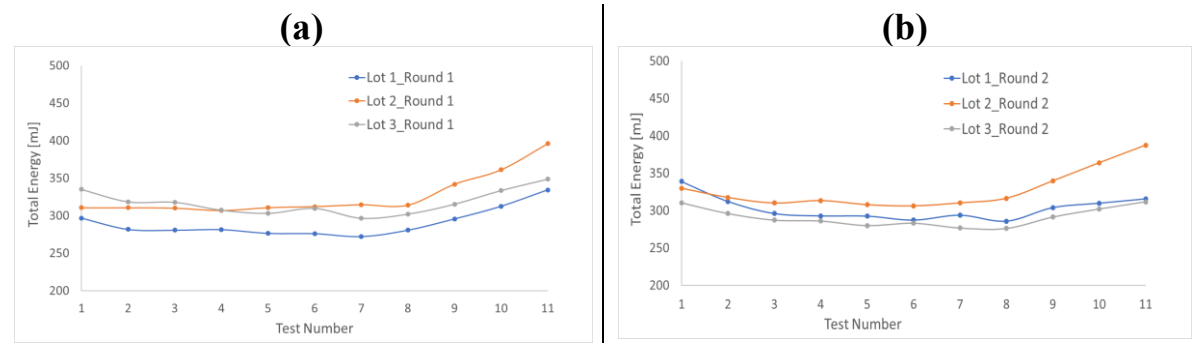


Figure 4.4: The graphs of the VFR test for three powder lots, (a) round 1 and (b) round 2.

To detect possible variations at the VFR test (Dynamic test) and to examine the repeatability of results, the following experiment was designed with powder lot 1 for three fresh samples (**Fig. 4.5**).

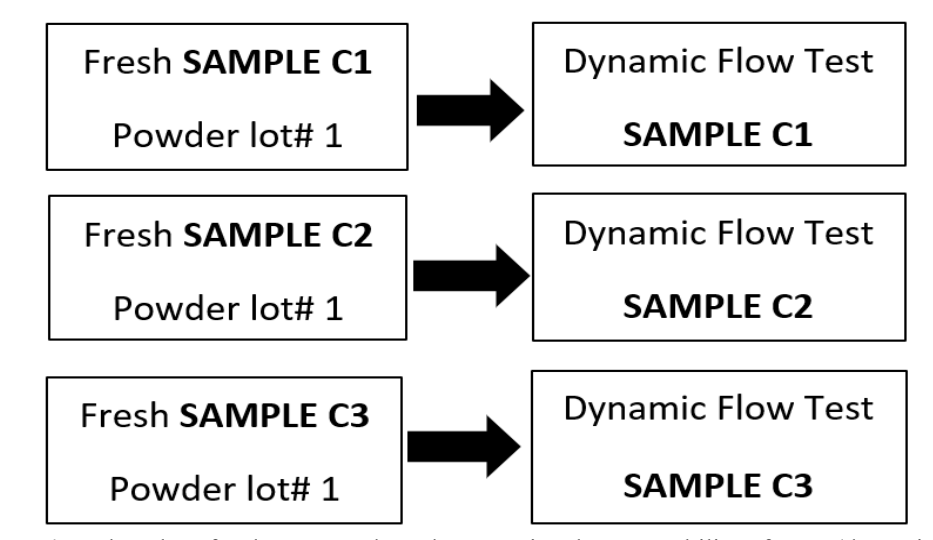


Figure 4.5: Flowchart for the test conducted to examine the repeatability of VFR (dynamic) test

Table 4.5 provides the dynamic outputs for the samples C1, C2 and C3, where the conditional bulk density $\rho_{(CBD)}$ for the three samples was 2.64 g/cm³. The maximum differences for BFE, SE and FRI were 5.6%, 4.3 % and 2.0 %, respectively.

Based on that, the stability and variable flow rate (VFR) test showed a good repeatability and high level of consistency for the three samples.

Table 4.5: The stability and variable flow rate (VFR) test outputs for the three samples from powder lot 1

VFR test outputs	Sample C1	Sample C2	Sample C3
CBD: Conditioned bulk density [g/cm ³]	2.64	2.64	2.64
BFE: Basic Flow Energy [mJ]	318.4	318.9	336.2
SE: Specific Energy [mJ/g]	2.33	2.34	2.42
FRI: Flow Rate Index	1.29	1.26	1.26

4.3.3 The Effect of Vessel Material on the Flow of Powder

The powder rheometer is equipped with a borosilicate glass vessel; the friction forces between (powder particles/internal surface of vessel) and the possible tribocharging effects (exchange of electrons) could be interfering with the obtained BFE values.

To distinguish the effect of the vessel material on the flow energy, a custom-made stainless steel vessel with exact same dimension with a rheometer borosilicate glass was fabricated (**Fig. 4.6-a**). Powder lot 3 was used to compare the differences between the borosilicate glass and stainless steel vessels; the VFR flow for these two experiments was plotted, as shown in **Fig. 4.6-b**.

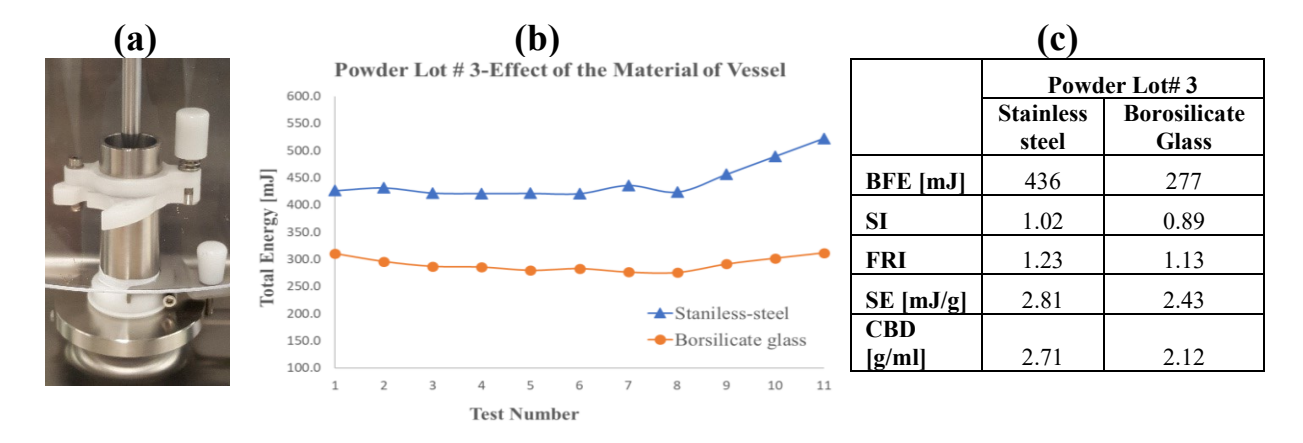


Figure 4.6: (a) Image for the custom-made stainless steel vessel, (b) the effect of the vessel material on VFR test for powder lot 3 samples, and (c) the values for obtained test parameters.

According to the values obtained in (**Fig. 4.6-c**), the stainless steel vessel affected the flow behavior of powder particles in-compare to the borosilicate glass. Where, there was a shift for the BFE values and the related VFR graphs for the stainless steel vessel.

The values for SE (mJ/gram) did not changed significantly which might indicate that SE was independent of the vessel material and SE was more related to powder properties and environmental conditions.

The powder particles are spread by rake over a metallic substrate to generate a SL of powder in AM process, and the particles slide and rotate over the internal surface of the stainless steel vessel during the stability and variable flow rate (VFR). For this reason, the VFR test obtained with the stainless steel vessel could simulate the spreading mechanism for particles in the AM powder bed process.

To investigate the performance of Ti-6Al-4V (Lot 3) with many repeat experiments, the powder was left inside the stainless steel vessel and no-splitting was obtained after the first experiment. As mentioned earlier, different impeller tip speeds were applied for one VFR test (100 mm/sec, 70 mm/sec, 40 mm/sec and 10 mm/sec). For this experiment, a 'repeat' (cycle) is based on the mentioned '11 tests' at different tip speeds. A series of 'repeats' should be applied to the studied powder until the value of BFE is plateaued. However, the total number of 'repeats' was 6 times, and the values of BFE was kept constant.

Figure 4.7-a plotted the values of BFE against the number of repeats. Also, the values of different VFR test parameters were recoded, Fig. 4.7-b. Where this powder showed repeatability for six repeats. As a result of that, the effect of tribocharging for Ti-6Al-4V (PSD: 15 - 45 μm) was not observed during the VFR test inside the stainless steel vessel. For this powder with same PSD, the tribocharging will not be expected to occur during the powder spreading for AM-PBF processes.

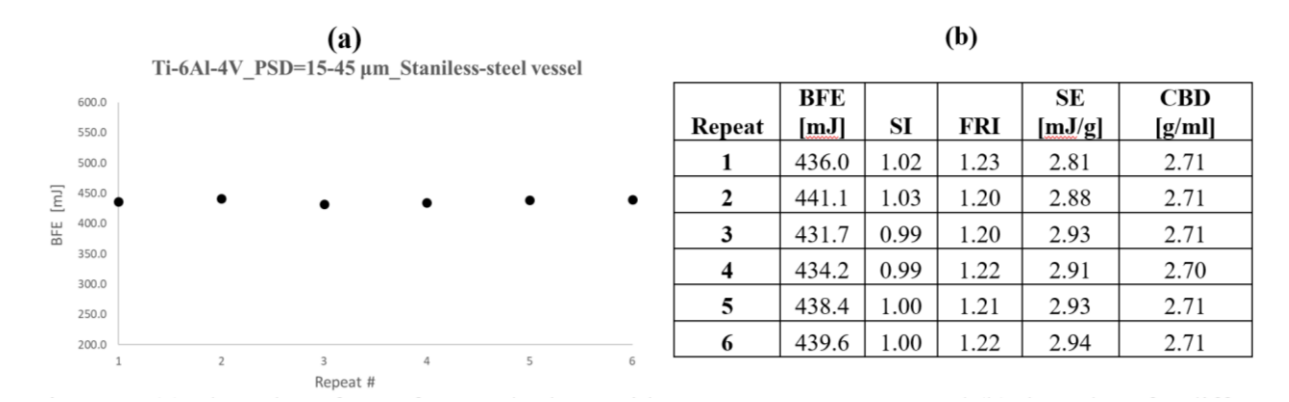


Figure 4.7: (a) The value of BFE for powder lot 3 with respect to number of repeats, and (b) the values of different VFR test parameters for the same powder were obtained for 6 repeats.

4.3.4 The Effect of Heat Radiation on Substrate Topography

Three substrates from Ti-6Al-4V grade 5 (samples: a, b and c), and a substrate from Inconel 718 were used for the following study, where the effect of heat treatment on the substrate topography was examined. The source of heat was the electron beam (EB) in the vacuum chamber, and the

heating method was the same procedure for CS experiments. (i.e., the substrate is heated using the electron beam (EB) inside a vacuum chamber from an initial temperature (20° C) to $(T_{CS} = 700^{\circ} \text{ C})$ in a short period of time. This (T_{CS}) is then maintained for 4 to 6 minutes only). The possible deformation of a substrate can be caused by, (i) the internal residual stresses, and/or (ii) the fixture to hold the substrate (**Fig. 4.8**).



Figure 4.8: The fixture to hold the substrate with 4 legs.

The average surface roughness (R_a) provides an overall description of the height variations. However, the (R_a) is not sensitive towards small variations in the height profile and cannot express the waviness of a surface [40]. The value of (R_a) might not associate with the substrate topography for the spreading mechanism, and the (R_a) parameter is a 'shapeless' that considers the height of any surface feature within a spatial wavelength bandwidth selected by a cut-off filter [43].

Some of the hybrid parameters are generated by 3D non-contact profilometer; those parameters could assist to predict the mechanical performance of a substrate based on its surface texture (substrate topography for the spreading mechanism). For a definite area, the hybrid parameters include the spacing features of the surface textures and amplitude. The root mean-square surface slope (S_{dq}) is one of these parameters, where the areal ISO hybrid (S_{dq}) parameter is a measurement of the slopes that cover a surface and is used to distinguish between surfaces with similar roughness values [44]. Also, (S_{dq}) is affected by spacing and texture amplitude.

An increase in the (S_{dq}) value indicates of a deterioration in the surface roughness, where this deterioration might not be detected from the value of (R_a) alone [43]. The value of (S_{dq}) is zero for a flat surface.

Skewness (S_{sk}) parameter is a non-Gaussian distribution of the roughness profile and it measures the symmetry of the variation in a surface with respect to its mean. In other words, (S_{sk}) describes the degree of symmetry for surface heights about the mean plane. Also, (S_{sk}) has a sensitivity towards the high-peaks or deep-valleys in the surface [40].

The sign of (S_{sk}) : (Ssk > 0) will describe a spike above a flatter average (the predominance of peaks), and (Ssk < 0) will define a deep valley at a flat surface (the predominance of valley structures). For a measured surface, if the (Ssk = 0), this surface has a symmetrical height distribution [40]. However, **Appendix A4** provides the definitions and equations for these surface parameters.

To compare between different substrates or to evaluate the deformation due to heat effect, this work has proposed to use the following three surface parameters: (i) surface roughness (R_a) (μ m), (ii) Skewness (S_{sk}) , and (iii) (S_{dq}) parameter (**Table 4.6**).

	Substrate (a)		Substrate (b)		Substrate (c)		Substrate (d)	
	Before	After	Before	After	Before	After	Before	After
$R_a(\mu m)$	2.31	1.12	2.39	2.86	1.53	1.41	4.14	5.25
S_{sk}	-1.42	0.32	-0.46	-0.31	0.16	-0.56	2.50	1.27
$Sdq\left(\frac{\mu m}{mm}\right)$	11 9	12 3	20	18.5	24.7	17.6	42.2	42

Table 4.6: The surface parameters for the studied substrates.

Based on the values of surface parameters in **Table 4.6** and **Fig. 4.9**, there was a change in the topography before and after heat treatment for the substrate (a). This change was captured clearly at the change of (S_{sk}) sign from negative to positive, which indicated that convexity of surface was improved towards a flatter surface, **Fig. 4.9-a**. No major variation at (S_{dq}) and (R_a) values were detected.

Regarding the values of three parameters for substrate (b), the substrate did not have a major topography change, **Table 4.6**. This result agreed with visual observations for **Fig. 4.9-b**, where the region of blue area has maintained almost same area before and after the heat treatment.

For substrate (c), there was a change at the topography after the heat treatment, **Table 4.6**. Where, the (S_{dq}) value decreased and (S_{sk}) became negative which defined a valley at a flat surface; this result agreed with visual observations for **Fig. 4.9-c**.

Finally, for the Inconel 718 substrate (sample d), no-change at the topography before and after the heat treatment was captured in **Table 4.6**. The three surface parameters agreed with the two measured surfaces, **Fig. 4.9-d**.

Although the optimal surface parameters to maintain consistency during the powder spreading are not defined yet, low values for (S_{dq}) , (R_a) , and $(Ssk \approx 0)$ are required for a substrate.

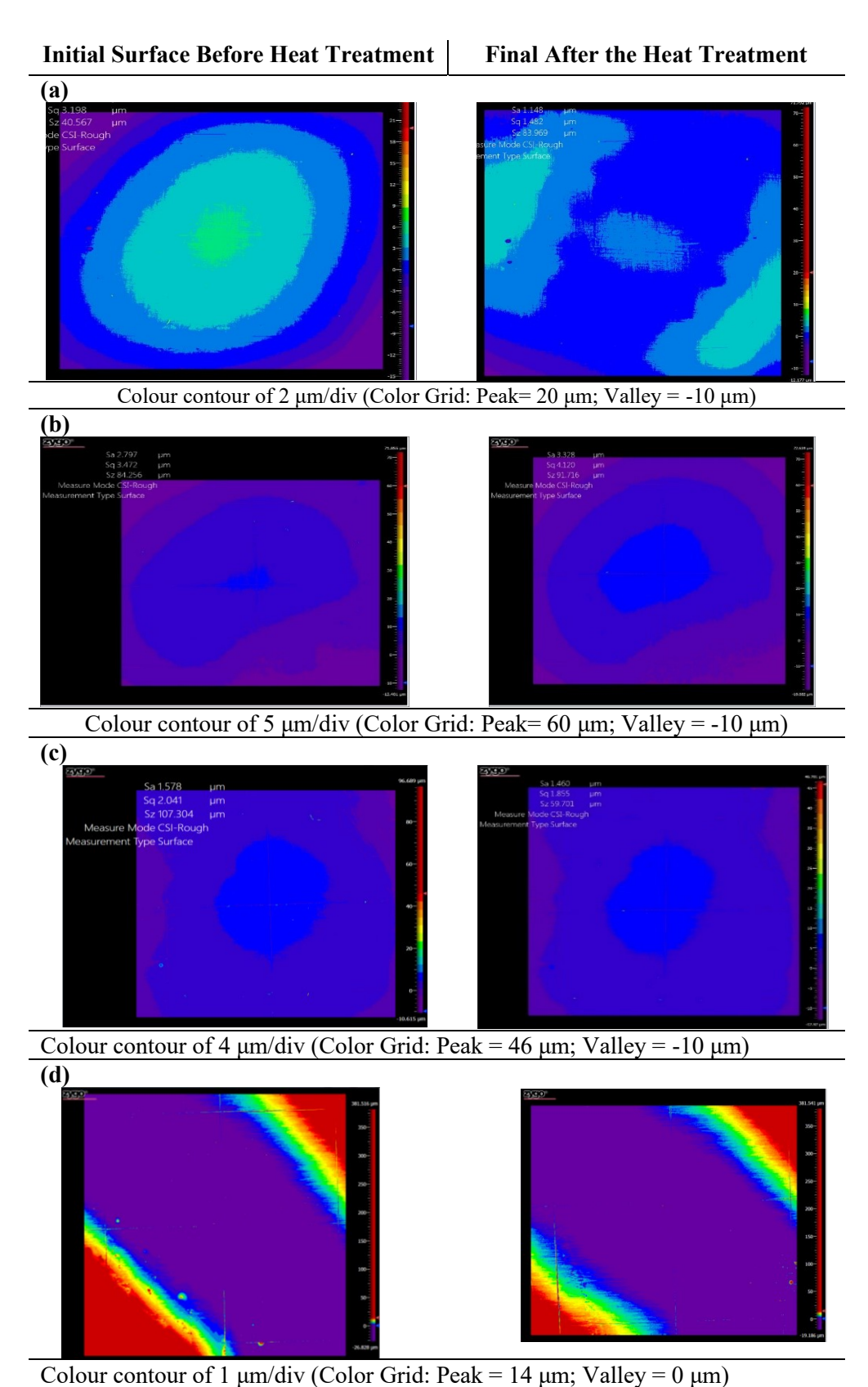


Figure 4.9: Measured substrates for 3 samples (a, b and c) for Ti-6Al-4V, and Inconel 718 (sample d) before and after the heat treatment.

4.3.5 The Effect of Layer Thickness on the Packing Factor

To evaluate spreadability for different powders and to correlate powder spreading with flow, the packing factor (\emptyset) was calculated for the following samples. If the solid density for Ti-6Al-4V was 4.42 g/cm³ [45], the maximum packing factor (\emptyset_{max}) for Ti-6Al-4V was 63.3%, **Condition** (4.9).

Two SL samples from powder lot 2 (PSD: 15 -45 μm) that had a poor flow were spread over Inconel 718 and Ti-6Al-4V (grad 5) substrates (**Fig. 4.10**). In addition to that, three samples of SL from Ti-6Al-4V (PSD: 45 -106 μm) were contact-sintered over Inconel 718 substrates.

From **Fig. 4.2-d**, the SEM image for SL of powder sample showed that particles maintained their spherical morphology at the end of CS process.

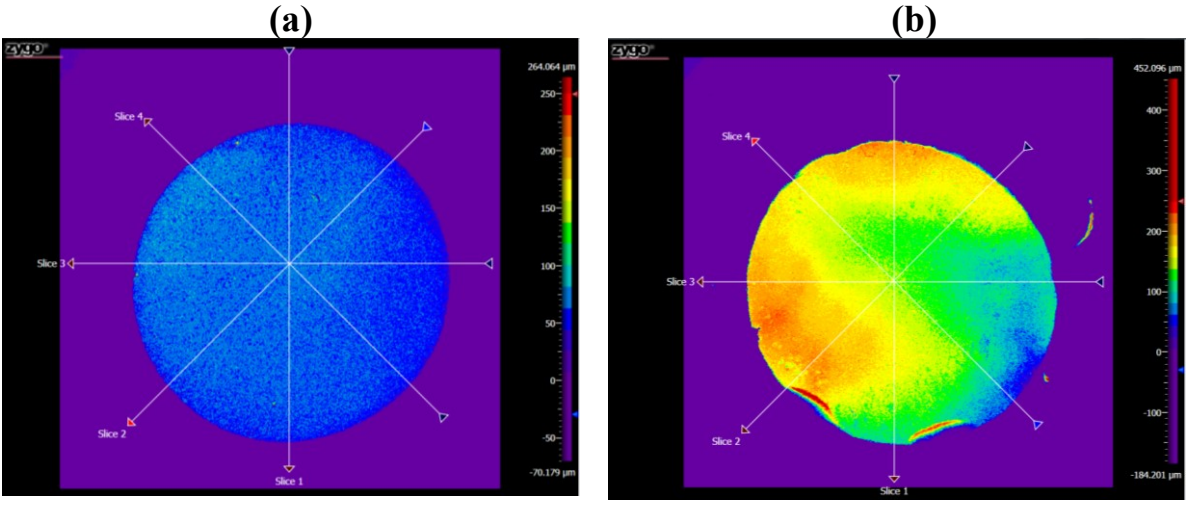


Figure 4.10: Two SL samples from powder lot 2: (a) sample 4 with Ti-6Al-4V substrate, and (b) sample 5 with Inconel 718 substrate; both surfaces were obtained with color contour 20 μm/div.

After CS process, the SL samples were measured by CSI, and the values of (\emptyset) were provided in **Table 4.7**.

Based on **Table 4.7**, the powder lot 2, that has a poor flow behavior was spread and generated two SL samples with the packing factors 56.8% and 38.8%. According to three surface parameters obtained in **Table 4.7**, the surfaces of SL samples had very similar textures, where the sample with higher packing factor had a smoother surface ($RMS = 11.4 \mu m$).

Based on this experiment, the powder spreading, and flow are two different processes. In other words, if a powder has a poor flow, or fail the flow test, this powder can still be spread with a high value of packing factor.

Interesting fact, the powder with larger PSD (samples 1, 2 and 3) generated three SL samples. However, sample 4 had the highest packing factor value with respect to all samples.

The maximum powder heights for samples 1, 2 and 3 were 185 μ m, 200 μ m and 143 μ m, respectively. These heights were higher than the heights of specific cavities (101.6 μ m and 76.2 μ m). Also, the maximum heights for samples 4 and 5 were higher than the 101.6 μ m specific cavity. This could be explained that cohesive forces between particles are stronger than shear forces during spreading with a puck, where the cohesive forces for this process was mainly the tribocharging forces.

Based on **Table 4.7**, the surfaces for samples 1, 2 and 3 had similar textures, where the sample with the highest packing factor had the smoothest surface texture ($RMS = 43 \mu m$). Same observation for the average surface roughness was captured between samples 4 and 5.

Table 4.7: Packing factors for the different powder samples with related surface parameters for the SL of sample.

									Meası	ired SL a	nfter CS
$T_{cs} \approx 700$ °C, Time= 4-6 min	Sample	Substrate	Height of Specific Cavity (µm)	Mass (gram)	Area (mm²)	Maximum height (μm)		Packing fraction (Φ *100%)	RMS (µm)	Ssk	Sdq μm/mm
Ti-6Al-4V	1		101.6	0.150	386	185	2.10	47.5	50	-0.08	2826
(PSD: 45 -106 μm)	2	Inco718	101.6	0.104	263	200	1.98	44.7	49	-1.38	1511
, ,	3		76.2	0.055	182	143	2.11	47.8	43	-0.87	2675
Powder lot 2 (PSD: 15 -45	4	Ti-6Al-4V (grad 5)		0.077	260	118	2.51	56.8	11.4	-0.80	814
μт)	5	Inco718	101.6	0.208	357	340	1.71	38.8	21.6	-2.0	851

4.4 Conclusions

This paper provided an opportunity to understand more about the powder spreading for powders with different particle size distributions.

The applicability and repeatability of the stability and variable flow rate (VFR) were examined. Effect of tribocharging was studied with the following components at the powder rheometer: the vessel material (borosilicate glass and stainless steel), and powders. The spreading of powder was correlated with the VFR test in the stainless steel vessel.

The values of SL density and packing factors were calculated for two-layer thicknesses.

This work proposed three surface parameters to evaluate the substrate topography, and these parameters were used to evaluate the spreading quality for SL samples. The results of contact-sintering for SL samples were discussed for different flow behaviors.

Appendix (A4)

The following surface parameters $(R_a, RMS, S_{dq} \text{ and } S_{sk})$ were utilized extensively in this thesis. According to that, the following appendix provides their definitions and equations.

The surface roughness (R_a) , or arithmetic average height parameter is the average absolute deviation of the roughness irregularities from an average line over the sampling length (L) [46]. It is expressed in the unit of height (μ m or μ in). However, the (R_a) is not sensitive towards small variations in the height profile and cannot express the waviness of a surface [40].

However, Gadelmawla et al. [46] provided the mathematical equation of this parameter.

$$R_a = \frac{1}{L} \int_0^L |y_{(x)}| \, dx$$
 (A4.1)

The root mean square roughness (RMS) is an essential surface parameter to evaluate the roughness, where it presents the standard deviation from an average line. In fact, it has a better sensitivity to large deviations in compare with the (R_a) parameter [46]. It is also expressed in the unit of height (μ m or μ in).

Where, Alshibli and Alsaleh [47] provided the mathematical equation of this parameter.

$$RMS = \sqrt{\frac{1}{L} \int_0^L (y_{(x)})^2 . dx}$$
 (A4.2)

The root mean-square surface slope (S_{dq}) is one of the hybrid parameters that are calculated by 3D non-contact profilometer, where the ISO 25178-2 areal hybrid parameter is a measurement of the slopes that cover a surface [41]. In fact, (S_{dq}) is applied to differentiate between surfaces with similar roughness values [44].

In the Cartesian coordinate system on a plane (x, y), the gradient of a surface is described by $\left(\frac{\partial z}{\partial x}\right)$ and $\left(\frac{\partial z}{\partial y}\right)$. If (A) is the projected area of the measured surface, the root mean-square surface slope (S_{dq}) is then calculated by **Equation (A4.3)** [44]:

$$S_{dq} = \sqrt{\frac{1}{A} \iint \left(\frac{\partial z^2}{\partial x} + \frac{\partial z^2}{\partial y}\right) dx. dy}$$
 (A4.3)

Although (S_{dq}) is a unitless positive value, but it is usually expressed in $(\mu m/mm)$ [44]. On the other hand, the (S_{dq}) value is zero for a 'flat' surface, and this parameter is controlled by spacing and texture amplitude. An increase in the (S_{dq}) value indicates of a deterioration in the surface roughness, where this deterioration may not be discovered from the R_a value alone [43].

Finally, the skewness parameter (S_{sk}) is a non-Gaussian distribution of the roughness profile and it measures the symmetry of the variation in a surface with respect to its mean. In other words, (S_{sk}) describes the degree of symmetry for surface heights about the mean plane. This parameter has a sensitivity towards the high-peaks or deep-valleys in the surface [40].

If (A) is the sampling area, the skewness is then calculated by **Equation (A4.4)** [44]:

$$S_{sk} = \frac{1}{\left(S_q^3\right)} \left(\frac{1}{A} \iint Z(x, y)^3 \, dx. \, dy\right) \qquad (A4.4)$$

To obtain the skewness value from the previous equation; the (S_q) parameter should be calculated first, where it is defined as the height parameter obtained from the (RMS) of the 'ordinate' values inside the sampling area (A) [41].

Where, the (S_q) parameter is defined by **Equation (A4.5)** [44]:

$$S_q = \sqrt{\frac{1}{A} \iint Z(x, y) \, dx. \, dy} \qquad (A4.5)$$

The sign of the skewness parameter (S_{sk}) was discussed by Sedlacek et al. [40]:

- If the (Ssk = 0) for a measured surface, this surface has a symmetrical height distribution.
- (Ssk < 0) will define a deep valley at a flat surface (the predominance of valley structures).
- (Ssk > 0) will describe a spike above a flatter average (the predominance of peaks).

References

- [1] G. Baudana, S. Biamino, D. Ugues, M. Lombardi, P. Fino, M. Pavese, and C. Badini, "Titanium aluminides for aerospace and automotive applications processed by electron beam melting: contribution of Politecnico di Torino," *Metal Powder Rep.*, vol. 71, pp. 193-199, 2016.
- [2] M. Weglowski, S. Blacha, and A. Phillips, "Electron beam welding-techniques and trends-review," *Vacuum*, vol. 130, pp. 72-92, 2016.
- [3] J. P. Choi, G. H. Shin, H. S. Lee, D. Y. Yang, S. Yang, C. W. Lee, M. Brochu, and J. H. Yu, "Evaluation of powder layer density for the selective laser melting (SLM) process," *Mater. Trans.*, vol. 58, pp. 294-297, 2017.
- [4] J. Clayton, J. Dawes, and C. Langley, "Optimizing metal powders for additive manufacturing: exploring the impact of particle morphology and powder flowability," *additivemanufacturing.media*, May 26, 2017. [Online]. Available: http://www.additivemanufacturing.media/blog/post/optimizing-metal-powders-for-additive-manufacturing-exploring-the-impact-of-particle-morphology-and-powder-flowability. [Accessed Dec. 20, 2018].
- [5] A. Klassen, T. Scharowsky, and C. Korner, "Evaporation model for beam based additive manufacturing using free surface lattice Boltzmann methods," *J. Phys. D: Appl. Phys.*, vol. 47, pp. 1-12, 2014.
- [6] D. Schulze, *Powders and Bulk Solids: Behavior, Characterization, Storage and Flow.* Berlin, Germany: Springer-Verlag Berlin Heidelberg, 2008.
- [7] W. Yan, Y. Qian, W. Ma, B. Zhou, Y. Shen, and F. Lin, "Modeling and experimental validation of the electron beam selective melting process," *Engineering*, vol. 3, pp. 701-707, 2017.
- [8] M. K. Stanford and C. DellaCorte, "Effects of humidity on the flow characteristics of a composite plasma spray powder," *J. Therm. Spray. Tech.*, vol. 15, pp. 33-36, 2006.
- [9] B. Alchikh-Sulaiman, P. R. Carriere, and S. Yue, "A novel method for generating a single layer of powder and calculating the packing factor with the assistance of white-light interferometry, for electron beam powder bed fusion (EB-PBF)," in *New Waves of Thermal Spray Technology for Sustainable Growth: Proceedings of the International Thermal Spray Conference, ITSC 2019, Yokohama, Japan, May 26-29, 2019*, Y. Lau, J. Veilleux, C. Widener, F. Toma, H. Koivuluoto, K. Balani, H. Li, K. Shinoda, Eds., Yokohama, ASM International, pp. 893-900.
- [10] S. Berretta, O. Ghita, and K. Evans, "Morphology of polymeric powders in laser sintering (LS): from polyamide to new peek powders," *European Polymer J.*, vol. 59, pp. 218-229, 2014.

- [11] S. Ziegelmeier, P. Christou, F. Wollecke, C. Tuck, R. Goodridge, R. Hague, E. Krampe, and E. Wintermantel, "An experimental study into the effects of bulk and flow behavior of laser sintering polymer powders on resulting part properties," *J. Mater. Proc. Tech.*, vol. 215, pp. 239-250, 2015.
- [12] L. Loewgren and M. Wildheim, "Method for improved powder layer quality in additive manufacturing", U.S. Patent 2016/0129501 A1, May 12, 2016.
- [13] E. Parteli and T. Pöschel, "Particle-based simulation of powder application in additive manufacturing," *Powder Tech.*, vol. 288, pp. 96-102, 2016.
- [14] Z. Xiang, M. Yin, Z. Deng, X. Mei, and G. Yin, "Simulation of forming process of powder bed for additive manufacturing," *J. Manuf. Sci. Eng.*, vol. 138, pp. 081002, 2016.
- [15] R. German, *Powder Metallurgy Science*. Princeton, NJ: Metal Powder Industries Federation, 1984.
- [16] A. B. Spierings, M. Voegtlin, T. Bauer, and K. Wegener, "Powder flowability characterization methodology for powder-bed-based metal additive manufacturing," *Prog. Addit. Manuf.*, vol. 1, pp. 9-20, 2016.
- [17] F. Amado, M. Schmid, G. Levy, and K. Wegener, "Advances in SLS powder characterization,": *Proceedings of the Annual International Solid Freeform Fabrication Symposium, Austin, TX, USA, August 8-10, 2011,* D.L. Bourell, R.H. Crawford, C.C. Seepersad, J.J. Beaman, H. Marcus, Ed. Austin: The University of Texas at Austin, 2011. pp. 3-5.
- [18] B. Liu, R. Wildman, C. Tuck, I. Ashcroft, and R. Hague, "Investigation the effect of particle size distribution on processing parameters optimization in selective laser melting process," : *Proceedings of the Annual International Solid Freeform Fabrication Symposium, Austin, TX, USA, August 8-10, 2011*, D.L. Bourell, R.H. Crawford, C.C. Seepersad, J.J. Beaman, H. Marcus, Ed. Austin: The University of Texas at Austin, 2011. pp. 227-238.
- [19] J. Whiting and J. Fox, "Characterization of feedstock in the powder bed fusion process: sources of variation in particle size distribution and the factors that influence them,": *Proceedings of the 26th Annual International Solid Freeform Fabrication Symposium, Austin, TX, USA, August 8-10, 2016,* D.L. Bourell, R.H. Crawford, S. Fish, J.J. Beaman, H. Marcus, Ed. Austin: The University of Texas at Austin, 2016. pp. 1-12.
- [20] A. B. Spierings, N. Herres and G. Levy, "Influence of the Particle Size Distribution on Surface Quality and Mechanical Properties in Additive Manufactured Stainless Steel Parts,": *Proceedings of the 21st Annual International Solid Freeform Fabrication Symposium, Austin, TX, USA, August 29-31, 2010*, D.L. Bourell, R.H. Crawford, C.C. Seepersad, J.J. Beaman, H. Marcus, Ed. Austin: The University of Texas at Austin, 2010. pp. 1-10.

- [21] C. Körner, "Additive manufacturing of metallic components by selective electron beam melting, a review," *Inter. Mater. Rev.*, vol. 61, pp. 361-377, 2016.
- [22] C. McCracken, C. Motchenbacher, and R. Deeter, "Plasma Spheroidized Titanium Powders," *cdn.ymaws.com*, Oct. 7, 2012. [Online]. Available: https://cdn.ymaws.com/titanium.org/resource/resmgr/2010_2014_papers/McCrackenColin_2012.pdf. [Accessed April. 17, 2017].
- [23] A. Santomaso, P. Lazzaro, and P. Canu, "Powder flowability and density ratios: the impact of granules packing," *Chem. Eng. Sci.*, vol. 58, pp. 2857-2874, 2003.
- [24] A. Bodhmage, "Correlation between physical properties and flowability indicators for fine powders," Ph.D. dissertation, Dept. Chem. Eng., University of Saskatchewan, Saskatoon, SK, 2006.
- [25] T. Hao, "Understanding empirical powder flowability criteria scaled by Hausner ratio or Carr index with the analogous viscosity concept," *RSC Advances*, vol. 5, pp. 57212-57215, 2015.
- [26] R. Freeman, "Measuring the flow properties of consolidated, conditioned and aerated powders-a comparative study using a powder rheometer and a rotational shear cell," *Powder Tech.*, vol. 174, no. 1, pp. 25-33, 2007.
- [27] C. Hare, U. Zafar, M. Ghadiri, T. Freeman, J. Clayton, and M. J. Murtagh, "Analysis of the dynamics of the FT4 powder rheometer," *Powder Tech.*, vol. 285, pp. 123-127, 2015.
- [28] J. Clayton and R. Deffley, "Optimizing metal powders for additive manufacturing," *Metal Powder Rep.*, vol. 69, pp. 14-17, 2014.
- [29] P. Li, "Effect of powder flow properties on the process performance of loss-in-weight feeders," M. S. thesis, Dept. Chem. Eng., University of New Jersey, New Brunswick, NJ, 2015.
- [30] M. Li, "Study of the FT4 powder rheometer: comparison of the test methods and optimization of the protocols," Ph.D. dissertation, Dept. Proc. Eng., Université de Technologie de Compiègne, Compiègne, France, 2017.
- [31] AZO materials and Freeman Technology, "Additive manufacturing using powder rheometry to improve print quality," 9 December 2016. [Online]. Available: https://www.azom.com/article.aspx?ArticleID=13391. [Accessed: Oct. 11, 2018].
- [32] B. Alchikh-Sulaiman, M. Alian, F. Ein-Mozaffari, A. Lohi, and S. R. Upreti, "Using the discrete element method to assess the mixing of polydisperse solid particles in a rotary drum," *Particuology*, vol. 25, pp. 133-142, 2016.

- [33] J. A. Slotwinski, E. J. Garboczi, P. E. Stutzman, C. F. Ferraris, S. S. Watson, and M. A. Peltz, "Characterization of metal powders used for additive manufacturing," *Journal of Research of the National Institute of Standards and Technology*, vol. 119, pp. 460-493, 2014.
- [34] S. Haeri, Y. Wang, O. Ghita, and J. Sun, "Discrete element simulation and experimental study of powder spreading process in additive manufacturing," *Powder Tech.*, vol. 306, pp. 45-54, 2016.
- [35] P. R. Carriere, "Energy and charge transfer during electron beam melting," Ph.D. dissertation, Dept. Mater. Eng., McGill Univ., Montreal, QC, 2018.
- [36] M. Van den Eynde, L. Verbelen, and P. Van Puyvelde, "Assessing polymer powder flow for the application of laser sintering," *Powder Tech.*, vol. 286, pp. 151-155, 2015.
- [37] P. M. Ireland, "Dynamic particle-surface tribocharging: the role of shape and contact mode," *J. Electrostatics*, vol. 70, no. 6, pp. 524-531, 2012.
- [38] S. Adi, H. Adi, H. Chan, P. Young, D. Traini, R. Yang, and A. Yu, "Scanning white-light interferometry as a novel technique to quantify the surface roughness of micron-sized particles for inhalation," *Langmuir*, vol. 24, pp. 11307-11312, 2008.
- [39] Y. Lu, J. Park, L. Yu, and S.W. Kim, "3D Profiling of rough SiC surfaces by coherence scanning interferometry using femtosecond laser," *OSA Optical Society*, vol. 57, no. 10, pp. 2584-2589, 2018.
- [40] M. Sedlacek, P. Gregorcic, and B. Podgornik, "Use of the roughness parameters *Ssk* and *Sku* to control friction- a method for designing surface texturing," *Tribology Transactions*, vol. 60, no. 2, pp. 260-266, 2017.
- [41] C. Gomez, R. Su, A. Thompson, J. DiSciacca, S. Lawes, and R. Leach, "Optimization of surface measurement for metal additive manufacturing using coherence scanning interferometry," *Optical Engineering*, vol. 56, no. 11, pp. 111714 (1-8), 2017.
- [42] W. Nan, M. Pasha, T. Bonakdar, A. Lopez, U. Zafar, S. Nadimi, and M. Ghadiri, "Jamming during particle spreading in additive manufacturing," *Powder Tech.*, vol. 338, pp. 253-262, 2018.
- [43] A. Diaz, "Surface texture characterization and optimization of metal additive manufacturing-produced components for aerospace applications," *Add. Manuf. Aero. ind.*, pp. 341-374, 2019.
- [44] F. Blateyron, "The areal field parameters," in *Characterisation of Areal Surface Texture*, R. Leach, Eds. London: Springer-Verlag Berlin Heidelberg, 2013, pp. 15-43.

- [45] K. C. Mills, *Recommended Values of Thermophysical Properties for Selected Commercial Alloys*. Cambridge, UK: Woodhead Publishing, 2002.
- [46] E. S. Gadelmawla, M. M. Koura, T. M. Maksoud, I. M. Elewa, and H. H. Soliman, "Roughness parameters," *J. Mater. Proce. Tech.*, vol. 123, pp. 133-145, 2002.
- [47] K. A. Alshibli and M. I. Alsaleh, "Characterizing surface roughness and shape of sands using digital microscopy," *J. Comp. Civ. Eng.*, vol. 18, pp. 36-45, 2004.

Chapter 5: Powder Spreading and Tribocharging for Additive Manufacturing Process

Basel Alchikh-Sulaiman, Paul R. Carriere, Xin Chu, Yang Liu, Stephen Yue.

In chapter 4, with the assistance of the white-light interferometry WLI (coherence scanning interferometry), three surface topography parameters (R_a , Skewness and S_{dq}) were applied to compare between the substrates before powder spreading, and several contact-sintering experiments were obtained. In addition, a stylus profiler was used to validate a surface roughness (R_a) measurement obtained with WLI. Also, the powder rheometer was utilized to investigate the relations between powder properties and flow. In this chapter, to further the validation process of the previous chapter, the height profile for powder-bed and cross-section of powder-layer obtained with the WLI is validated with a digital light-optical microscope. As well, the method of contact-sintering is expanded for a single layer of powder sample using an electric furnace at atmospheric pressure. Finally, tribocharging is detected for the first time by a powder rheometer.

Abstract

Despite the wide applications of powder metallurgy in the field of additive manufacturing (AM), knowledge on the mechanism of contact-sintering for the single layer (SL) of powder in electron beam powder bed fusion (EB-PBF) is limited. Recently, the definition of contact-sintering was introduced as a method to evaluate the spreading for SL of powder for EB-PBF [1]. For this paper, the effect of layer thickness over the packing factor is investigated. In addition, the definition of contact-sintering is expanded towards SL of powder samples inside the electrical furnace at atmospheric pressure. The cross-section of powder-layer and the height profile for powder-bed obtained with the white-light interferometry are validated with a digital light-optical microscope. Finally, a factor which affects the spreading, i.e. tribocharging, is indirectly detected for AM powders by an FT4-powder rheometer.

5.1 Introduction

Additive manufacturing (AM) begins with a three-dimensional (3D) computer-aided design (CAD) of the part. Using this file, in powder bed fusion (PBF), the machine lays down successive layers of powder to produce the required 3D part [2]. Additive manufacturing processes are sorted according to the source of materials, joining mechanism, and energy. The source of applied energy is either a high-energy laser (selective laser melting SLM) or an electron beam; materials are metals, polymers or ceramics in the form of powder or wire [2]. The electron beam powder bed fusion (EB-PBF) is dominated by the Arcam system from Sweden [2, 3].

A group of metals and alloys have been investigated by EB-PBF for different applications: (i) titanium for medical applications, (ii) Ti-6Al-4V alloy for aerospace industry, (iii) Inconel 718 alloy for gas turbines and aero engines for frames and discs [4] and (iv) the stainless steel (SS) 316L alloy for biomedical applications [5]. For SLM and EB-PBF, the recommended powder sizes are between 15 - 45 μm and 45 - 106 μm, respectively [6, 7]. For this paper, both particle size distributions (PSD) are used.

The deployment of powder inside an electron beam powder bed fusion (EB-PBF) chamber is based on the following steps [8]: (i) storage of powder inside two hoppers under vacuum; the build plane moves downwards a definite height (typically 50 to 100 µm) to allow for a layer of powder to be added to the workpiece; (ii) flow of powder particles under its own weight from the storage hopper

to the build plane; this step is related to the powder flowability [9]. The flow of powder particles is affected by the following factors [9,10]: interparticle friction, geometrical interlocking, adhesion due to liquid or solid bridging, and charging (Electrostatic and Tribocharging); (iii) spreading; once the powder particles fall from the hopper and accumulate, a rake spreads the powder to fill the space uniformly (a single layer of powder bed); this requires the powders to be spreadable [11].

The main objective is to generate layers with dense, homogenous packing characteristics, as this accelerates the overall building rate (cm³/hour) and creates a reproducible process; however, the physics behind the formation of this thin layer has not been thoroughly investigated [12, 13].

Powder flow and spreading used to be considered as similar processes. However, there are differences between flow and spreading, these differences have not been fully examined. For the first layer, the main differences between spreadability and flowability processes are concerned with build plane (substrate) surface characteristics: (i) topography, and (ii) temperature [14, 15]. However, the surface characteristics (roughness and temperature) of the previous layer will affect spreadability of the next layer. For all layers, the other main difference between spreadability and flowability is that the stresses experienced by the powder particles are caused by raking the particles at a constant velocity [13].

To evaluate the effectiveness of powder spreading, the packing factor (\emptyset) is presented. A parameter for powder bed was defined by Van den Eynde et al. [16]. The packing factor (\emptyset) is the ratio of single layer density to solid density, and it is an index for the packing quality of a single powder layer in PBF; the higher packing factor will lead to a denser sintered part [17].

The maximum packing factor (\emptyset_{max}) is defined as the ratio of tap density (ρ_{tap}) to solid density for the same material, and (\emptyset_{max}) is limited by the size distribution and morphology of powder particles [16]. Alchikh-Sulaiman et al. [1] presented a novel approach to measuring packing factor of a single layer of powder (SL) whereby the as-spread powder was stabilized by a contact-sintering (CS) heating schedule performed in a customized electron beam welding unit.

$$\left(\emptyset = \frac{\rho_{(single-layer-powder)}}{\rho_{(solid)}}\right) \le \left(\emptyset_{max} = \frac{\rho_{(tap)}}{\rho_{(solid)}}\right) \quad (5.1)$$

Contact-sintering (CS) is a process to freeze the powder particles in the as-spread condition, with minimal changes in the packing characteristics and morphology of particles. The original definition for CS is based on two sequential steps. The first step is to heat the powder using the electron beam (EB) inside a vacuum chamber from a certain temperature (e.g. 25°C) to several hundred degrees Celsius (T_{CS}) in a short period of time without a direct contact between EB and powder to avoid powder smoking [18]. In other words, the EB will hit the outer side of substrate. The second step is to maintain this CS temperature (T_{CS}) for four to six minutes only.

For other additive manufacturing powder bed fusion (AM-PBF) processes that operate at atmospheric pressure, the definition of CS is expanded towards SL of powder samples inside the electrical furnace.

As mentioned above, the tribocharging impacts on the powder flow and might affect the spreading. When two materials are rubbed against each other, their surface may exchange electrons. The material with the stronger affinity for negative charge will gain electrons and will be charged negatively after the two materials are separated. The 2nd material will have an equal amount of positive charge [19].

Whiting [20] proposed that charging could be responsible for variations observed in the basic flow energy (BFE) results obtained with the FT4 powder rheometer (Freeman Technology, Tewkesbury, UK). The amount of charge developed depends on the following factors [21]: (i) nature of the materials in contact, (ii) ambient conditions, (iii) pressure of the contact, (iv) relative velocity of the contact surfaces and (v) friction between the contact surfaces.

For this paper, a technique is described to investigate the tribocharging effect in which the contacts between interacted particles [22] are generated by powder rheometer and the effect of charging at the flow is investigated using the value of BFE [mJ]. The tribocharging effect is expanded to cover the following components at the FT4 powder rheometer: the material of vessel (borosilicate glass and stainless steel), and the powder particles.

This research paper will address the results of contact-sintering inside vacuum chamber and electrical furnace, and the effect of tribocharging is correlated with powder spreading.

5.2 Experimental Methods

5.2.1 White-light interferometry (WLI)

Noncontact optical profilometry (ZygoTM NewView 8000, CT, USA) using white-light interferometry (WLI) proposes a dependable, fast and appropriate technique of performing surface roughness measurements, characterizations of the contact-sintered SL of powders, and large area image stitching with 3D surface visualization. White-light interferometry was utilized to obtain different surface measurements, such as root-mean-square roughness (RMS) (μ m), and the root mean square gradient of the surface (S_{dq}) (μ m/mm) [23]. The areal ISO hybrid (S_{dq}) parameter is a measurement of the slopes that cover a surface and is applied to differentiate between surfaces with similar roughness values. For a flat surface, the value of (S_{dq}) is zero [24]. At the end of Chapter 4, **Appendix A4** provided the equations of these surface parameters.

5.2.2 Light-Optical Microscope (LOM)

The optical digital microscope (KeyenceTM VHX-6000) has a multi-lighting function that could measure a surface with high complex topographies. It is an easy tool to measure surfaces with no need to configure lighting; this optical microscope was utilized to validate the measurement of height profile with WLI.

5.2.3 Powder Rheometer and Tribocharging

The stability and variable flow rate (VFR) for the powder rheometer obtains measurements for particles in motion. Measurements of axial forces and rotational torques acting are performed and the basic flowability energy (BFE) test is defined as the resistance to motion of a specialized blade as it rotates downwards through a volume of conditioned powder through a specific pathway [17, 25].

Stability and Variable Flow Rate has been utilized to define the sensitivity and stability of a powder to flow rate and it is a series of cycles (conditioning and test). During the test cycle, the impeller penetrates the powder sample and moves upwards and downwards with a constant tip speed to determine the related flow energy. To understand the sensitivity of a powder to flow rate, different impeller tip speeds are applied. From test 1 to 8, the tip speed for the impeller is 100 mm/sec, and the tip speeds for test 9, 10 and 11 are 70 mm/sec, 40 mm/sec and 10 mm/sec, respectively.

For this research, a 'repeat' (cycle) is based on the mentioned '11 tests' at different tip speeds. The BFE is the work obtained after the 7th test and is used as an index of the flowability [26]. The proposed method for the tribocharging effect, the powder sample is left inside the vessel of rheometer, and the VFR tests are repeated until the BFE plateaus.

5.2.4 Materials

Powder Ti-6Al-4V (grade 23) and stainless steel (SS316L) powders were used with the CS experiments, where the PSD for these powders were $45 - 106 \mu m$ and $13 - 28 \mu m$, respectively. Inconel 718 powder with the PSD of $15 - 45 \mu m$ was used with the powder rheometer experiments. For the substrates, Inconel 718 and Ti-6Al-4V (grade 5) 1.53 mm thick plates, were laser cut into approximately 50 mm by 50 mm sections, by Baoji Magotan Nonferrous Metals Co. (Shaanxi, China), and were used as substrates on which the powders were spread.

5.2.5 Procedure to prepare a single layer (SL) of powder

To spread the powder over this substrate, a metal puck of stainless steel was fabricated. A high degree of flatness (\pm 9 μ m) and smoothness (low value for the surface roughness (R_a)) was obtained for this puck with a manually operated grinding machine. To spread the powder over the prepared substrate, the flat puck was manually rotated for two complete rotations, with an angular velocity about 0.5 rpm. Powder was slowly poured into a funnel over the substrate for 30 seconds. The puck was then placed gently on top of the powder for 30 seconds before the rotation.

Figure 5.1-a represents a diagram for the procedure to prepare a SL of powder for the electron-beam chamber or electrical furnace. By applying powder according to previous set-up and procedure, the powder was spread in a circular shape, **Fig. 5.1-a**. Note that the thickness of this 'single' layer is approximately two or three particles. Based on our experimental results for CS studies for different powders [1], the electrical furnace was adjusted for (T_{CS}) temperature for each powder. The SL of powder sample was prepared outside the furnace, then inserted inside the furnace for seven minutes only. However, the furnace was operated at atmospheric pressure with the existence of air.

To calculate the density for a SL of powder, the weights of substrate and sample of powder were recorded. After CS, the total weight of sample (substrate + CS powder) was measured.

Thus, the utilized mass of powder (m_{SL}) was determined, and the shape of the SL was assumed to be a thin disc, Fig. 5.1-a. Surface topography of the SL was measured by WLI, as presented in Fig. 5.1-b.

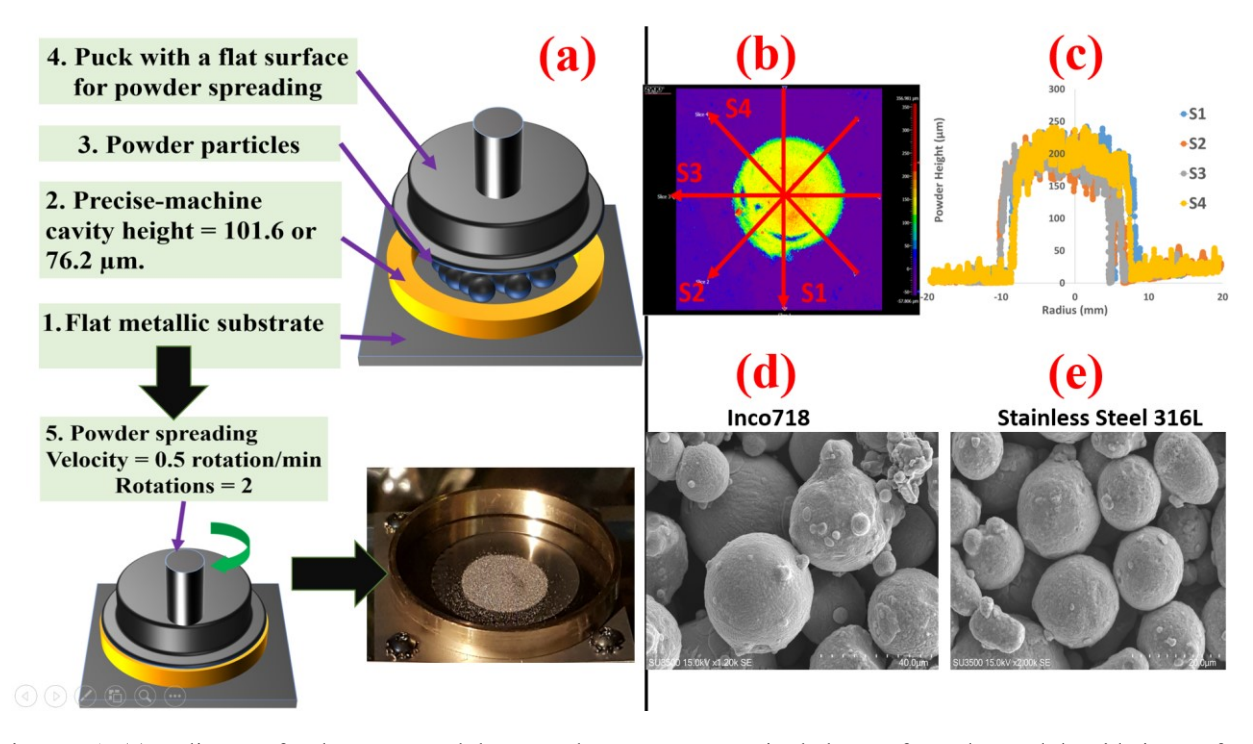


Figure 5.1: (a) A diagram for the set-up and the procedure to prepare a single layer of powder, and the side image for a SL powder sample before contact-sintering, (b) with the assistance of WLI, the measured SL of Inconel 718 powder sample with color contour of $20 \mu m/div$ and four cross-sections,(c) the extracted height profile with respect to the four cross-sections, and (d and e) SEM images for the CS samples inside electrical furnace for Inconel 718 and SS316L.

From **Fig. 5.1-c**, the height profiles for the four slices (cross-sections) lines were plotted with respect to the average diameter for the sample. As a result of **Fig. 5.1-c**, the maximum powder height (h_{max}) was determined. Also, the area $(area_{SL})$ of best fit circle to SL circumference was determined by the measured surface, **Fig. 5.1-b**. Thus, SL density $(\rho_{(single-layer-powder)})$ was calculated by **Equation (5.2)**.

$$\rho_{(single-layer-powder)} = \frac{m_{SL}}{h_{max} \times area_{SL}}$$
 (5.2)

5.3 Results and Discussion

5.3.1 The validation for height profile measurements for single layer of powder (WLI vs. LOM)

A single layer of powder was prepared with Ti-6Al-4V (PSD = $45 - 106 \mu m$); where mass of powder was 0.083 gram; the material of substrate was made of Ti-6Al-4V (grade 5). After

preparing the SL of powder as described previously in the Experimental Methods, a blade was used to slice the powder bed and the section was measured by WLI and LOM.

By comparing the results from LOM and WLI, there is a good agreement between both instruments in terms of the waviness of surface and shape of the powder-layer. It is important to mention that WLI measurement was obtained with no-form remove to follow same scanning strategy with LOM, **Fig. 5.2**. Also, the maximum heights for WLI and LOM were 190 μ m and 170 μ m, respectively.

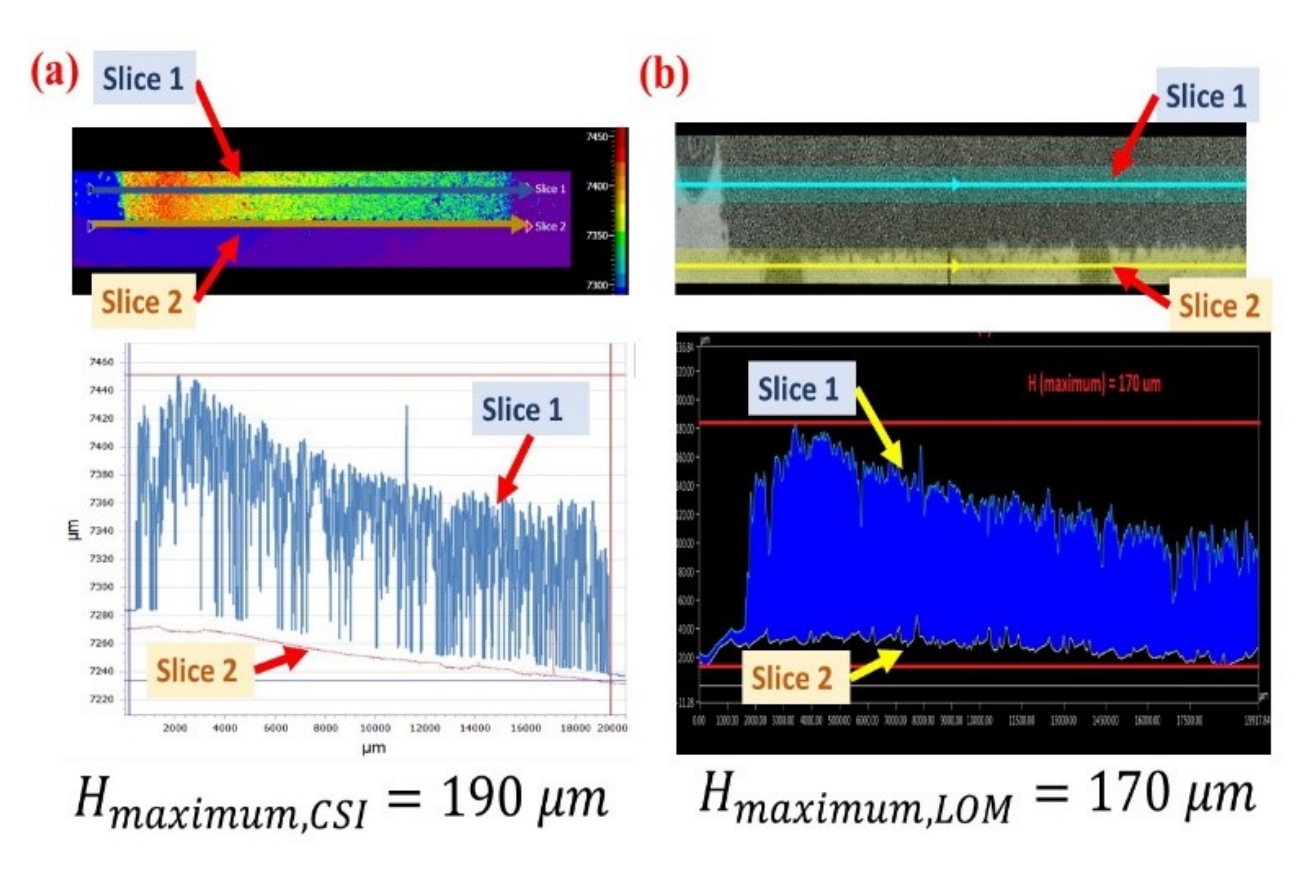


Figure 5.2: (Left) Surface measurement for a definite single layer (SL) of powder with WLI, and (Right) the surface measurement for the same sample with LOM.

5.3.2 The detection of tribocharging with powder rheometer

The powder rheometer is equipped with a borosilicate glass vessel; friction forces between powder particles and internal surface of vessel and possible tribocharging effects (exchange of electrons) can influence with BFE values. The internal surface roughness (smoothness) of the vessel edges will enhance the mentioned factors.

To distinguish the effect of the material of vessel over the BFE value and flow dynamic, a custom-made stainless steel vessel with same dimensions of the powder rheometer borosilicate glass was fabricated. The Inconel 718 powder was utilized to obtain this examination with the stainless steel vessel; the dynamic flow for this experiment was plotted with same graph on **Fig. 5.3-a** to compare the differences. According to **Fig. 5.3-a**, the stainless steel vessel has affected the flow behavior for powder particles in-compare to the borosilicate vessel. Where, there was a shift for the BFE value and for the graph of VFR test for the stainless steel vessel.

For this research paper, the stability and variable flow rate (VFR) test obtained with the stainless steel vessel might describe to some extent the powder spreading at AM process.

Powder particles are spread by rake over a substrate to generate one single layer of powder. For the VFR test, particles rotate and slide over the internal surface of the vessel as a result of the rotating impeller. To investigate the performance of Inconel 718 with many repeats, the powder was left inside the two vessels and no-splitting was obtained after the first experiment.

The stability and variable flow rate (VFR) tests were repeated for 12 times until the value of BFE plateaued, and **Fig. 5.3-b** plotted the value of BFE against the number of repeats. The absolute increments for the BFE values for stainless steel and glass vessels were 18% and 50%, respectively.

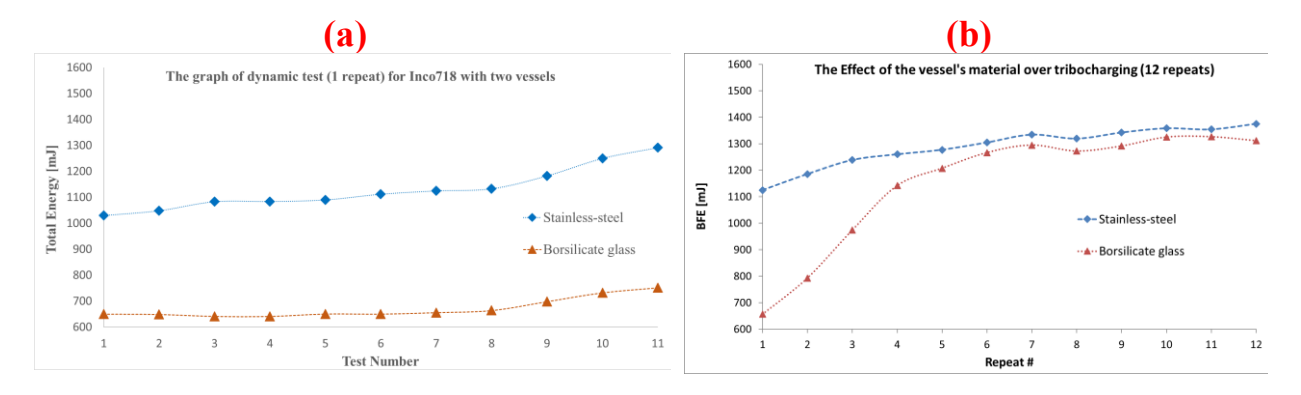


Figure 5.3: (a) The effect of the material of vessel over VFR test for Inconel 718 samples, and (b) the value of BFE for powder Inconel 718 with respect to 12 repeats.

5.3.3 Effects of the layer thickness over packing factors (CS in vacuum chamber)

To evaluate spreadability for different powder samples, the powder heights and packing factors were obtained for the following samples, where all SL of samples were spread over Inconel 718

substrates. To calculate the packing factors, the solid densities for Ti-6Al-4V, Inconel 718, and SS316L were 4.42 g/cm³, 8.19 g/cm³ and 7.95 g/cm³, respectively [27].

Based on **condition (5.1)**, the values of maximum packing factor (\emptyset_{max}) for Ti-6Al-4V, Inconel 718 and SS316L were 63.3%, 64.7% and 63.4%, respectively. Six SL of Ti-6Al-4V samples were prepared at the electron beam inside a vacuum chamber. On the other hand, two samples of SL of Inconel 718 and SS316L were contact-sintered at the electric furnace. All SL of samples were measured by WLI after CS processes.

Table 5.1 provides the operational CS parameters and values of packing factor for all SL samples. According to **Fig. 5.1-d** and **Fig. 5.1-e**, SEM images for Inconel 718 and SS316L samples showed that powder particles had maintained their morphology at the end of CS at furnace.

Based on **Table 5.1**, the packing factors of Inconel 718 (Inco718) and SS316L samples with smaller PSDs have higher packing values in compare to the Ti-6Al-4V with wider PSD. Also, the effects of two height cavities for the Ti-6Al-4V over the values of (\emptyset) were not significant, and it showed similar (\emptyset) values for samples 4 and 6.

Table 5.1: Packing factor values for all single layer of samples.

Heating method	Powder Sample	$(T_{CS}^{\ \ o}, ext{time for CS})$ PSD for powder	Height of Specific Cavity (μm)	Mass (gram)	Area (mm²)	Maximum height (µm)	SL density (g/cm³)	Packing fraction (Φ *100%)	Measured substrate after CS	
									RMS (µm)	Sdq (µm/mm)
	1			0.109	245.2	186	2.390	54.1	1.55	152
Electron beam welding machine (Vacuum chamber)	2	(T _{cs≈} 700 °C, 4-6 min) PSD= 45-106 μm	,	0.117	290.9	250	1.609	36.4	1.33	80
	3		101.6	0.136	293.8	300	1.543	34.9	10.8	340
	4		,	0.081	243.2	230	1.185	32.8	6.00	167
	5			0.098	265.4	292	1.264	28.6	6.25	203
	6		76.2	0.087	237.2	220	1.667	37.7	1.45	54
Thermal furnace (Atmospheric pressure)	Inco718	(T _{cs} = 889°C, 7 min)		0.235	209.5	232	4.834	59	8	240
		PSD =15 – 45 µm								
	SS316L	(T _{cs} = 889°C, 7 min) PSD = 13 – 28 μm	101.6	0.206	183.8	247	4.537	57.1	3.44	295

5.4 Conclusions

This paper provided a unique opportunity to investigate the expansions for the definition of contact-sintering mechanism for different metallic powders. Two processes were defined to generate single layer (SL) samples, where the electron-beam and electrical furnace were applied as the source of heating in vacuum and atmospheric pressure, respectively. Moreover, the powder-bed densities and packing factors were calculated for the following layer thicknesses (101.6 μ m and 76.2 μ m). The tribocharging effect was discussed and correlated to the powder spreading.

References

- [1] B. Alchikh-Sulaiman, P. R. Carriere, and S. Yue, "A novel method for generating a single layer of powder and calculating the packing factor with the assistance of white-light interferometry, for electron beam powder bed fusion (EB-PBF)," in *New Waves of Thermal Spray Technology for Sustainable Growth: Proceedings of the International Thermal Spray Conference, ITSC 2019, Yokohama, Japan, May 26-29, 2019*, Y. Lau, J. Veilleux, C. Widener, F. Toma, H. Koivuluoto, K. Balani, H. Li, K. Shinoda, Eds., Yokohama, ASM International, pp. 893-900.
- [2] G. Baudana, S. Biamino, D. Ugues, M. Lombardi, P. Fino, M. Pavese, and C. Badini, "Titanium aluminides for aerospace and automotive applications processed by electron beam melting: contribution of Politecnico di Torino," *Metal Powder Report*, vol. 71, pp. 193-199, 2016.
- [3] M. Weglowski, S. Blacha, and A. Phillips, "Electron beam welding-techniques and trends-review," *Vacuum*, vol. 130, pp. 72-92, 2016.
- [4] D. Deng, "Additively manufactured Inconel 718 microstructures and mechanical properties," Ph.D. dissertation, Dept. Mater. Eng., Linköping Univ., Linköping, Sweden, 2018.
- [5] B. A. AlMangour, "Additive manufacturing of high-performance 316L stainless steel nanocomposites via selective laser melting," Ph.D. dissertation, Dept. Mater. Eng., University of California, Los Angeles, CA, 2017.
- [6] J. P. Choi, G. H. Shin, H. S. Lee, D. Y. Yang, S. Yang, C. W. Lee, M. Brochu, and J. H. Yu, "Evaluation of powder layer density for the selective laser melting (SLM) process," *Mater. Trans.*, vol. 58, pp. 294-297, 2017.

- [7] J. Clayton, J. Dawes, and C. Langley, "Optimizing metal powders for additive manufacturing: exploring the impact of particle morphology and powder flowability," additivemanufacturing.media, May 26, 2017. [Online]. Available: http://www.additivemanufacturing.media/blog/post/optimizing-metal-powders-for-additive-manufacturing-exploring-the-impact-of-particle-morphology-and-powder-flowability. [Accessed Dec. 20, 2018].
- [8] A. Klassen, T. Scharowsky, and C. Korner, "Evaporation model for beam based additive manufacturing using free surface lattice Boltzmann methods," *J. Phys. D: Appl. Phys.*, vol. 47, pp. 1-12, 2014.
- [9] D. Schulze, *Powders and Bulk Solids: Behavior, Characterization, Storage and Flow.* Berlin, Germany: Springer-Verlag Berlin Heidelberg, 2008.
- [10] M. K. Stanford and C. DellaCorte, "Effects of humidity on the flow characteristics of a composite plasma spray powder," *J. Therm. Spray. Tech.*, vol. 15, pp. 33-36, 2006.
- [11] W. Yan, Y. Qian, W. Ma, B. Zhou, Y. Shen, and F. Lin, "Modeling and experimental validation of the electron beam selective melting process," *Engineering*, vol. 3, pp. 701-707, 2017.
- [12] H. P. Zhu, Z. Y. Zhou, R. Y. Yang, and A. B. Yu, "Discrete particle simulation of particulate systems: a review of major applications and findings," *Chem. Eng. Sci.*, vol. 63, pp. 5728-5770, 2008.
- [13] Z. Xiang, M. Yin, Z. Deng, X. Mei, and G. Yin, "Simulation of forming process of powder bed for additive manufacturing," *J. Manuf. Sci. Eng.*, vol. 138, pp. 081002, 2016.
- [14] L. Loewgren and M. Wildheim, "Method for improved powder layer quality in additive manufacturing", U.S. Patent 2016/0129501 A1, May 12, 2016.
- [15] E. Parteli and T. Pöschel, "Particle-based simulation of powder application in additive manufacturing," *Powder Tech.*, vol. 288, pp. 96-102, 2016.
- [16] M. Van den Eynde, L. Verbelen, and P. Van Puyvelde, "Assessing polymer powder flow for the application of laser sintering," *Powder Tech.*, vol. 286, pp. 151-155, 2015.
- [17] J. Clayton and R. Deffley, "Optimizing metal powders for additive manufacturing," *Metal Powder Report*, vol. 69, pp. 14-17, 2014.
- [18] P. R. Carriere, "Energy and charge transfer during electron beam melting," Ph.D. dissertation, Dept. Mater. Eng., McGill Univ., Montreal, QC, 2018.

- [19] B. Lee and D. Orr, "The TriboElectric Series,". *alphalabinc.com*, 2018. [Online]. Available: https://www.alphalabinc.com/triboelectric-series/. [Accessed July 14, 2019].
- [20] J. Whiting, "Repeatability of the FT4 rheometer evaluating AM powder," *Poster session presented. Additive Manufacturing with Powder Metallurgy (AMPM) conference*, Las Vegas, NV, USA, June 13-15,2017.
- [21] M. B. Neagoe, Y. E. Prawatya, T. Zeghloul, and L. Dascales, "Influence of surface roughness on the tribo-electric process for a sliding contact between polymeric plate materials," *IOP Conf. Series: Mater. Sci. Eng.*, vol. 174, no.1, pp. 1-6, 2017.
- [22] P. M. Ireland, "Dynamic particle-surface tribocharging: the role of shape and contact mode," *Journal of Electrostatics*, vol. 70, no. 6, pp. 524-531, 2012.
- [23] C. Gomez, R. Su, A. Thompson, J. DiSciacca, S. Lawes, and R. Leach, "Optimization of surface measurement for metal additive manufacturing using coherence scanning interferometry," *Optical Engineering*, vol. 56, no. 11, pp. 111714 (1-8), 2017.
- [24] A. Diaz, "Surface texture characterization and optimization of metal additive manufacturing-produced components for aerospace applications," *Add. Manuf. Aero. ind.*, pp. 341-374, 2019.
- [25] C. Hare, U. Zafar, M. Ghadiri, T. Freeman, J. Clayton, and M. J. Murtagh, "Analysis of the dynamics of the FT4 powder rheometer," *Powder Tech.*, vol. 285, pp. 123-127, 2015.
- [26] P. Li, "Effect of powder flow properties on the process performance of loss-in-weight feeders," M. S. thesis, Dept. Chem. Eng., University of New Jersey, New Brunswick, NJ, 2015.
- [27] K. C. Mills, Recommended Values of Thermophysical Properties for Selected Commercial Alloys. Cambridge, UK: Woodhead Publishing, 2002.

Chapter 6: Detection of Tribocharging Effect for Metallic Powders with a Powder Rheometer

Basel Alchikh-Sulaiman, Louis-Philippe Lefebvre and Stephen Yue

As mentioned in chapter 2, powder flowability and spreadability were affected by tribocharging. Moreover, tribocharging was indirectly detected with the powder rheometer in chapter 5. In this chapter, a procedure is developed to compare tribocharging characteristics using the powder rheometer and to assess its effect on the flow of powder.

Abstract

Metallic powders are applied in different additive manufacturing (AM) processes. The effect of powder characteristics (composition and particle size distribution (PSD)) on tribocharging has not been well documented, and there is no method available to examine the effect of charging on flowability. For a metallic powder, the powder rheometer has been utilized to detect the tribocharging effect. This research introduces a technique to evaluate tribocharging generated inside the rheometer and assess its effect on the powder flowability using the change in basic flow energy (*BFE*), i.e. the mean percentage difference in *BFE* (%*PD*) from Repeat 1 to the plateau. In addition, two methods are defined to determine the effects of powder composition and PSD. As a result of that, the positions of commercial purity titanium (CP-Ti), Ti-6Al-4V and Inconel 718 in the new triboelectric series are proposed.

6.1 Introduction

Additive manufacturing (AM) delivers numerous design and manufacturing advantages including: (i) the capability to construct complicated internal topographies and shapes, (ii) integration and optimization of functional features, (iii) a high degree of customization, (iv) reduction of post processing operations, and (v) high degree of efficiency in the usage of powders [1, 2].

Different additive manufacturing (AM) processes have been designed to apply different heat sources, such as electron beam, laser beam, or welding torch, and providing the raw material in the form of powder or wire [3]. Additive manufacturing, which can be performed with polymer, ceramic or metal powders, begins with a CAD description of the component. Using this file, the machine lays down successive layers of powder to generate the required 3D object [2]. The particles are spread onto a platform and melted by a high-energy beam (electron, plasma or laser), leading to the geometry build-up of a part [1]. Additive manufacturing with powders is classified into powder bed or direct deposition systems, where powder bed AM is considered more for industrial applications. Additive manufacturing with laser is available in several variants such as direct metal laser sintering (DMLS) and selective laser melting (SLM). On the other hand, the electron beam powder bed fusion (EB-PBF) technology usually refers to the by Arcam AB systems (GE additive company, Mölndal, Sweden) [2, 4].

A suitable selection of powder is a very important step to obtain required mechanical properties and microstructures for fabricated parts [5]. The following properties of powders will affect the build with electron beam powder bed fusion (EB-PBF) process. (i) Particle size distribution (PSD) affects the ability to generate layers with the appropriate characteristics [6]; (ii) Shape and its variation with particle size; spherical particles are desirable for EB-PBF; the existence of irregular shapes and satellites could affect flowability and the building process [2]; (iii) Surface roughness of particles can affect properties of final object including density, hardness, tensile strength, and surface texture; and (iv) apparent and tap densities are considered as essential characterizations to ensure a good layer deposition, i.e. a high packing density with homogeneous surface texture [7]. The ability to forecast the flowability of powder is significant for powder metallurgy, ceramics and additive manufacturing [8]. The flowability is affected by density, surface chemistry, morphology, particle size distribution (PSD) and environmental conditions [9].

Powder flowability is controlled by the following interparticle forces: (i) adhesive forces: solid and liquid bridges (surface tension), (ii) friction forces: particle-particle interactions due to surface condition and topography, and (iii) coulombic forces: van der Waals forces, electrostatic and tribocharging [9,10]. Powder flowability cannot be fully quantified with a single measurement technique because of the powders nature and the influence of handling on measurement results [11]. The classical approach to evaluate the flowability is to measure the discharging time for 50 grams of powder through the funnel of the Hall flowmeter (ASTM B213-13) [12]. However, powder particles cannot flow under their own weight when the forces (electrostatic, van der Waals, etc.) between individual particles exceed gravitation [9]. Recently, new approaches to evaluate the powder flow have been introduced, two of these being: (i) dynamic angle of repose [13], and (ii) stability and variable flow rate (VFR) test of the powder rheometer (FT4 Freeman Technology, Tewkesbury, UK) [14]. The powder rheometer provides more information about the powder properties than the Hall flow meter, and, of course, if a powder fails the Hall flowmeter test, the rheometer gives flow properties.

As mentioned above, the tribocharging impacts on the flowability of powder. When two different materials are rubbed against each other, their surfaces may exchange electrons. The material with the stronger affinity for negative charge will gain electrons and will be charged negatively after the two materials are separated. The second material will have an equal positive charge [15].

Tribocharging is proportional to the surface contact area, and the accumulation of specific charge might be increased for particles with smaller sizes. The following surface factors will control the magnitude and polarity of tribocharging: (i) friction between the contact surfaces, (ii) shape, (iii) surface roughness, (iv) the surface chemistry and microstructure, (v) contact force, (vi) coefficient of restitution, (vii) relative velocity of the contact surfaces, (viii) pressure of the contact and (ix) ambient conditions [16, 17].

Freeman and March [18] reported the triboelectric series of different materials. When two of the listed materials in the series are rubbed together, the upper material in the series gains a negative charge and the lower one becomes positive [18]. Based on this series [18], the following materials are listed in order from the most electro-negative to the most electro-positive material: Teflon, gold (Au), nickel (Ni), steel and iron (Fe), aluminum (Al), borosilicate glass (fire polished) and asbestos.

However, according to the standard specification for additive manufacturing using nickel alloy with powder bed fusion (ASTM F3055-14a) [19], Inconel 718 is consisted of 50 wt% nickel and 17 wt% chromium. In this paper, the tribocharging behaviors for commercial purity titanium (CP-Ti), Ti-6Al-4V and Inconel 718 are investigated, which, to the best of our knowledge, have not been studied in the literature.

The work of Kwetkus and Sattler might be relevant [20], since they obtained tribocharging experiments for oxidized Ni and Cr powders under high vacuum conditions. The oxidized metal powder samples were contacted with a gold plate, with the transfer of charge being detected on the gold plate and samples. The charge was acquired by nickel powder after repeated contacts with the gold plate. At the first contact, nickel powder lost electrons (became positively charged), and did not change with further contacts. Obviously, the gold plate gained electrons (became negatively charged). This supports the triboelectric series [18], which indicates that when nickel and gold are rubbed together, gold (the upper material in the series) gains a negative charge and nickel (the lower material in the series) became positive. In the case of chromium powder [20], the first contact, the chromium also reached a "saturation charge", but became negatively charged with respect to the gold. These observations make it difficult to predict possible tribocharging effects Inconel 718, since it contains nickel and a significant level of chromium oxide.

It was mentioned above that the tribocharging is controlled by the surface chemistry. Thus, the tribocharging for commercial purity titanium and Ti-6Al-4V is controlled by the oxide layer. In the case of titanium and its alloys, TiO_2 is a transition metal oxide and it is frequently nonstoichiometric. The oxygen vacancies is the predominant defect at near-atmospheric oxygen pressure, where a deficiency in the oxygen introduces an excess of electrons in the material resulting in an increase of the electrical conductivity [21]. It is important to address that TiO_2 is an electrical insulator with a high resistivity over the $10^8 \Omega$. cm [22]. However, the oxygen vacancies act as electron donors, therefore, the sub-oxidized TiO_{2x} with an excess of titanium is an N-type semiconductor with unique properties [21, 22].

Bally [21] mentioned that the sub-stoichiometric TiO_{2x} can act as a moderate semiconductor or a poor insulator. To decrease or increase the electrical conductivity inside TiO_2 , experiments were obtained to introduce doping (a charge carrier), or to control the oxygen vacancy concentration.

Depends on the ratio between the oxygen vacancy concentration, and the concentration of iron, chromium, or manganese, these metals are described as electron acceptors decreasing or increasing the electrical conductivity of TiO₂. In addition, these incorporations manipulate the morphology and structure of TiO₂ [21].

The concept of equilibrium is important to estimate the maximum electrostatic charge carried by 'interacted particles' [23] and vessel in the rheometer. It can also evaluate electrostatic energy reserved in the system [24]. For this research, a technique is presented to explore tribocharging of the aforementioned powders generated inside the rheometer vessel. The effect of tribocharging on the flowability of powder is investigated using the value of basic flow energy (*BFE*).

6.2 Materials and Methods

6.2.1 Rheometer

All tests were conducted with the FT4 powder rheometer (Freeman Technology, Tewkesbury, UK) [25, 26]. The stability and variable flow rate (VFR) for the rheometer was utilized to define the sensitivity and stability of a powder and consisted of conditioning and test cycles. The flow is conducted by measuring the resistance of powder when moving the rotating stainless steel impeller (23.5 mm diameter) through the powder contained in a glass vessel (borosilicate glass, fire polished, 51 mm height, 25 mm internal diameter; thus, the distance between the vessel and tip of

impeller surface is 0.75 mm). At the top of the vessel, a split mechanism was attached to determine the height of the powder column, **Fig. 6.1-a**. The impeller movement from top to bottom defines one 'test'; axial forces and rotational torques acting on the impeller are measured, **Fig. 6.1-a** [25], and the total flow energy (E_{flow}) is calculated, **Fig. 6.1-b** [27]. This energy is defined as the resistance to motion of the impeller as it rotates downwards through a volume of conditioned powder through a definite pathway. The E_{flow} was introduced by Hare et al. [26]:

$$E_{flow} = \int_{H_1}^{H_2} \left(\frac{T}{R \tan \alpha} + F_{base} \right) . dH$$
 (6.1)

Where T and F_{base} are the torque and vertical force applied on the impeller, R is impeller radius, α is the is the helix angle, and $(H_2 - H_1)$ is the penetration depth inside the powder column. The values of the following parameters $(R, \alpha, H_2 \text{ and } H_1)$ are defined in the FT4 instructions.

The conventional FT4 powder rheometer measurement is generated using a series of 11 'tests', collectively designated as a 'Repeat', where from test 1 to 8, the tip speed is 100 mm/sec, and the tip speeds for test 9, 10 and 11 are 70 mm/sec, 40 mm/sec and 10 mm/sec, respectively. This Repeat is known as the variable flow rate (VFR) Repeat. Different impeller tip speeds are applied during the VFR Repeat. The basic flow energy (*BFE*) is the work calculated after the (Test 7) and is used as an index for the flowability [27].

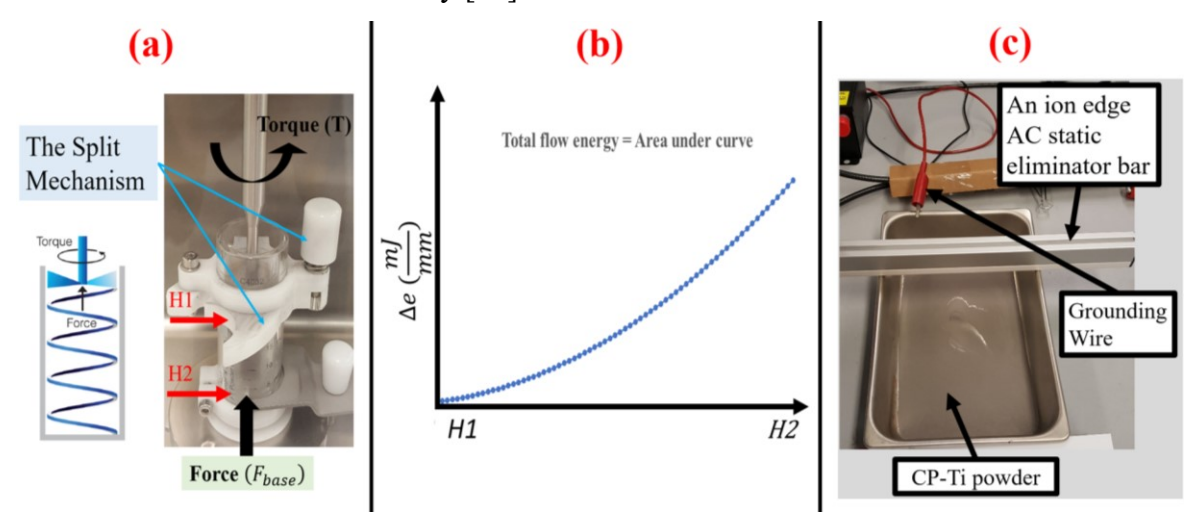


Figure 6.1: (a) Image for the FT4 powder rheometer during the VFR Repeat with the split mechanism, (b) the graph for the calculation of total flow energy, and (c) CP-Ti powder neutralized with the AC ionizing bar.

Recently, Alchikh-Sulaiman et al. [28] showed that the VFR test has a high level of consistency. For one repeat, the BFE values for three 'fresh' (i.e. not previously subjected to a Hall flowmeter

test or any powder test) powder samples (Ti-6Al-4V; PSD = $15 - 45 \mu m$) from the same bottle in one day were varied by 5.6 %.

6.2.2 Instruments for Detecting Charging

To validate tribocharging effects in the powder rheometer, the ultra-stable surface DC voltmeter (AlphaLab Inc, USA) was used to measure the powder charge. The powder was poured out of the rheometer vessel onto a grounding stainless steel tray and the voltage was measured. The powder was then subjected to neutralizing using an ion edge AC static eliminator bar (TAKK industries Inc., USA), by sweeping the AC ionizing bar above the powder on the tray 6 times as shown in **Fig. 6.1-c**. The voltage of the neutralized powder was then measured.

6.2.3 Materials

Different powders were investigated in this study, where **Figure 6.2** provides the SEM images for some of the powders. Plasma atomized commercial purity titanium (CP-Ti) and Ti-6Al-4V powders from a commercial producer with different particle size distributions (CP-Ti :0 - 45 μ m and 63 - 90 μ m) and (Ti-6Al-4V: 15 - 63 μ m and 45-106 μ m) were investigated.

Gas atomized nickel-based alloy Inconel 718 (15 - 45 μ m) and Ti-6Al-4V (15 - 45 μ m) powders from (Carpenter Powder Products Inc, USA) were applied for this work. In addition, gas atomized stainless steel (SS316L) powder from (Sandvik Osprey, Sweden) with 32 - 66 μ m PSD, aluminum H-15 (11- 43 μ m PSD) powder from (Valimet Inc., Stockton, CA), and aluminum alloy A357 (45 - 53 μ m PSD) powder from (Equispheres, Canada) were tested. Finally, glass microspheres (10 - 95 μ m PSD) from (Cospheric LLC, Santa Barbara, CA) were investigated in order to reveal the effect of tribocharging in a system with similar powder and rheometer vessel materials.

The borosilicate glass has 80% SiO₂, and the composition of glass microspheres has 72% SiO₂ [29,30]. Moreover, the chemical compositions for some of these powders are presented in **Appendices A6 and A7**. Also, the particle size distribution measurement was made with a laser particle size analyzer (Horiba LA-920, Japan). Where, each measurement was repeated four times and the average value was used.

As mentioned previously, tribocharging is affected by the ambient conditions such as relative humidity and temperature [31]. To eliminate the effect of ambient conditions, experiments were obtained in a control laboratory under following conditions (23°C room temperature and 12% average Relative Humidity). For powders, fresh samples were poured directly from closed bottles without a delay in the vessel of the rheometer.

6.2.4 Procedure for Tribocharging Experiments

Tribocharging can take place between the powder/ vessel, powder/ powder particles and powder/ impeller. In this work, the powder and vessel (borosilicate glass, fire polished) interaction is the focus. To investigate the tribocharging effects between the powder and vessel, the following two methods were used:

6.2.4.1 Method (1)

In this procedure, the following steps were proposed: (i) the tests were performed as sets of Repeats (i.e. 11 tests); (ii) between successive Repeats, the vessel was emptied of the powder by storing the tested powder in an aluminum cup; (iii) the empty vessel of the rheometer was wiped and cleaned between the Repeats; (iv) the mass of powder was recorded before and after transferring into the vessel, where a small reduction of mass was observed, and (v) the next Repeat was performed. The steps were performed until the value of basic flow energy ($BFE_{Repeat\ final}$) plateaued. In addition, CP-Ti (0 - 45 µm) and Ti-6Al-4V (15 - 63 µm) powders from a commercial producer were used for these tests.

6.2.4.2 Method (2)

No emptying or cleaning of the vessel was performed throughout this experiment. The basic flow energy (BFE) was calculated after each Repeat, and, as for Method 1, the Repeats were performed until the value of basic flow energy ($BFE_{Repeat\ final}$) plateaued.

For this method, the gas atomized Inconel 718 (15 - 45 μ m) (Nickel-based superalloy [32]) and Ti-6Al-4V (15 - 45 μ m) powders from (Carpenter Powders), SS316L, A357, aluminum H-15, the glass microspheres, and finally the plasma atomized CP-Ti (0 - 45 μ m and 63 - 90 μ m) and Ti-6Al-4V (45 - 106 μ m) powders from a commercial producer were investigated.

For both methods, the mean percentage difference (%PD) was applied to compare the change in the BFE values between Repeat 1 ($BFE_{Repeat\ 1}$) to ($BFE_{Repeat\ final}$) as defined by Cloe [33]:

$$\%PD = 100 \times \frac{BFE_{Repeat\ final\ -\ BFE_{Repeat\ 1}}}{\left(\frac{BFE_{Repeat\ final\ +\ BFE_{Repeat\ 1}}}{2}\right)}$$
(6.2)

For method 2, experiments were repeated several times for some powders, and revealed a high level of repeatability.

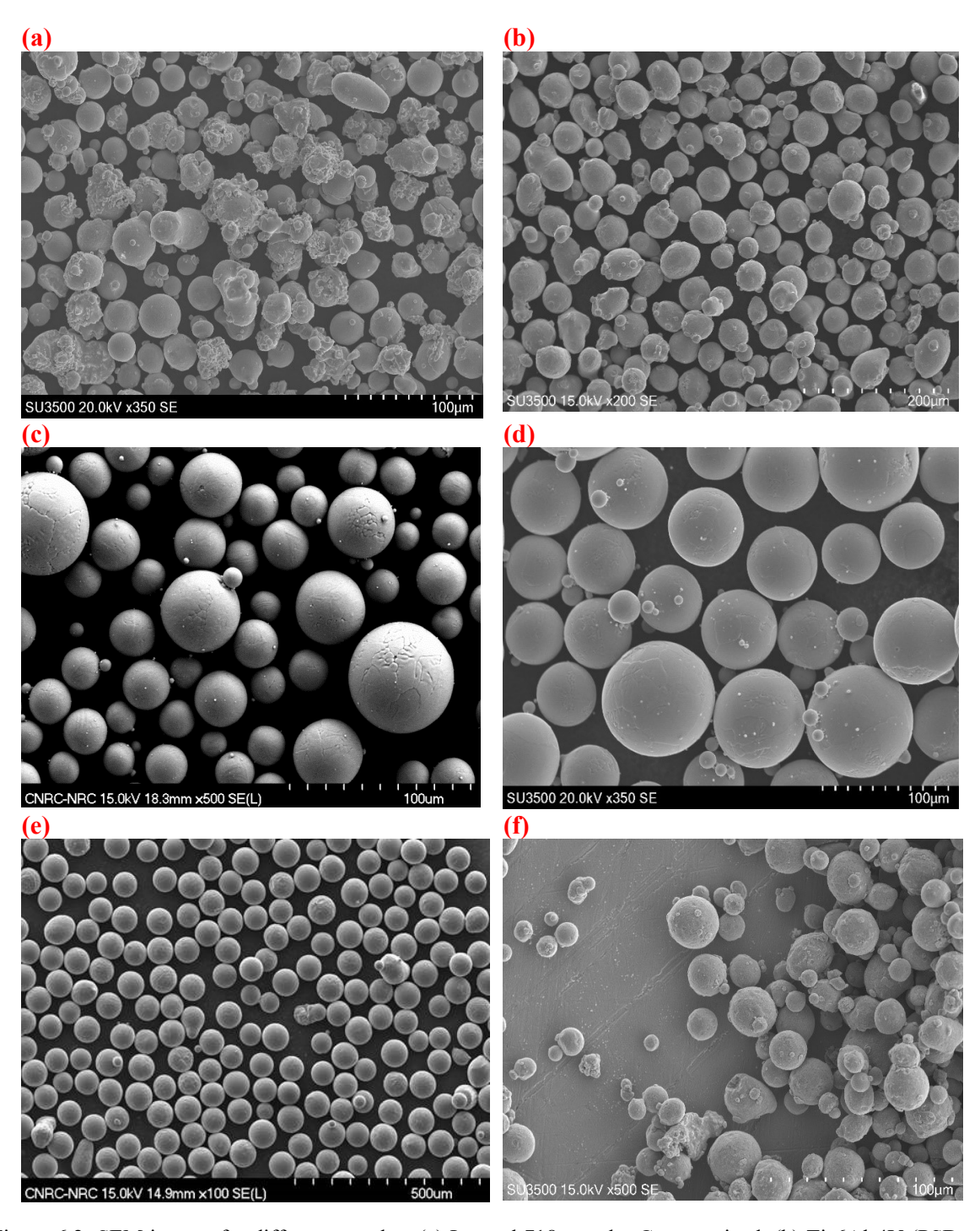


Figure 6.2: SEM images for different powders (a) Inconel 718 powder Gas atomized, (b) Ti-6Al-4V (PSD =15 - 45 μm) gas atomized, (c) Ti-6Al-4V (grade 23) with PSD = 15-45 μm plasma atomized, (d) CP-Ti with PSD=63-90 μm plasma atomized, (e) aluminum alloy A357 PSD=45- PSD=45-53 μm , and (f) gas atomized stainless-steel PSD=32 - 66 μm .

6.3 Results and Discussion

6.3.1 Method (1)

The goal of this experiment was to capture the possible variations of (BFE) value as a function of the number of repeats and the effect of cleaning the vessel during the testing.

As mentioned earlier, a mass reduction was detected for both experiments. Where, the total decrease in Ti-6Al-4V and CP-Ti masses were 2.8% and 4.8%, respectively.

For both powders, the values of (*BFE*) decreased very slightly before reaching a plateau after the fifth Repeat as shown in **Fig. 6.3**. For Ti-6Al-4V, the BFE value decreased from 281 mJ to 253 mJ, and BFE value decreased from 279 mJ to 234 mJ for CP-Ti. The (%*PD*) values for Ti-6Al-4V and CP-Ti were -10% and -18%, respectively.

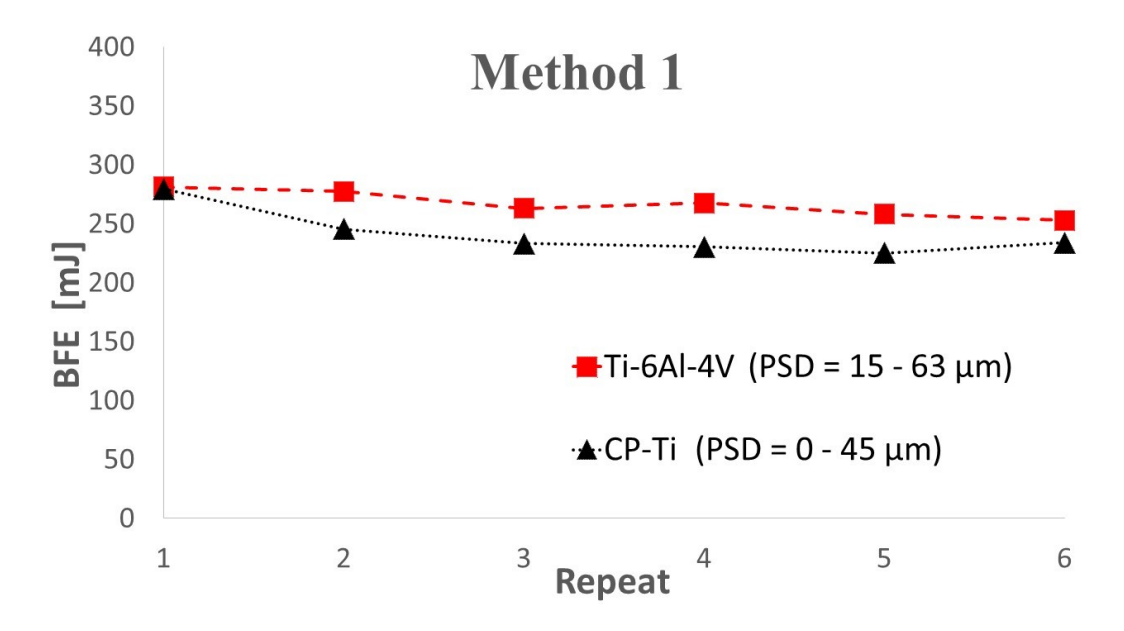


Figure 6.3: Values of BFE for two powders plotted with respect to the number of repeats

To demonstrate that charging is taking place, the aforementioned charge detection method was deployed in the following case. The CP-Ti was poured out of the rheometer vessel onto a grounding stainless tray and ionized after Repeat 6, i.e. well into the plateau region, **Fig. 6.1-c**.

The voltmeter was used to measure the static charge voltage of the powder in the stainless steel tray before and after the ionization. The measurements before and after ionization were -85 volt

and +2.7 volt, respectively. However, after ionization, the powder particles were neutralized (an electrostatic equilibrium period) as indicated by the +2.7 volt measurement.

Then, the 'neutralized' CP-Ti powder was poured back in the rheometer, and the VFR Repeat was performed to generate Repeat 7. From **Figure 6.4**, the energy values of each test of Repeat 7 are higher compared to the corresponding values of Repeat 6. (For both Repeats in **Fig. 6.4**, the energy values for Test 9 (70 mm/sec), Test 10 (40 mm/sec) and Test 11(10 mm/sec) are higher compared to energy values for Tests 1 to 8; because the rotating impeller requires more energy when moving through the powder with a lower tip speed.)

If the powder was not neutralized, the $(BFE_{Repeat 7})$ should be equal to $(BFE_{Repeat 6})$, i.e. well into the plateau region, **Fig. 6.3**. The CP-Ti particles will continue to gain a negative charge, and the vessel surface (borosilicate glass, fire polished) will have an equal positive charge until an electrostatic equilibrium occurs between them [24].

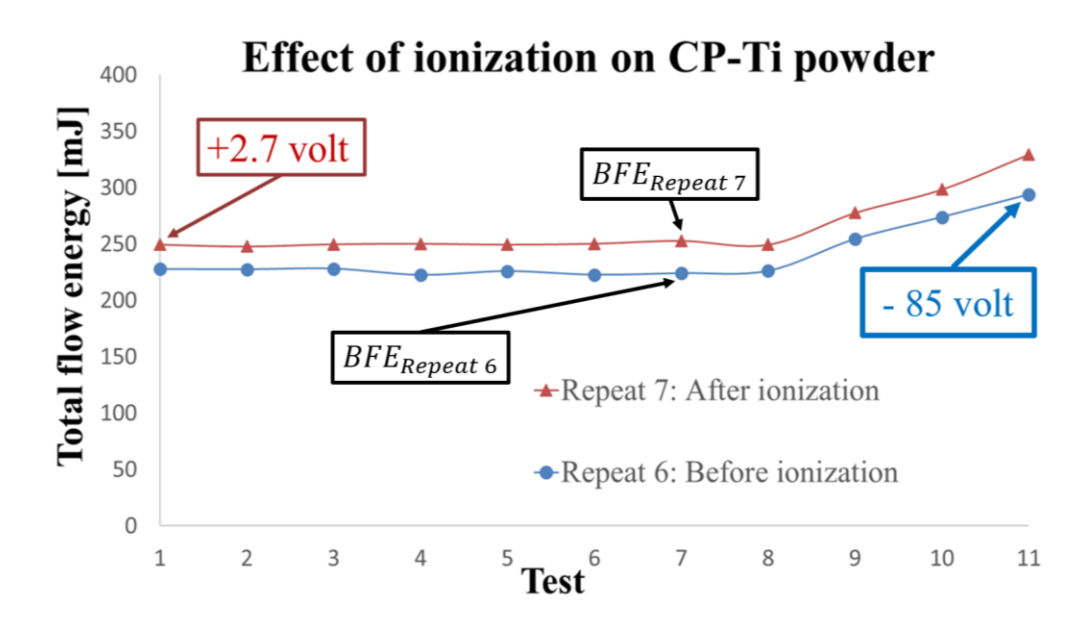


Figure 6.4: The VFR Repeat performed before and after ionization.

6.3.2 Method (2)

To examine the charging effects for powders on the basic flow energy (BFE) and (%PD) values, the VFR Repeats were performed with fresh samples of powders. The evolution of VFR Repeat reveals two periods: (i) the transition period: a region of rapid rise in the energy, and (ii) the plateau or electrostatic equilibrium. The exceptions to this behavior are the Ti-6Al-4V (45- 106 μ m), A357 and the glass microspheres, which do not really change in their (BFE) and (%PD) values.

The $(BFE_{Repeat\ 1})$ and (%PD) values for Inconel 718 and SS316L powders are much higher compared to the other powders, therefore the results are provided into two figures. **Figure 6.5** presents the (BFE) values for Inconel 718 and SS316L with respect to the number of repeats, and **Figure 6.6** provides the (BFE) values for the other powders.

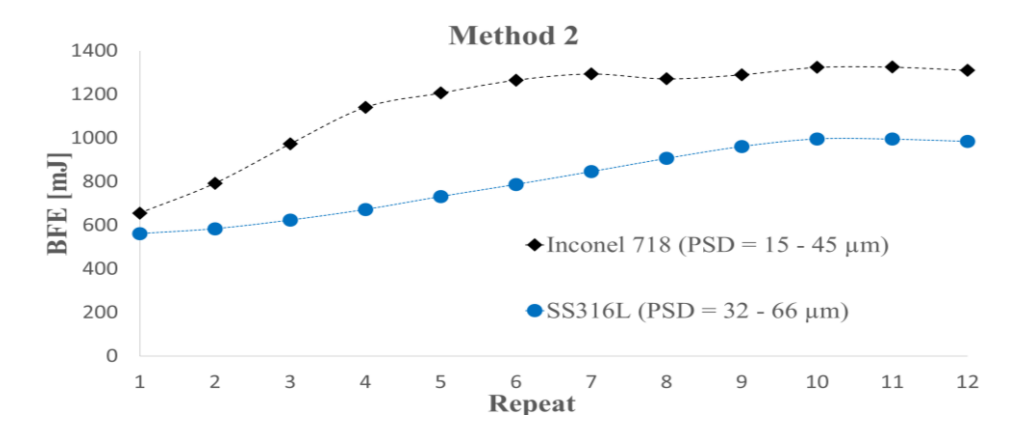


Figure 6.5: BFE values for Inconel 718 and SS316L powders plotted with respect to the number of repeats.

From **Figure 6.5**, the value of $(BFE_{Repeat\ 1})$ for Inconel 718 was higher than for SS316L. Also, the transition period exhibits a lower rate of increase for SS316L compared to the Inconel 718. Finally, the values of (%PD) for Inconel 718 and SS316L were 67% and 55%, respectively. From **Figure 6.6**, the powders are listed in terms of the decreasing $(BFE_{Repeat\ final})$ values in the plateau period: Ti-6Al-4V (15 - 45 μ m), CP-Ti (0 - 45 μ m), CP-Ti (63 - 90 μ m), Ti-6Al-4V (45-106 μ m), aluminum H-15, A357, and the glass microspheres. More importantly, with regard to tribocharging characteristics, the related (%PD) values were 10%, 23%, 25%, 3%, 48%, 2% and 2%, respectively.

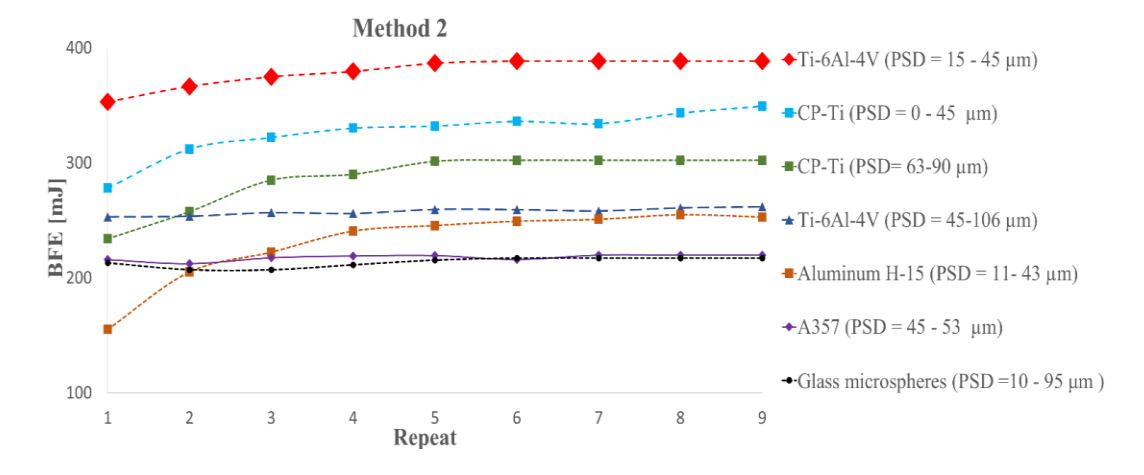


Figure 6.6: BFE values for Ti-6Al-4V, CP-Ti, aluminum H-15, A357 and glass microspheres powders plotted with respect to the number of repeats.

As suggested above, **Figures 6.5** and **6.6** indicate that the VFR Repeat is undergoing the tribocharging; this charging is caused mainly by the interactions between the powder and vessel, and the powder and powder (same-material bipolar charging). These measurements agreed with Whiting [34], who proposed that charging could be responsible for variations observed in the (*BFE*) results obtained for a stainless steel powder with the powder rheometer for many repeats. During the interaction between metallic particles with an insulator (borosilicate glass), the transfer of charges can be explained by a similar hypothesis of the metal and metal electron transfer with the assumption of an "effective work function" is assigned to the insulator [31]. For the powder and powder same-material bipolar charging, larger particles tend to lose electrons (become positively charged) on coming in contact with smaller particles, which gain electrons (become negatively charged) [35, 36].

The specific influence of each of these powders on the tribocharging needs further work. But it is interesting to note that, in the case of aluminum and titanium, the (%PD) is much higher for the commercial 'pure' metal than the alloy. This obviously needs further investigation, but one approach to explaining the tribocharging behavior is to consider the surface chemistry of particles. Therefore, the tribocharging for CP-Ti and Ti-6Al-4V is controlled by the oxide layer, where TiO₂ is an electrical insulator with a high resistivity. However, Bally [21] mentioned that the substoichiometric TiO_{2x} can act as a moderate semiconductor or a poor insulator. If aluminum atoms for Ti-6Al-4V are incorporated into TiO₂, a decrease in the electrical conductivity is observed. On the other hand, the electrical conductivity of TiO₂ is increased if vanadium atoms are incorporated [21]. Such considerations for the role of oxide layer in the tribocharging is probably valid for the other powders.

From the above results, the new triboelectric series is presented in **Table 6.1**, where Inconel 718 is the furthest material from the glass microspheres, and A357 is the closest to the glass microspheres. The SS316L is closer to glass microspheres than Inconel 718 but further away from A357.

Thus, there is generally good agreement between **Table 6.1** and the previously mentioned triboelectric series [18] (i.e. the materials are listed in order from the most electro-negative to the most electro-positive: nickel, steel, aluminum, and borosilicate glass). It is interesting to note that the Ti-6Al-4V seems to exhibit a size effect whereas CP-Ti does not.

Moreover, as mentioned above, it is notable from **Table 6.1**, that the tribocharging behavior for commercial pure metals is much higher compared to their alloys. Clearly, the influence of particle size distribution and alloying additions needs much more investigation.

Table 6.1: Positions of Inconel 718, SS316L, Ti-6Al-4V and CP-Ti in the new triboelectric series based on %PD values.

More Negative (-)	% PD
Inconel 718	67%
SS316L	55%
Aluminum H-15	48%
CP-Ti (63 - 90 μm)	25%
CP-Ti (0 - 45 μm)	23%
Ti-6Al-4V (15 - 45 μm)	10%
Ti-6Al-4V (45- 106 μm)	3%
A357	2%
Glass microspheres	2%
More Positive (+)	

The values of (%PD) for CP-Ti (0 - 45 μ m and 63 - 90 μ m) and Ti-6Al-4V (15 - 45 μ m and 45-106 μ m) were located between the (%PD) values for the aluminum H-15 and A357. Thus, CP-Ti and Ti-6Al-4V should be positioned between the aluminum H-15 and A357 in the new triboelectric series.

6.4 Conclusion

Powder rheometer was utilized to detect tribocharging effects for different AM metallic powders. A novel technique was defined to evaluate tribocharging generated inside the rheometer and assessed its effect on the powder flowability using the change in basic flow energy (BFE), i.e. the mean percentage difference in BFE (%PD) from Repeat 1 to the plateau. In the case of aluminum and titanium, the mean percentage difference (%PD) was much higher for the commercial 'pure' metal than the alloy. In terms of particle size effects, CP-Ti exhibited no variation whereas Ti-6Al-4V showed a significant effect. Finally, the positions of Inconel 718, Ti-6Al-4V and commercial purity titanium and A357 in the new triboelectric series were proposed, based on the (%PD) values.

Appendix (A6)

The composition of borosilicate glass is 80% SiO₂, 14% B₂O₃, 4% Na₂O, and 2% Al₂O₃ [29], and the composition of glass microspheres is 72% SiO₂, 14% Na₂O, 8% CaO, and 6% MgO [30].

Gas atomized titanium alloy Ti-6Al-4V (15 - 45 μ m) powder from (Carpenter Powder Products Inc, USA) was used in **Chapter 6**. According to the powder certificate, the chemical compositions of this powder are listed in **Table A6.1**

Table A6.1: The constituents of Ti-6Al-4V powder based on Carpenter powder certificate.

Element	Weight Percentage %			
Titanium	Balance			
Aluminum	6.32			
Vanadium	3.99			
Iron	0.20			
Oxygen	0.12			
Nitrogen	0.0206			
Carbon	0.0106			
Hydrogen	0.0024			
Yttrium	< 0.001			

The commercial purity titanium (CP-Ti) powder was used. According to the powder certificate, the chemical compositions of this powder are listed in **Table A6.2**

Table A6.2: The constituents of CP-Ti powder based its material certificate.

Element	Weight Percentage %
Titanium	Balance
Iron	0.04
Oxygen	0.12
Nitrogen	0.01
Carbon	0.01
Hydrogen	0.002
Other	0.3

The commercial purity aluminum H-15 powder was used. According to the powder certificate from Valiment Inc., the chemical composition is 99.8% Al and 0.12 % Fe.

References

- [1] Y. Sun, S. Gulizia, C. Oh, C. Doblin, Y. Yang, and M. Qian, "Manipulation and characterization of a novel titanium powder precursor for additive manufacturing applications," *The Min. Met. Mater. Soc.*, vol. 67, pp. 564-572, 2015.
- [2] G. Baudana, S. Biamino, D. Ugues, M. Lombardi, P. Fino, M. Pavese, and C. Badini, "Titanium aluminides for aerospace and automotive applications processed by electron beam melting: contribution of Politecnico di Torino," *Met. Powder Rep.*, vol. 71, pp. 193-199, 2016.
- [3] B. Baufeld, "Mechanical properties of Inconel 718 parts manufactured by shaped metal deposition (SMD)," *J. Mater. Eng. Perfo.*, vol. 21, pp. 1416-1421, 2012.
- [4] M. Weglowski, S. Blacha, and A. Phillips, "Electron beam welding-techniques and trends-review," *Vacuum*, vol. 130, pp. 72-92, 2016.
- [5] J. P. Choi, G. H. Shin, H. S. Lee, D. Y. Yang, S. Yang, C. W. Lee, M. Brochu, and J. H. Yu, "Evaluation of powder layer density for the selective laser melting (SLM) process," *Mater. Trans.*, vol. 58, pp. 294-297, 2017.
- [6] C. Körner, "Additive manufacturing of metallic components by selective electron beam melting, a review," *International Materials Reviews*, vol. 61, pp. 361-377, 2016.
- [7] A. B. Spierings, M. Voegtlin, T. Bauer, and K. Wegener, "Powder flowability characterization methodology for powder-bed-based metal additive manufacturing," *Prog. Addit. Manuf.*, vol. 1, pp. 9-20, 2016.
- [8] B. Alchikh-sulaiman, F. Ein-Mozaffari, and A. Lohi, "Evaluation of poly-disperse solid particles mixing in a slant cone mixer using discrete element method," *Chem. Eng. Res. Des.*, vol. 96, pp. 196-213, 2015.
- [9] M. K. Stanford and C. DellaCorte, "Effects of humidity on the flow characteristics of a composite plasma spray powder," *J. Therm. Spray. Tech.*, vol. 15, pp. 33-36, 2006.
- [10] D. Schulze, *Powders and Bulk Solids: Behavior, Characterization, Storage and Flow.* Berlin, Germany: Springer-Verlag Berlin Heidelberg, 2008.
- [11] A. Santomaso, P. Lazzaro, and P. Canu, "Powder flowability and density ratios: the impact of granules packing," *Chem. Eng. Sci.*, vol. 58, pp. 2857-2874, 2003.
- [12] ASTM International, "ASTM B213-13: standard test methods for flow rate of metal powders using the Hall flowmeter funnel," *in Annual book of ASTM standards 2013 (pp. 27-30)*. West Conshohocken, PA: American Society for Testing and Materials, 2013.

- [13] F. Amado, M. Schmid, G. Levy, and K. Wegener, "Advances in SLS powder characterization,": *Proceedings of the Annual International Solid Freeform Fabrication Symposium, Austin, TX, USA, August 8-10, 2011,* D.L. Bourell, R.H. Crawford, C.C. Seepersad, J.J. Beaman, H. Marcus, Ed. Austin: The University of Texas at Austin, 2011. pp. 3-5.
- [14] R. Freeman, "Measuring the flow properties of consolidated, conditioned and aerated powders-a comparative study using a powder rheometer and a rotational shear cell," *Powder Tech.*, vol. 174, no. 1, pp. 25-33, 2007.
- [15] B. Lee and D. Orr, "The TriboElectric Series,". *alphalabinc.com*, 2018. [Online]. Available: https://www.alphalabinc.com/triboelectric-series/. [Accessed July 14, 2019].
- [16] M. B. Neagoe, Y. E. Prawatya, T. Zeghloul, and L. Dascales, "Influence of surface roughness on the tribo-electric process for a sliding contact between polymeric plate materials," *IOP Conf. Series: Mater. Sci. Eng.*, vol. 174, pp. 1-6, 2017.
- [17] R. Mukherjee, V. Gupta, S. Naik, S. Sarkar, V. Sharma, P. Peri, and B. Chaudhuri, "Effects of particle size on the triboelectrification phenomenon in pharmaceutical excipients: experiments and multi-scale modelling," *Asian J. Pharm. Sci.*, vol. 11, pp. 603-617, 2016.
- [18] G. Freeman and N. March, "Triboelectricity and some associated phenomena," *Mater. Sci. Tech.*, vol. 15, pp. 1454-1458, 1999.
- [19] ASTM International, "Standard specification for additive manufacturing nickel alloy (UNS N07718) with powder bed fusion," *in Annual book of ASTM standards 2014 (pp.1-8)*. West Conshohocken, PA: American Society for Testing and Materials, 2014.
- [20] B. A. Kwetkus and K. Sattler, "Contact charging of oxidized metal powders," *Z. Phys. B Condensed Matter*, vol. 82, pp. 87-93, 1991.
- [21] A. Bally, "Electronic properties of nano-crystalline titanium dioxide thin films," Ph.D. dissertation, Dept. Phys., École Polytechnique Fédérale De Lausanne, Lausanne, EPFL, 1999.
- [22] Y. Ju, M. Wang, Y. Wang, S. Wang and C. Fu, "Electrical properties of amorphous titanium oxide thin films for bolometric application," *Adv. Cond. Matter Phys.*, vol. 365475, pp. 1-5, 2013.
- [23] P. M. Ireland, "Dynamic particle-surface tribocharging: the role of shape and contact mode," *J. Electro.*, vol. 70, pp. 524-531, 2012.
- [24] J. Yao, Y. Zhang, C.H. Wang, and Y.C. Liang, "On the electrostatic equilibrium of granular flow in pneumatic conveying systems," *J. AIChE*, vol. 52, pp. 3775-3793, 2006.

- [25] J. Clayton and R. Deffley, "Optimizing metal powders for additive manufacturing," *Metal Powder Report*, vol. 69, pp. 14-17, 2014.
- [26] C. Hare, U. Zafar, M. Ghadiri, T. Freeman, J. Clayton, and M. J. Murtagh, "Analysis of the dynamics of the FT4 powder rheometer," *Powder Tech.*, vol. 285, pp. 123-127, 2015.
- [27] P. Li, "Effect of powder flow properties on the process performance of loss-in-weight feeders," M. S. thesis, Dept. Chem. Eng., University of New Jersey, New Brunswick, NJ, 2015.
- [28] B. Alchikh-Sulaiman, P. R. Carriere, and S. Yue, "For Powder Bed Additive Manufacturing Process: Correlations between Single Layer Density and Powder Properties with the Assistance of Coherence Scanning Interferometry," *PowderMet 2019: International Conference on Powder Metallurgy & Particulate Materials*, D. Reardon and V. Warke Ed., June 23-26, 2019 (Phoenix, AZ, USA), Metal Powder Industries Federation, pp. 285-304.
- [29] V. Venkatesh and S. Mahadevan, "Electro-chemical mechanical polishing of copper and chemical mechanical polishing of glass," *J. Mater. Process. Technol.*, vol.149, pp. 493-498, 2004.
- [30] P. K. Mallick, "Particulate and short fiber reinforced polymer composites," in *Comprehensive Composite Materials*, vol. 2, Reference Work, A.Kelly, C. Zweben, Eds. Cambridge University, UK: Elsevier, 2000, pp. 291-331.
- [31] S. Matsusaka, H. Maruyama, T. Matsuyama, and M. Ghadiri, "Triboelectric charging of powders: A review," *Chem. Eng. Sci.*, vol. 65, pp. 5781-5807, 2010.
- [32] T. M. Pollock and S. Tin, "Nickel-based superalloys for advanced turbine engines: chemistry, microstructure, and properties," *J. Prop. Power.*, vol. 22, pp. 361-374, 2006.
- [33] T. J. Cole, "Sympercents: symmetric percentage differences on the 100 loge scale simplify the presentation of log transformed data," Statist. Med., vol. 19, pp. 3109-3125, 2000.
- [34] J. Whiting, "Repeatability of the FT4 rheometer evaluating AM powder," *Poster session presented. Additive Manufacturing with Powder Metallurgy (AMPM) conference, Las Vegas, USA, June 13-15, 2017.*
- [35] R. Mukherjee, V. Gupta, S. Naik, S. Sarkar, V. Sharma, P. Peri, and B. Chaudhuri, "Effects of particle size on the triboelectrification phenomenon in pharmaceutical excipients: experiments and multi-scale modelling," *Asian J. Pharm. Sci.*, vol. 11, pp. 603-617, 2016.
- [36] S. R. Waitukaitis, V. Lee, J. M. Pierson, S. L. Forman, and H. M. Jaeger, "Size-dependent same-material tribocharging in insulating grains," *Ameri. Phys. Soc.*, vol. 112, pp. 218001(1-5), 2014.

Chapter 7: The Effect of Tribocharging and Same-material Bipolar Charging on Powder Flowability with the Assistance of Powder Rheometer

Basel Alchikh-Sulaiman and Stephen Yue

In chapter 6, a technique was presented to study tribocharging generated inside the powder rheometer using the basic flow energy (BFE). The effects of powder composition and particle size distribution on tribocharging were investigated. Also, the tribocharging behaviour for Inconel 718 was reported. In this chapter, tribocharging evaluation continues by examining the effects of the rheometer vessel material (borosilicate glass and stainless steel), using Inconel 718 and stainless steel 316L powders.

Abstract

There is a lack of sufficient knowledge regarding the effect of tribocharging and same-material bipolar charging on flowability of Inconel 718 and stainless steel 316L powders for the additive manufacturing (AM) powder bed fusion process. Recently, Alchikh-Sulaiman et al. [1] developed a technique to generate and study tribocharging inside a powder rheometer and assessed the effect of tribocharging on various parameters. In this research, the continuous flow rate (CFR) which presents a modification of the methodology in [1], is extended to determine the charging effects of the rheometer vessel material (borosilicate glass and stainless steel). The contribution of tribocharging to the total flow energy (e_f) , and therefore flowability, can then be determined. The evolution of CFR test in the borosilicate glass vessel reveals three periods: (i) the incubation period, (ii) the transition period, and finally (iii) the electrostatic equilibrium. Once the vessel is changed to stainless steel, the incubation period has disappeared, and the other two periods will occur.

7.1 Introduction

Additive manufacturing (AM), or 3D printing, has the capability to produce parts based on the customer personal choice, where it does not require tooling. As a result of that, AM process has reduced the unit cost by allowing direct manufacture from a computer design, and the fabrication can take place in or close to the operation location [2]. The fact that AM has the ability to fabricate a unique part at no extra cost with the design freedom, this provides the ability to produce one or few parts and it is economically possible [3].

Additive manufacturing technologies are classified according to source of energy, materials and joining mechanism, where the materials are in the form of wires or powders [4]. Additive manufacturing, which can be performed with polymer, ceramic and metals powders, begins with a computer-aided design (CAD) description of the component. Using this file, the machine lays down successive layers of powder in a layer-upon-layer fashion to generate the required 3D part [4]. The particles are spread onto a platform and melted by a high-energy beam (electron, plasma or laser), leading to the geometry build-up of a part [5]. The additive manufacturing (AM) with electron beam powder bed fusion (EB-PBF) is only delivered by Arcam AB (technology: electron beam melting EBM, GE additive company, Mölndal, Sweden) [6]. The AM with laser is available in several variants such as selective laser melting (SLM) [7].

Knowledge of powder characteristics is essential to obtain the required mechanical properties and microstructures of fabricated parts [8]. For EB-PBF and SLM, the recommended powder sizes are between 45 - 106 μm and 15 - 45 μm, respectively [8, 9].

In fact, powder bed fusion and other AM technologies are operated with fixed process parameters for specified powder feedstock characteristics and a definite 3D object. However, even feedstocks that appear to have the 'same' characteristics can lead to inconsistent quality of the finished part [9]. Therefore, a better understanding relation between powder characteristics and final-part properties is essential; this paper will concentrate on powder flow.

Selective laser melting has successfully processed a variety of materials for different applications such as steel, stainless steel (SS316L), tool steel (H13), titanium alloys (Ti-Al6-V4 and Ti-Al6-Nb7), AlSi12Mg, cobalt chromium, nickel-based alloys and bronze-based alloys [6,10].

Inconel 718 is a nickel based superalloy that is applied widely in the nuclear applications and aerospace industry where corrosion and creep resistances at high temperature are essential design parameters [11]. The stainless steel (SS316L) alloy has been fabricated with SLM for biomedical applications [10].

7.1.1 Flowability

The ability to quantify the powder flowability is vital for different powder industries [12 - 14]; where, the flowability depends on the physical properties of a powder, environmental conditions and the equipment used for measuring the flow. The shape of powder particles, size distribution, surface chemistry and chemical composition are some of the physical properties that could affect the flow of powder. In addition, the temperature of powder, relative humidity and moisture content are among the environmental conditions [15,16].

Due to the influence of handling on flow results, there is not a single instrument or test which is appropriate to examine the flowability for different powders [15,17,18]. However, the initial step is usually the Hall flowmeter, which has a high sensitivity for the surface smoothness of powder particles [19].

In the Hall flowmeter, 50 grams of powder is allowed to fall through a funnel (ASTM B213-13) [20]. Lately, the stability and variable flow rate (VFR) test of the powder rheometer (Freeman

Technology, Tewkesbury, UK) [12], and the dynamic angle of repose for GranuDrum (Granutools, Awans, Belgium) are also being utilized to measure the powder flowability. The powder rheometer provides more information about the powder properties than the Hall flow meter, and, of course, if a powder fails the Hall flowmeter test (i.e. does not fall through the funnel), the rheometer gives flow properties.

Flowability is essentially a function of the forces between individual particles. These forces are classified as: (i) interparticle friction, (ii) geometrical interlocking, (iii) adhesive forces: solid and liquid bridges (surface tension), and (iv) coulombic forces: van der Waals forces, electrostatic and tribocharging [13, 21]. In this paper, the coulombic force behavior generated by tribocharging is studied.

7.1.2 Physics of Tribocharging

Tribocharging of particles is a phenomenon occurring during powder handling, and the electrostatic forces or accumulated charges developed could affect the process significantly. Powder charging involves environmental conditions. For example, Greason [22] measured the charge on a metal sphere with a Faraday cage after contact with an insulating material under various conditions. The charge increased with decreasing relative humidity at a definite temperature. When the relative humidity was low, the charge decreased with increasing temperature [22]. It was mentioned by Nomura et al. [23], that the charge of a wet powder was lower than that of the dry powder, and the absolute value of tribocharging for a powder increased with decreasing humidity.

Charging is, of course, also affected by the electrical and physical properties of a powder and container vessel. The powder becomes electrostatically charged both by interparticle collisions or segregation, and collisions against other materials including the vessel and container. In fact, in the pharmaceutical industry, the flowability of fine size powder becomes difficult to control due to the tribocharging effect of particles [24]. Because of these multiple influences, it is a difficult task to evaluate the tribocharging characteristics of a powder during the process [23].

Tribocharging is proportional to the surface contact area, and the accumulation of specific charge might be increased for particles with smaller sizes. The following surface factors can control the magnitude and polarity of tribocharging; (i) friction between the contact surfaces, (ii) shape, (iii)

surface roughness, (iv) the type of the materials, (v) contact force, (vi) coefficient of restitution, (vii) relative velocity of the contact surfaces, (viii) pressure of the contact and (ix) ambient conditions [25, 26].

7.1.2.1 Different-material Tribocharging

When two different materials are rubbed against each other, their surfaces may exchange electrons. The material with the stronger affinity for negative charge will gain electrons and will be charged negatively after the two materials are separated. The second material will have an equal positive charge [27]. Freeman and March [28] revealed the triboelectric series of different materials; when two of the listed materials in the series are rubbed together, the upper material in the series gains a negative charge and the lower one becomes positive. Based on the triboelectric series [28], the following materials are listed in order from the most electro-negative to the most electro-positive material: Teflon, gold (Au), nickel (Ni), steel and iron (Fe), aluminum (Al), borosilicate glass (fire polished) and asbestos.

Alchikh-Sulaiman et al. [1] have recently been utilized the powder rheometer to detect tribocharging for a metallic powder. A new technique was introduced to examine tribocharging generated inside the powder rheometer and evaluated its effect on the values of basic flow energy. From Chapter 6, two methods determined the effects of powder composition, particle size distribution (PSD) and handling. As a result of this research, a new triboelectric series was provided, where, the materials were listed in order from the most electro-negative towards the most electro-positive material: Inconel 718, stainless-steel 316L, commercial purity titanium and Ti-6Al-4V, aluminum alloy A357, and borosilicate glass fire polished.

7.1.2.2 Same-material Bipolar Charging

For particles of the same material, bipolar charging exists between particles with different size fractions. Where larger particles have a tendency to lose electrons (become positively charged) on coming in contact with smaller particles, which gain electrons (become negatively charged) [26, 29, 30]. Forward et al. [31] developed a correlation for powders between the binary particle size and charge polarity.

7.1.2.2.1 Same-material Charging and Segregation

Powders in the presence of shear forces will self-organize into local regions of particles with similar density, particle size, shape and/or surface characteristics [32, 33]. This is clearly a problem in additive manufacturing powder bed fusion (AM-PBF) because different layers may have different packing factors, for example.

Recent studies specified that the main reason for segregation of powder particles is the particle size difference [14, 34, 35]. Four segregation mechanisms based on the particle size distribution were proposed by Tang and Puri [36]: (i) side-to-side (large particles), (ii) sieving (small particles), (iii) agglomeration (cohesive fine) and (iv) fluidization (fine). Forward et al. [31] observed charge segregation for a bimodal system, where this segregation relied on the proportion of the particle sizes. In other words, the segregation was discussed as a result of same-material bipolar charging phenomenon. The tribocharging effect on the homogeneity of powder blending was examined by Pu et al. [37] for binary mixtures. It was found that the minimization, or the elimination if it is possible, of the electrostatic charges can disturb the homogeneity of the mixture.

For a process, the segregation of metallic powder particles due to particle size should take in account the bipolar charging, where smaller particles will become negatively charged and larger particles will become positively charged.

During the stability and variable flow rate (VFR) test, segregation occurred when smaller particles moved and stored on the back surface of the impeller due to the downward and upward cycles. Inside the powder rheometer, the larger particles stayed at the upper section of the powder column. On the other hand, smaller particles occupied the lower section of the column and filled the upper side of the impeller [38]. Based on this analysis, the segregation mechanism during the VFR test was determined to be sieving.

7.1.3 Tribocharging in Hall Flowmeter

In any flowmeter, there is a relative flow between particles. Where, in the case of the Hall flowmeter, there is a relative flow between particles and the funnel. Also, in the case of the powder rheometer, there is a relative flow between powder particles with the impeller and vessel.

Finally, in the case of in the case of the dynamic angle of repose, the flow is between the powder particles and drum surface.

Clearly, tribocharging will take place and it is therefore important to take this into account when measuring flow in order to obtain consistent/reproducible flow results. Tribocharging will also occur at stages of additive manufacturing where powders are moved, so it is important to measure the evolution of the tribocharging forces, and to determine the influence of powder characteristics on tribocharging.

In addition to the above, the concept of equilibrium is also important to estimate the maximum electrostatic charge carried by particles/vessel in the powder rheometer and helps to evaluate electrostatic energy reserved in the system [39].

In this paper, the flowability in the powder rheometer is the focus; in particular the tribocharging behavior with an electrostatic equilibrium for the following two powders (Inconel 718 and stainless steel 316L) were examined.

7.2 Materials and Methods

7.2.1 Powder Characterization

Gas atomized nickel-based alloy Inconel 718 (15 - 45 µm) powder from (Carpenter Powder Products Inc, USA) was investigated in this study. The apparent density and flow rate from the product certificate were 3.71 g/cm³ and 16 sec/50 gram. From the standard specification for additive manufacturing nickel alloy with powder bed fusion (ASTM F3055-14a) [40], Inconel 718 is consisted of nickel (50 wt%) and chromium (17 wt%).

Gas atomized stainless steel (SS316L) from (Sandvik Osprey, Sweden) and glass microspheres from (Cospheric LLC, Santa Barbara, CA) powders were used for this work. The PSDs for SS316L and glass microspheres were 32 - 66 μ m and 10 - 95 μ m, respectively.

From the standard specification for stainless steel wire (ASTM A 580/A 580M - 06) [41], stainless steel (SS316L) is consisted of iron (balance), chromium (16 wt%), nickel (10 wt%) and molybdenum (2 wt%). However, the chemical compositions for Inconel 718 and stainless steel (SS316L) powders are presented in **Appendix A7**.

During this work, the evaluation of particle flowability was carried out by measuring the Hall flow rate (s/50 g) as per ASTM B213-13 [20], which is expressed as the time required for 50 grams of powder to be discharged by its weight through the funnel. In addition, the morphology of the examining powder was observed with a scanning electron microscope (SEM, Hitachi SU-3500 Variable Pressure, Japan). The particle size distribution measurement was made with a laser particle size analyzer (Horiba LA-920, Japan). Where, each measurement was repeated four times and the average value was reported.

Figure 7.1 shows the morphology of the four studied powders. For Inconel 718, the powder samples consisted mainly of spherical particles but with a few elongated ones and some surface irregularities. The particle size values of D_{10} , D_{50} and D_{90} (in µm) were 20, 31 and 55, respectively. Similar observations were made for the gas atomized stainless steel (SS316L), but the level of surface irregularities and elongated particles appeared to be lower; the particle sizes of D_{10} , D_{50} and D_{90} (in µm) were 32, 47 and 66, respectively.

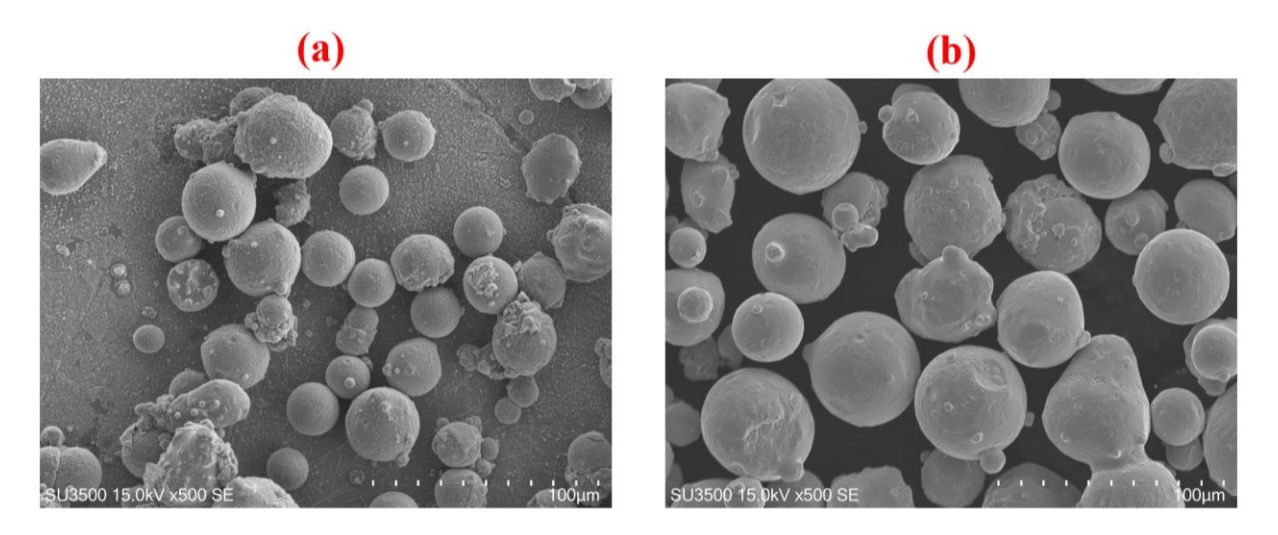


Figure 7.1: SEM images for different powders (a) Inconel 718 powder sample, and (b) stainless steel SS316L powder.

7.2.2 Powder Rheometer

All tests were conducted with the FT4 powder rheometer from Freeman Technology (Tewkesbury, UK) [42, 43]. Stability and variable flow rate (VFR) test has been conducted to examine the stability and sensitivity of the powders [44], where the experiments consisted of repeated VRF tests and conditioning cycles. The flow behavior of the powder is quantified by measuring the resistance of 'conditioned' powder when moving the rotating stainless steel impeller (23.5 mm

diameter) in a vessel (borosilicate glass, fire polished, 25 mm internal diameter, 51 mm height) filled with the powder, **Fig. 7.2-a**. Thus, the distance between the tip of impeller and vessel surface is 750 µm.

The powder sample is preconditioned using the conditioning procedure for the stability and variable flow rate (VFR) test. The conditioning blade provides a gentle disturbance for the powder by using the lifting helix upwards and the slicing helix downwards, where the tip speed of impeller during the conditioning cycle is 40 mm/sec. The purpose of this preparation cycle is to generate a uniformly packed sample with a high level of reproducibility [12]. In addition to that, a 'splitting' mechanism at the top of the vessel was assembled to control the height of the powder column precisely, **Fig. 7.2-a**.

Axial forces and rotational torques acting on the impeller were measured [42], and the total flow energy (e_f) is calculated as the area under the curve [45], **Fig. 7.2-c**. The total flow energy of one test is defined as the resistance to motion of the impeller as it rotates downwards through a volume of conditioned powder through a definite pathway from H_1 to H_2 , **Fig. 7.2-a**.

Yan et al. [38] calculated the total flow energy using the following equation:

$$e_f = \int_{H_1}^{H_2} \left(\frac{P}{r \tan(\theta)} + k_{base} \right) . dh$$
 (7.1)

Where, (k_{base}) and (P) are the vertical force and torque applied on the impeller, (θ) is the helix angle,(r) is the impeller radius and (H) is the penetration depth inside the powder column, **Fig.** 7.2-a. Also, the specific total flow energy (S_f) is (e_f) divided by total mass of powder in the vessel, giving units of $[J.kg^{-1}]$ [46].

As defined by Freeman [12], the flow energy that characterizes a powder is obtained by VFR test, different impeller tip speeds are used. From test 1 to 8, the tip speed is 100 mm/sec, and the tip speeds for test 9, 10 and 11 are 70 mm/sec, 40 mm/sec and 10 mm/sec, respectively. The basic flow energy (BFE) is the total flow energy calculated after the 7th test and is used as an index for the flowability [12, 45].

The continuous flow rate (CFR) test was introduced for this research, which presented a modification of the methodology in [1]. Where, the impeller speed was fixed at 100 mm /sec at

every test, and the total flow energy (e_f) is calculated after each test. In addition to that, splitting was not required after (Test 1), and the mass of powder was kept without moving the powder in vessel. The CFR test was repeated until the values of total energy (e_f) plateaued.

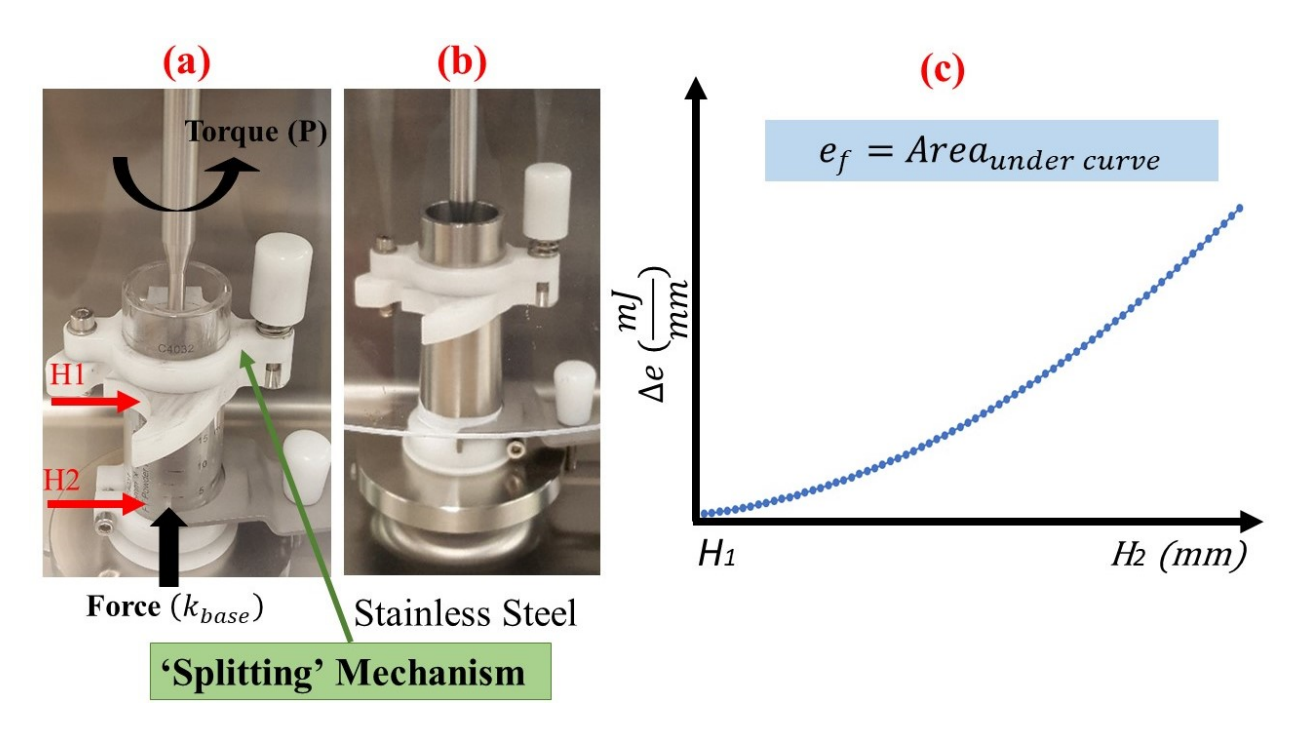


Figure 7.2: (a) Image for the borosilicate glass vessel with representations for torque and force, (b) image for the custom-made stainless steel vessel, and (c) the graph for the calculation of total flow energy.

To investigate the charging effects between the powder and vessel, the following set of experiments (variants 1 and 2) were introduced. When the (e_f) values plateaued, the experiments were repeated by first pouring out the powder in an aluminum cup, and then using the following two experimental variations, while the powder was stored.

For variant 1, the vessel of rheometer was not wiped or cleaned when the powder was poured outside. For variant 2, the vessel was wiped and cleaned when it was empty. Then, the powder was poured into the vessel and the CFR test performed again. The values of (e_f) were observed until plateaued.

To study the effect of a different vessel material, a custom-made stainless steel (SS) vessel with the exact same above dimensions was fabricated, **Fig. 7.2-b**. Finally, the possible tribocharging effect of rotating stainless steel impeller on powders was not considered for this research.

7.3 Results

7.3.1 The Energy Values for the CFR Test for Inconel 718

To examine the charging effects of Inconel 718 powder on the (e_f) values, the CFR test was performed with a 'fresh' (i.e. not previously subjected to a Hall flowmeter test or any powder test) sample of Inconel 718 powder. The change in the total flow energy is presented in **Fig. 7.3**.

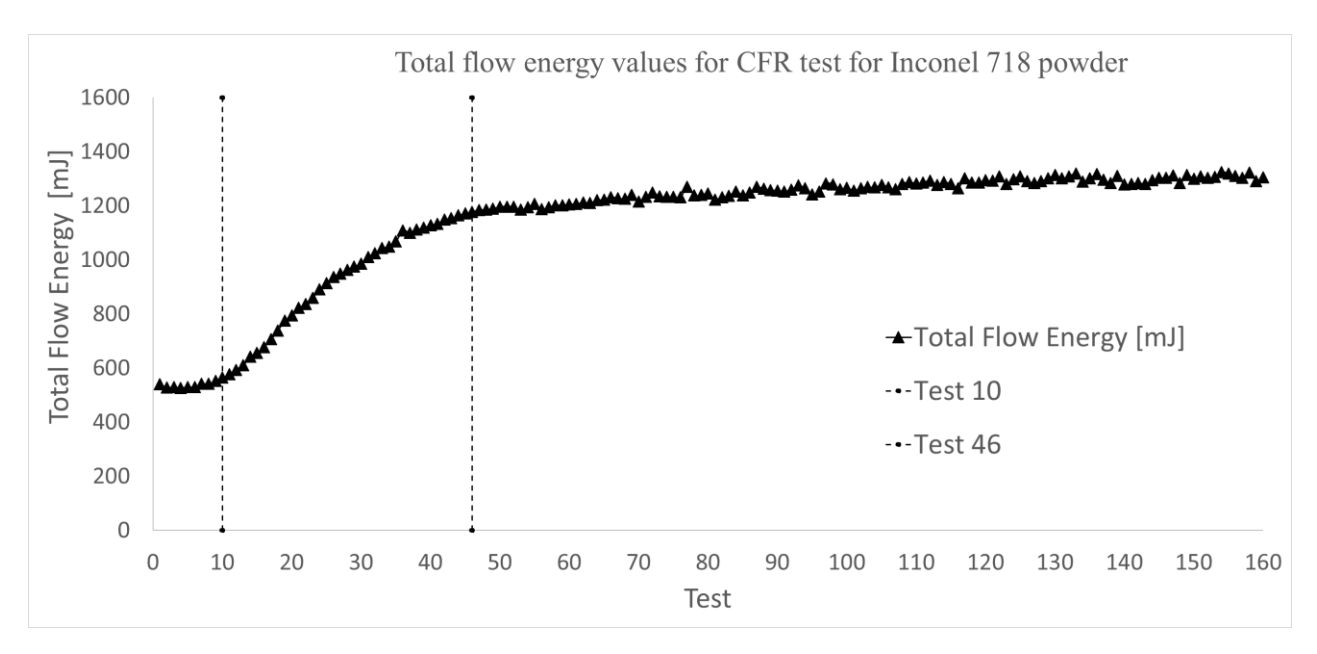


Figure 7.3: The energy values for the continuous flow rate (CFR) test for a fresh sample of Inconel 718 powder.

The evolution of CFR test reveals three periods: (i) The incubation period [47]: an initial region where there is no significant change in energy with test number, (ii) the transition period [47]: a region of rapid rise in the energy, and finally (iii) the electrostatic equilibrium or plateau. Where the increase in energy with test number is correlated with tribocharging [1].

At Test 1, the energy value for the Inconel 718 powder was 540 mJ; this energy was essential to move particles away from the impeller. From Test 1 to 10, the total energy value for the graph increased by 4% only, and the energy value in Test 10 was 564 mJ. Then, the value of total energy increased by 52% from Test 10 to 46. Finally, the energy value (e_f) plateaued at 1300 mJ from Test 47 to 160 and increased by 9% only.

7.3.1.1 Charging Effect between the Vessel and Powder (Variants 1 & 2)

The following two experiments were performed to examine the possible existence and effect of a charging between the vessel and powder particles. When the flow energy for the Inconel 718

powder had plateaued (Test 160), test variants 1 and 2 were applied. For variant 1, the powder was poured into an aluminum cup, but the borosilicate vessel was not wiped or cleaned. Then, the powder was poured back in the borosilicate vessel, and the more tests were performed. The values of total energy, from Tests 161 to 180 appeared to be a continuation of the initial test, **Fig. 7.4**. Thus, the electrostatic equilibrium between the powder particles and vessel was not changed, and the local positive charges on the borosilicate glass vessel were kept without any change.

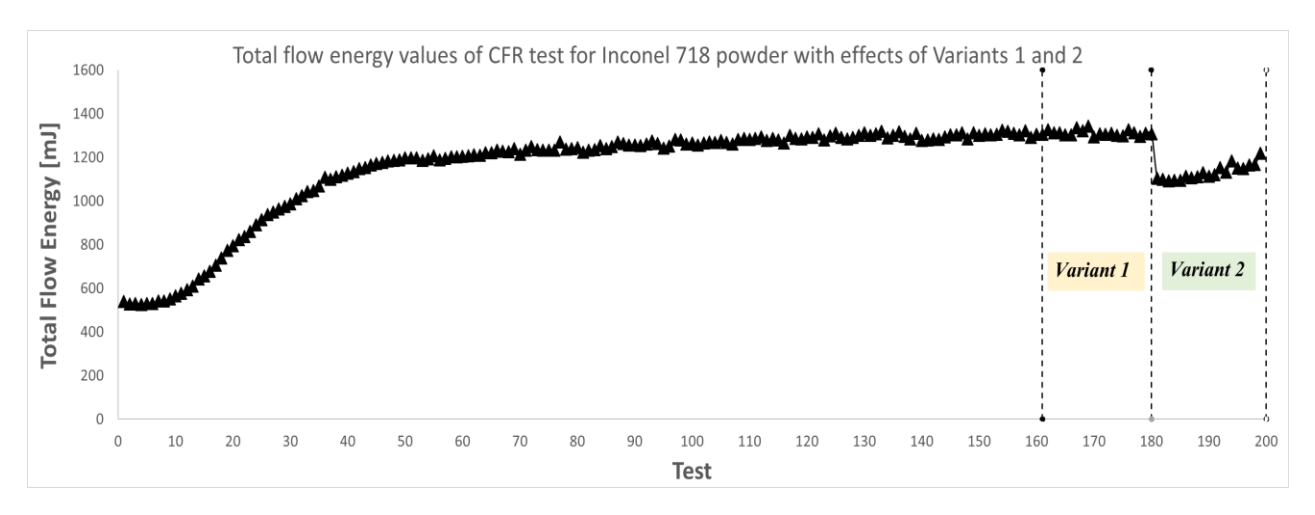


Figure 7.4: The total flow energy values of CFR test for Inconel 718 powder with effects of variants 1 and 2.

After Test 180, the powder was poured again in the aluminum cup, but the borosilicate vessel was wiped and cleaned (variant 2). The powder was then poured back in the borosilicate vessel and tests were conducted. From **Fig. 7.4**, there was a sudden drop in the energy value from Test 180 (1308 mJ) to Test 181 (1103 mJ). To explain this decrease of energy (-18.5%), the electrostatic equilibrium between the powder particles and vessel was disturbed or neutralized during the cleaning process. In other words, the settled powder particles on the vessel were wiped off.

Then, with continued testing, the value of total energy continually increased up to Test 200, where the testing was terminated. A new static equilibrium had established again between the vessel and particles.

7.3.1.2 Flow Measurements Before and After the CFR Test

The following experiment was performed to conduct the possibility of powder charging with the powder rheometer, where the flow of powder was measured with Hall flowmeter before and after the continuous flow rate (CFR) test.

Initially, 50 grams from a fresh sample of Inconel 718 powder was used for the Hall flow measurement, where the powder was kept in a sealed bottle. The flow time for the fresh powder was 17 sec/ 50 gram; however, the flow rate from the product certificate was 16 sec/50 gram. In comparison between the certificate and this measurement, this variation in the flow rate might be related to different ambient conditions during the measurement (at the lab, 21.7°C room temperature and 26% RH relative humidity).

After measuring the flow rate, the powder was poured inside the borosilicate glass vessel of the rheometer, and more powder was added to fill the vessel completely. The mass of powder inside the vessel after the splitting was 107gram.

The continuous flow rate (CFR) test was performed according to the experimental procedure. The CFR test was repeated until the values of total energy (e_f) plateaued. Then, the measurement of Hall flowmeter for this 'used' sample was 20 sec/50 gram; the difference between the final and initial flow rates might be explained by the tribocharging effect.

7.3.2 The Effect of Vessel Material on Tribocharging

The following experiments were performed to examine the effect of vessel material on the tribocharging for Inconel 718 powder. For this experiment, a custom-made stainless steel vessel with same dimensions of the borosilicate glass vessel was utilized, **Fig. 7.2-b**. From **Fig. 7.5**, the values for total flow energy for the Inconel 718 powder in the borosilicate glass and stainless steel vessels are plotted in graphs 1 and 2, respectively.

The two experiments were obtained with fresh samples from the same bottle. Also, the experiment for graph 1 was conducted with 18.4% RH relative humidity and 21.9 °C room temperature. For graph 2, the experiment was conducted with 15.8% RH and 22.9 °C temperature. Because the ambient conditions were almost the same for both experiments, they had the same effects on both experiments.

The evolution of CFR test for the borosilicate glass vessel, as before, reveals three periods: (i) the incubation period [47] from Test 1 to 7, (ii) the transition period [47] from Test 8 to 33, and (iii) an electrostatic equilibrium starting from Test 34.

The CFR evolution with the stainless steel vessel reveals only two periods: the transition period (Test 1 to 33), and the electrostatic equilibrium from (Test 34 to 100). The incubation period has disappeared; the transition period exhibits a much lower rate of increase in compare to the borosilicate glass vessel, but the plateau value is the same. However, the transition periods for both measurements are similar in length.

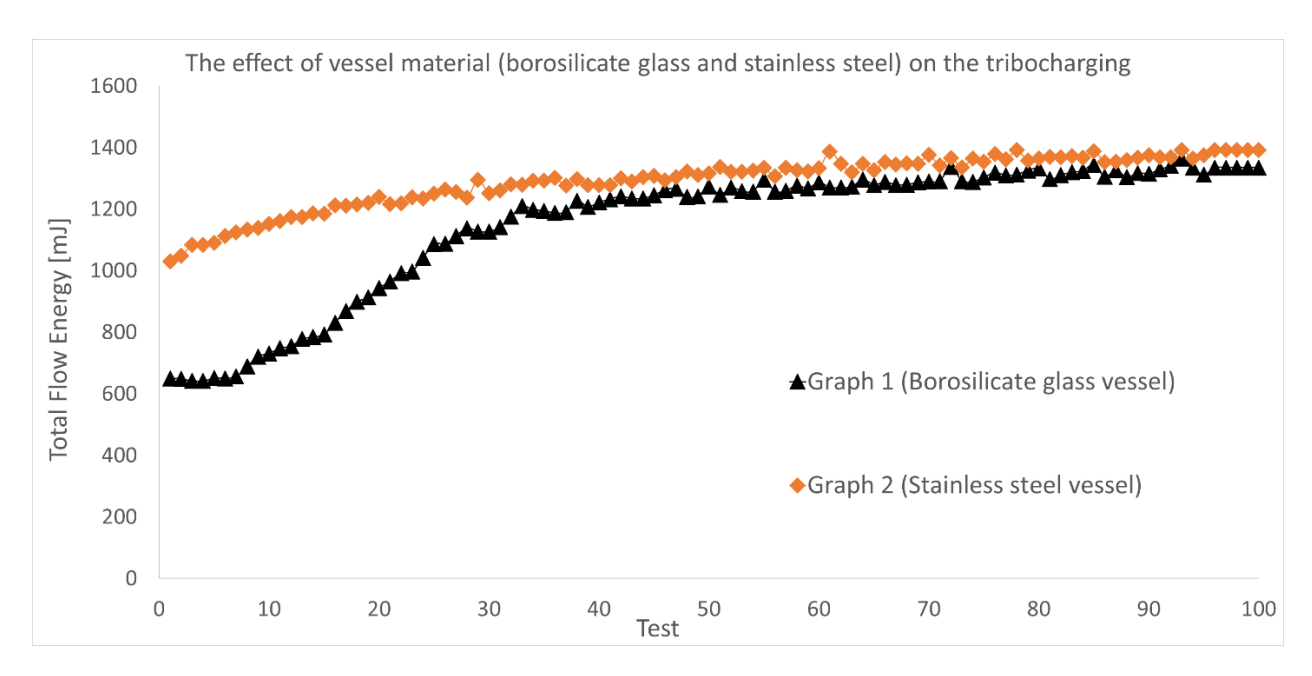


Figure 7.5: The effect of vessel material (borosilicate glass and stainless steel) on the tribocharging for Inconel 718 powder

At Test 1, the value of total flow energy for graph 2 was higher from the energy of graph 1. The powder particles inside the stainless steel vessel required a higher energy (1030 mJ) to move particles away from the impeller in compare to the fresh powder particles (650 mJ) in the borosilicate glass vessel. The graph 1 had increased and approached graph 2 starting from Test 40 (1221 mJ).

For both graphs, if the surface roughness effect for a vessel was dominated from (Test 1 to 33) with the obtained (e_f) values, the vessel effect was disappeared for both graphs starting from Test 40 and the (e_f) values became independent from the surface roughness. These differences may be a result of tribocharging between the powder and vessel, as will be discussed later.

7.3.3 The Effect of Same-material Bipolar Charging

The goal of the following experiment was to detect the effect of same-material bipolar charging. For this reason, stainless steel (SS316L) powder particles and the stainless steel vessel were utilized. The CFR tests for the stainless steel (SS316L) powder in the borosilicate glass and stainless steel vessels are presented in **Fig. 7.6**. Where, graphs (α) and (β) present the values of total flow energy of the stainless steel (SS316L) powder in the borosilicate glass and stainless steel vessels, respectively.

The experiment for graph (α) was conducted with 18.4% RH and 21.9 °C room temperature. On the other hand, the experiment for graph (β) was conducted with 15.8% RH and 22.9 °C room temperature. Because the ambient conditions were almost the same for both experiments, they had the same effects on both experiments.

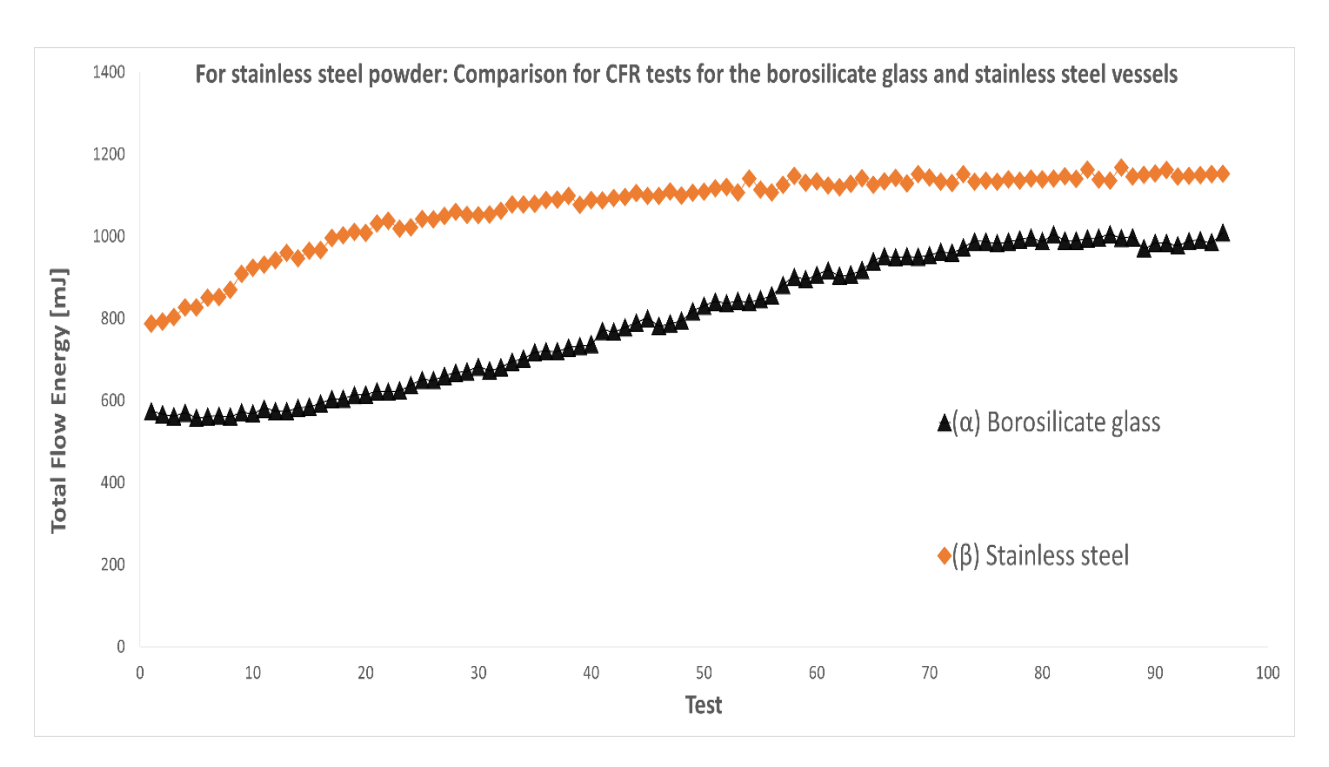


Figure 7.6: For the stainless steel (SS316L) powder: the comparison for the continuous flow rate (CFR) tests for the borosilicate glass and stainless steel vessels.

The CFR curves are similar to the previous results; in that the borosilicate glass vessel reveals the three periods but the stainless steel vessel reveals only the transition and the electrostatic equilibrium.

For graph (α) , the evolution of CFR test for the borosilicate glass vessel reveals three regions: (i) the incubation period from Test 1 to 16, (ii) the transition period from Test 17 to 74, and (iii) an electrostatic equilibrium starting from Test 75. For graph (β) , the CFR evolution with the stainless steel vessel reveals only two regions: the transition period from Test 1 to 37, and the electrostatic equilibrium starting from Test 38. The incubation period has disappeared, and the transition period for graph (α) is much longer than for the graph (β) .

For Test 1, the value of total flow energy for the stainless steel (SS316L) powder in the stainless steel vessel was higher than the flow energy in the borosilicate glass vessel. In other words, the powder particles inside the stainless steel vessel required a higher energy (786 mJ) to move particles away from the impeller in compare to the fresh powder particles (573 mJ) in the borosilicate glass vessel. Unlike the previous test with Inconel 718 powder, when the graphs (α) and (β) plateaued, they almost had approached the same energy value with a difference of 12% only.

7.3.4 Same-Material Bipolar Charging for a Non-Conductive Material

To investigate the possible same-material charging for a non-conductive material, the CFR test for glass microspheres was obtained in the borosilicate glass vessel, **Fig. 7.7**. From (Test 1 to 70), the value of total energy increased by 11%, and the graph plateaued starting from (Test 48) with 226 mJ. Minor to no-charging occurred with the glass microspheres, i.e. the same-material charging between non-conductive surfaces occurred with very limited aspects.

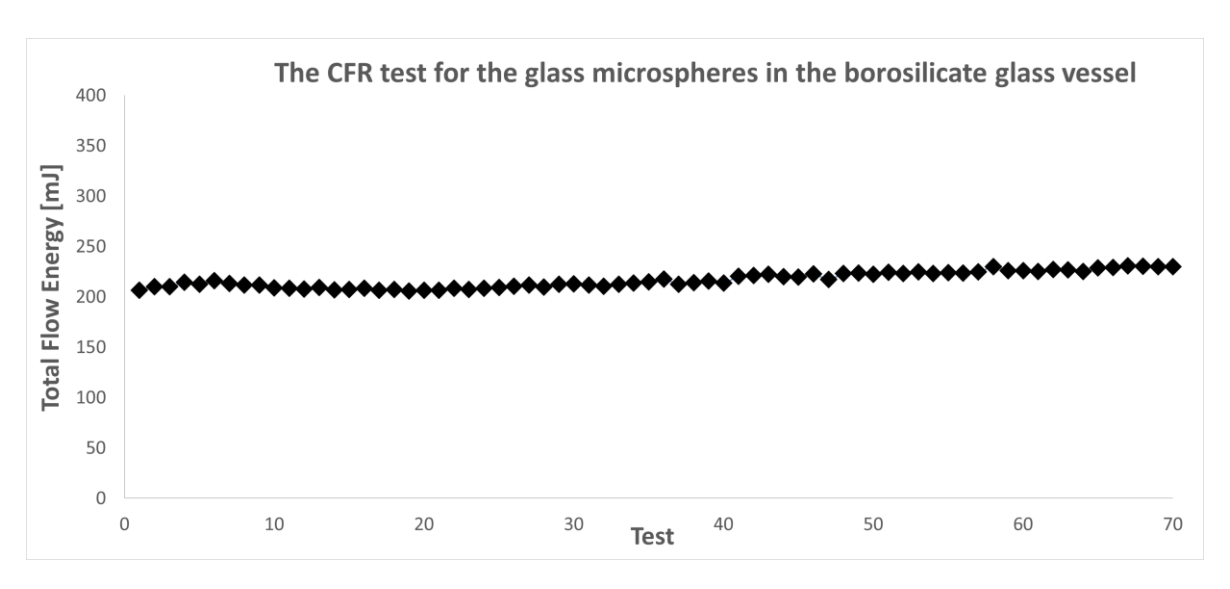


Figure 7.7: The graph of CFR test for the glass microspheres in the borosilicate glass vessel

7.4 Discussion

7.4.1 Effect of Tribocharging on Total Flow Energy

To analyze the charging events during the CFR test, the new triboelectric series in Chapter 6 was utilized. Where, some of the materials from the series were listed in order from the most electronegative towards the most electro-positive material: Inconel 718, stainless-steel 316L, and borosilicate glass fire polished.

From the previous results, there is an increase in the total flow energy which occurs over three or two periods. As well, **Figures 7.5** and **7.6** indicate that the vessel is involved in the tribocharging behavior. This charging is basically caused by two charging events, these being interactions between (i) powder/vessel, and (ii) powder/powder particles [48]. The total flow energy is then comprised of coulombic forces between powder and the vessel due to the tribocharging, and between powder particles as a result of same-material bipolar charging. In the latter, larger particles tend to lose electrons (become positively charged) on coming in contact with smaller particles, which gain electrons (become negatively charged) [26, 29]. Since there is a powder velocity gradient increasing from the center to the vessel wall [49], it is likely that the tribocharging effect of powder/vessel takes place initially, then the same-material bipolar charging effect of powder/powder eventually will be added to the total flow energy.

From Fig 7.3, which is the CFR test for Inconel 718 in the borosilicate glass vessel, the incubation period is where the total flow energy values are constant; this suggests that it takes some time to develop a charge (lose electrons and become positively charged) on the vessel. On the other hand, in Fig. 7.5, which is the CFR test for Inconel 718 powder and the stainless steel vessel, there is no incubation period, which suggests that a charge develops very quickly on the vessel.

The differences in the charging time could be related to the presence of 'free' electrons in stainless steel and the fact that electrons are not free in the borosilicate glass. Contact surfaces for the two metals (Inconel 718 and stainless steel) exchange electrons by tunneling mechanism to maintain the thermodynamic equilibrium [50]. During the interaction between a metallic surface (Inconel 718 particles) with an insulator (borosilicate glass), the transfer of charges can be explained by a similar hypothesis of the metal/ metal electron transfer with the assumption of an "effective work function" is assigned to the insulator [51].

The transition period is a combination of the vessel/powder and powder/powder charging events leading to an electrostatic equilibrium. The same effects were seen for the stainless steel powder (**Fig. 7.6**) which indicates that a vessel of the same material as the powder can also be charged; this could be regarded as an extension of larger particles interacting with smaller particles, where the vessel wall acts as a 'large' particle.

However, as pointed out above, there are differences between the Inconel 718 and stainless steel (SS316L) powders behaviors: (i) the electrostatic equilibrium periods for the SS316L powder are at lower total flow energies in compare with Inconel 718 powder, (ii) the transition period for the SS316L powder in the borosilicate glass vessel is much longer than for the same powder in the stainless steel vessel and (iii) the specific total flow energy (S_f) values for Inconel 718 powder in both used vessels were higher than the (S_f) values for SS316L (The specific total flow energy (S_f) for a powder is defined as the required energy to increase the total flow energy per unit mass from the incubation period to the electrostatic equilibrium (steady state)).

According to Fig. 7.5 and Fig. 7.6, the specific total flow energy (S_f) due to charging is presented in **Table 7.1**.

Table 7.1: The specific total flow energy (S_f) for Inconel 718 and stainless steel 316L powder samples

Powder		Mass [Kg]	$\Delta e = e_{f, ext{electrostatic equilibrium}} - e_{f, ext{incubation period}}$ [Joule]	$S_f = \frac{\Delta e}{mass}$ [Joule/Kg]
Inconel 718 Inconel 718	(Graph 1)	0.102	0.563 0.566	5.52
SS316L	(Graph α)	0.112	0.435	3.88
SS316L	(Graph β)	0.111	0.366	3.30

According to **Table 7.1**, the (S_f) values with the borosilicate glass vessel (graphs 1 and α) were higher than the (S_f) values with the stainless steel vessel (graphs 2 and β).

The previous three differences might be related to the relative positions of these materials (Inconel 718 and Stainless steel) in the new triboelectric series in Chapter 6.

In terms of the flow measurements, perhaps having a much larger clearance between the blade edge of impeller and vessel might be advisable to minimize or even eliminate the influence of the vessel on the flow metrics.

Regarding the powder flow in additive manufacturing AM process, the behavior can be dynamic, but there is an electrostatic equilibrium where the interaction of flow and charging is static. Obviously, reaching an electrostatic equilibrium (steady state) is positive for process stability, and perhaps, powder processing methods need to be developed so that as-received powders are at an electrostatic equilibrium.

7.4.2 Same-Material Bipolar Charging for a Non-Conductive Material

From **Fig. 7.7**, the specific total flow energy (S_f) due to same-material bipolar charging for glass microspheres powder in the borosilicate glass vessel is obtained in **Table 7.2**.

Table 7.2: The specific total flow energy (S_f) for glass microspheres powder sample

		_ A
Mass	$\Delta e = e_{f, ext{electrostatic}}$ equilibrium $-e_{f, ext{incubation}}$ period	$S_f = \frac{\Delta e}{}$
[Kg]	[Joule]	mass mass
	[voult]	[Joule/Kg]
0.037	0.023	0.63

The result obtained in **Fig. 7.7** agreed with same results obtained by Yan et al. [38], where two set of glass beads with particles of 2 mm and 4 mm diameters were tested by the CFR test for 20 consecutive tests (100 mm/sec tip speed). Although the powder column was significantly changed due to segregation, the value of total flow energy did not change. Yan et al. [38] tried to correlate between the flow energy and segregation mechanism. To correlate between the total flow energy and the segregation index, a mixture of binary system with distinguish flow behaviors was used.

As a matter of fact, the glass microspheres with 10 - 95 µm PSD segregated during the CFR test, where the segregation mechanism occurred due to the volume fraction and particle size ratios [38]. From this work, during the CFR test, the increase of total flow energy values was caused by the tribocharging and bipolar charging phenomenon.

When powder particles get charges during the CFR test, a segregation mechanism occurs between particles. For a conductive powder (Inconel 718 and SS316L) with CFR test, the existence of PSD

and interactions with the vessel during have caused the tribocharging; this charging might cause to segregate the particles. On the other hand, no-charging, or a minor was conducted for the glass microspheres, but the segregation was occurred as a result the wide range of PSD (10 - 95 μ m). If the total flow energy had plateaued for the entire test in **Fig. 7.7**, the segregation was occurred but without tribocharging.

7.5 Conclusions

This work provided the theoretical background for the tribocharging between different materials and same-material bipolar charging phenomena. A novel method was described, where tribocharging can be generated by interaction between particles from the same material inside a powder rheometer. The tribocharging for metallic powders inside the powder rheometer was investigated by the total flow energy (e_f) , and a correlation between flowability and tribocharging was described. As a result of this method, the effect of vessel material on the tribocharging was evaluated. In the borosilicate glass vessel, the evolution of CFR test showed three periods listed in order, the incubation period, the transition period, and the electrostatic equilibrium. The incubation period disappeared in the stainless steel vessel, and the other two periods took place.

Appendix (A7)

Gas atomized nickel-based alloy Inconel 718 (15 - 45 µm) powder from (Carpenter Powder Products Inc, USA) was used in **Chapters 6 and 7**. According to the powder certificate, the chemical compositions of this powder are listed in **Table A7.1**

Table A7.1: The constituents of Inconel 718 based on Carpenter powder certificate.

Element	Weight Percentage %
Nickel	53.06
Chromium	19.65
Carbon	0.04
Manganese	0.02
Silicon	0.03
Phosphorus	0.002
Sulfur	0.001
Cobalt	0.09
Molybdenum	3.07
Titanium	1.0
Aluminum	0.4
Copper	0.02
Boron	< 0.001
Iron	Balance
Oxygen	0.017
Nitrogen	0.005

Gas atomized stainless steel (SS316L) from (Sandvik Osprey, Sweden) powder was used in **Chapters 6 and 7**. The chemical compositions of this powder was examined by Barua [52] using the inductively coupled plasma optical emission spectroscopy (ICP-OES). The measured chemical compositions are presented in Table A7.2

Table A7.2: The chemical compositions of stainless steel SS316L [52]

Element	Weight Percentage %
Iron	68.71
Chromium	16.36
Nickel	10.90
Molybdenum	2.33
Manganese	1.41
Silicon	0.28
Carbon	0.014

References

- [1] B. Alchikh-Sulaiman, P. R. Carriere, X. Chu, Y. Liu, and S. Yue, "Powder spreading and tribocharging for additive manufacturing process," *Euro PM2019: European Powder Metallurgy Association*, O. Coube Ed., October 13-16, 2019 (Maastricht, The Netherlands), Euro PM 2019, pp. (4347446) 1-6.
- [2] N. Hopkinson and P. Dickens, "Rapid prototyping for direct manufacture," *Rapid Prototyping J.*, vol. 7, pp. 197-202, 2001.
- [3] A. S. Salles and D. E. Gyi, "Delivering personalized insoles to the high street using additive manufacturing," *Inter. J. Computer Integrated Manufacturing*, vol. 26, pp. 386-400, 2013.
- [4] G. Baudana, S. Biamino, D. Ugues, M. Lombardi, P. Fino, M. Pavese, and C. Badini, "Titanium aluminides for aerospace and automotive applications processed by electron beam melting: contribution of Politecnico di Torino," *Met. Powder Rep.*, vol. 71, pp. 193-199, 2016.
- [5] Y. Sun, S. Gulizia, C. Oh, C. Doblin, Y. Yang, and M. Qian, "Manipulation and characterization of a novel titanium powder precursor for additive manufacturing applications," *The Min. Met. Mater. Soc.*, vol. 67, pp. 564-572, 2015.
- [6] V. Petrovic, J. V. Gonzalez, O. J. Ferrando, J. D. Gordillo, J. R. Puchades, and L. P. Grinan, "Additive layered manufacturing: Sectors of industrial application shown through case studies," *Inter. J. Produc. Res.*, vol. 49, pp. 1061-1079, 2011.
- [7] Z. H. Liu, D. Q. Zhang, S. L. Sing, C. K. Chua, and L. E. Loh, "Interfacial characterization of SLM parts in multi-material processing: Metallurgical diffusion between 316L stainless steel and C18400 copper alloy," *Mater. Character.*, vol. 94, pp. 116-125, 2014.
- [8] J. P. Choi, G. H. Shin, H. S. Lee, D. Y. Yang, S. Yang, C. W. Lee, M. Brochu, and J. H. Yu, "Evaluation of powder layer density for the selective laser melting (SLM) process," *Mater. Trans.*, vol. 58, pp. 294-297, 2017.
- [9] J. Clayton, J. Dawes, and C. Langley, "Optimizing metal powders for additive manufacturing: exploring the impact of particle morphology and powder flowability," *additivemanufacturing.media*, May 26, 2017. [Online]. Available: http://www.additivemanufacturing.media/blog/post/optimizing-metal-powders-for-additive-manufacturing-exploring-the-impact-of-particle-morphology-and-powder-flowability. [Accessed Dec. 20, 2018].

- [10] B. A. AlMangour, "Additive manufacturing of high-performance 316L stainless steel nanocomposites via selective laser melting," Ph.D. dissertation, Dept. Mater. Eng., University of California, Los Angeles, CA, 2017.
- [11] W. J. Mills and L. A. James, "Effect of heat-treatment and heat-to-heat variations in the fatigue-crack growth response of alloy 718," *Eng. Fracture Mech.*, vol. 22, pp. 797-817, 1985.
- [12] R. Freeman, "Measuring the flow properties of consolidated, conditioned and aerated powders-a comparative study using a powder rheometer and a rotational shear cell," *Powder Tech.*, vol. 174, pp. 25-33, 2007.
- [13] M. K. Stanford and C. DellaCorte, "Effects of humidity on the flow characteristics of a composite plasma spray powder," *J. Therm. Spray. Tech.*, vol. 15, pp. 33-36, 2006.
- [14] B. Alchikh-Sulaiman, F. Ein-Mozaffari, and A. Lohi, "Evaluation of poly-disperse solid particles mixing in a slant cone mixer using discrete element method," *Chemical Engineering Research and Design*, vol. 96, pp. 196-213, 2015.
- [15] M. Peleg, "Flowability of food powders and methods for its evaluation-A review," *J. Food Proc. Eng.*, vol. 1, pp. 303-328, 1977.
- [16] V. Ganesan, K. A. Rosentrater, and K. Muthukumarappan, "Flowability and handling characteristics of bulk solids and powders-A review with implications for DDGS," *Biosystems Engineering*, vol. 101, pp. 425-435, 2008.
- [17] E. R. Rice and J. Tengzelius, "Die filling characteristics of metal powders," *Powder Meta.*, vol. 29, pp. 183-194, 1986.
- [18] A. Santomaso, P. Lazzaro, and P. Canu, "Powder flowability and density ratios: the impact of granules packing," *Chem. Eng. Sci.*, vol. 58, pp. 2857-2874, 2003.
- [19] J. E. Peterson and W. M. Small, "Evaluation of metal powders using Arnold density meter and Hall flowmeter," *Powder Meta.*, vol. 37, pp. 37-41, 1994.
- [20] ASTM International, "ASTM B213-13: standard test methods for flow rate of metal powders using the Hall flowmeter funnel," *in Annual book of ASTM standards 2013 (pp. 27-30)*. West Conshohocken, PA: American Society for Testing and Materials, 2013.
- [21] D. Schulze, *Powders and Bulk Solids: Behavior, Characterization, Storage and Flow*. Berlin, Germany: Springer-Verlag Berlin Heidelberg, 2008.
- [22] W. D. Greason, "Investigation of a test methodology for triboelectrification," *J. Electrostatics*, vol. 49, pp. 245-256, 2000.

- [23] T. Nomura, T. Satoha, and H. Masuda, "The environment humidity effect on the tribocharge of powder," *Powder Tech.*, vol. 136, pp. 43-49, 2003.
- [24] S. Trigwell, N. Grable, C. U. Yurteri, R. Sharma, and M. K. Mazumder, "Effects of surface properties on the tribocharging characteristics of polymer powder as applied to industrial processes," *IEEE Transactions on Industry applications*, vol. 39, pp. 79-86, 2003.
- [25] M. B. Neagoe, Y. E. Prawatya, T. Zeghloul, and L. Dascales, "Influence of surface roughness on the tribo-electric process for a sliding contact between polymeric plate materials," *IOP Conf. Series: Mater. Sci. Eng.*, vol. 174, pp. 1-6, 2017.
- [26] R. Mukherjee, V. Gupta, S. Naik, S. Sarkar, V. Sharma, P. Peri, and B. Chaudhuri, "Effects of particle size on the triboelectrification phenomenon in pharmaceutical excipients: experiments and multi-scale modelling," *Asian J. Pharm. Sci.*, vol. 11, pp. 603-617, 2016.
- [27] B. Lee and D. Orr, "The TriboElectric Series,". *alphalabinc.com*, 2018. [Online]. Available: https://www.alphalabinc.com/triboelectric-series/. [Accessed July 14, 2019].
- [28] G. Freeman and N. March, "Triboelectricity and some associated phenomena," *Mater. Sci. Tech.*, vol. 15, pp. 1454-1458, 1999.
- [29] S. R. Waitukaitis, V. Lee, J. M. Pierson, S. L. Forman, and H. M. Jaeger, "Size-dependent same-material tribocharging in insulating grains," *Ameri. Phys. Soc.*, vol. 112, pp. 218001(1-5), 2014.
- [30] H. Zhao, G. S. Peter Castle, I. I. Inculet, and A. G. Bailey, "Bipolar charging of polydisperse polymer powders in fluidized beds," *IEEE Trans. Ind. Appl.*, vol. 39, pp. 612-618, 2003.
- [31] K. M. Forward, D. J. Lacks, and R. M. Sankaran, "Triboelectric charging of granular insulator mixtures due solely to particle–particle interactions," *Ind. Eng. Chem. Res.*, vol. 48, pp. 2309-2314, 2009.
- [32] P. Porion, N. Sommier, A. Faugere, and P. Evesque, "Dynamics of size segregation and mixing of granular materials in a 3D-blender by NMR imaging investigation," *Powder Tech.*, vol. 141, pp. 55-68, 2004.
- [33] B. Remy, J. G. Khinast, and B. J. Glasser, "Discrete element simulation of free flowing grains in a four-bladed mixer," *AlChE Journal*, vol. 55, pp. 2035-2048, 2009.
- [34] B. Remy, J. G. Khinast, and B. J. Glasser, "Polydisperse granular flows in a bladed mixer: Experiments and simulation of cohesionless spheres," *Chem. Eng. Sci.*, vol. 66, pp. 1811-1824, 2011.

- [35] B. Alchikh-Sulaiman, M. Alian, F. Ein-Mozaffari, A. Lohi, and S. R. Upreti, "Using the discrete element method to assess the mixing of polydisperse solid particles in a rotary drum," *Particuology*, vol. 25, pp. 133-142, 2016.
- [36] P. Tang and V. M. Puri, "Methods for minimizing segregation: a review," *Particulate Science and Technology*, vol. 22, pp. 321-337, 2004.
- [37] Y. Pu, M. Mazumder, and C. Cooney, "Effects of electrostatic charging on pharmaceutical powder blending homogeneity," *J. Pharm. Sci.*, vol. 98, pp. 2412-2421, 2009.
- [38] Z. Yan, S. K. Wilkinson, E. H. Stitt, and M. Marigo, "Investigating mixing and segregation using discrete element modelling (DEM) in the Freeman FT4 rheometer," *Int. J. Pharm.*, vol. 513, pp. 38-48, 2016.
- [39] J. Yao, Y. Zhang, C.H. Wang, and Y.C. Liang, "On the electrostatic equilibrium of granular flow in pneumatic conveying systems," *J. AIChE*, vol. 52, pp. 3775-3793, 2006.
- [40] ASTM International, "Standard specification for additive manufacturing nickel alloy (UNS N07718) with powder bed fusion," *in Annual book of ASTM standards 2014 (pp.1-8)*. West Conshohocken, PA: American Society for Testing and Materials, 2014.
- [41] ASTM International, "Stainless steel wire ASTM A 580/A580M-06," in Annual book of ASTM standards 2006 (pp. 1-5). West Conshohocken, PA: American Society for Testing and Materials, 2006.
- [42] J. Clayton and R. Deffley, "Optimizing metal powders for additive manufacturing," *Metal Powder Report*, vol. 69, pp. 14-17, 2014.
- [43] C. Hare, U. Zafar, M. Ghadiri, T. Freeman, J. Clayton, and M. J. Murtagh, "Analysis of the dynamics of the FT4 powder rheometer," *Powder Tech.*, vol. 285, pp. 123-127, 2015.
- [44] B. Alchikh-Sulaiman, P. R. Carriere, and S. Yue, "For Powder Bed Additive Manufacturing Process: Correlations between Single Layer Density and Powder Properties with the Assistance of Coherence Scanning Interferometry," *PowderMet 2019: International Conference on Powder Metallurgy & Particulate Materials*, D. Reardon and V. Warke Ed., June 23-26, 2019 (Phoenix, AZ, USA), Metal Powder Industries Federation, pp. 285-304.
- [45] P. Li, "Effect of powder flow properties on the process performance of loss-in-weight feeders," M. S. thesis, Dept. Chem. Eng., University of New Jersey, New Brunswick, NJ, 2015.
- [46] C. McGuire, "Granular flow properties of food powders in extrusion processing," M.S. thesis, Dept. Grain Sci., Kansas State University, Manhattan, KS, 2017.

- [47] F. Wakai, N. Enomoto, and H. Ogawa, "Three-dimensional microstructural evolution in ideal grain growth-general statistics," *Acta Mater*, vol. 48, pp. 1297-1311, 2000.
- [48] P. M. Ireland, "Dynamic particle-surface tribocharging: the role of shape and contact mode," *J. Electro.*, vol. 70, pp. 524-531, 2012.
- [49] R. Bharadwaj, W. R. Ketterhagen, and B. C. Hancock, "Discrete element simulation study of a Freeman powder rheometer," *Chem. Eng. Sci.*, vol. 65, pp. 5747-5756, 2010.
- [50] W. R. Harper, "The Volta effect as a cause of static electrification," *Proc. R. Soc. Lond. A*, vol. 205, pp. 83-103, 1951.
- [51] S. Matsusaka, H. Maruyama, T. Matsuyama, and M. Ghadiri, "Triboelectric charging of powders: A review," *Chem. Eng. Sci.*, vol. 65, pp. 5781-5807, 2010.
- [52] R. Barua, "Study of the structural properties and control of degradation rate for biodegradable metallic stents using cold spray," Ph.D. dissertation, Dept. Mater. Eng., McGill University, Montreal, QC, 2015.

Chapter 8

8.1 Global Discussion

Since Chapters 3 - 7 were prepared as separate manuscripts, a global discussion is provided to unify the findings and conclusions.

Powder spreading and flow would, superficially, appear to be similar processes. However, there are differences between flow and spreading which were distinguished clearly. For a single layer, the main differences between spreading and flow are concerned with substrate surface characteristics, temperature, and topography [1, 2].

The contact-sintering technique was utilized to examine spreadability for single layer (SL) samples. Where, a specific cavity, with height of 76.2 μ m or 101.6 μ m, was utilized during the spreading procedure. The cavity was introduced to simulate spreading in a real AM process when the build 'table' was lowered by a specific height to allow the spreading of a layer.

8.1.1 The Effect of Tribocharging on Spreading

From **Fig. 8.1**, on the edge of the single layer (SL) samples, the powder height was 2 to 3 powder particles thick, similar to conventional powder bed fusion PBF spreading metrics [3]. Hence, a large fraction of the contact points is between powder particles and the substrate.

Thus, the substrate surface parameters (topography and temperature) influence the spreading. For SL samples, the spreading was conducted before transferring the SL sample inside the thermal furnace, or before closing the chamber for the pumping down process. In other words, the temperature of substrates was kept unchanged, i.e. similar to the laboratory temperature. Thus, the substrate topography was the main parameter to control spreading.

It was mentioned earlier that the spreading is controlled by the following interparticle forces [4, 5]: friction, coulombic forces (tribocharging), and adhesive forces.

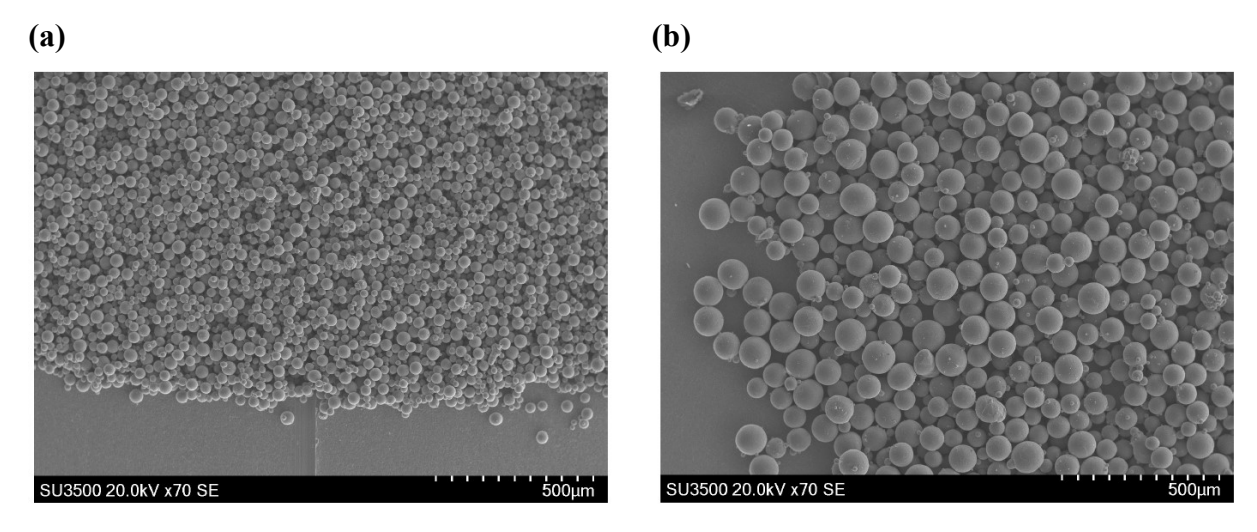


Figure 8.1: SEM images on the edge for two SL contact-sintering samples of Ti-6Al-4V powder with (a) 15-45 μ m PSD and (b) 45-106 μ m PSD.

The SL powder samples were prepared from gas or plasma atomized spherical powders with a minimum number of satellites. A 'fresh' (i.e. not previously subjected to a Hall flowmeter test or any powder test) sample of powder was used for every experiment, and the ambient conditions for storing the powder and spreading were kept unchanged. Thus, the effects of adhesive and friction forces on spreading are likely similar for SL samples in this thesis and tribocharging becomes the main dynamic variable.

For an additive manufacturing powder bed fusion (AM-PBF) process, the powder particles are spread by rake over a metallic substrate to generate a SL of powder. In the powder rheometer used in this research, the particles slide and rotate over the internal surface of the stainless steel vessel during the continuous flow rate (CFR) test. Thus, this CFR test has some similarities to powder spreading in AM-PBF.

The CFR test was used to evaluate charging effects of the stainless steel vessel on the flow of powder, where the flow is quantified by measuring the resistance of 'conditioned' powder when moving the rotating stainless-steel impeller (23.5 mm diameter) in a vessel (stainless steel, 25 mm internal diameter, 51 mm height) filled with a powder. Thus, the distance between the tip of impeller and vessel surface is 750 µm.

As a result of this small distance between the tip of impeller and vessel surface, the vessel of the rheometer is involved in the tribocharging events; these being interactions between (i) powder/vessel [6], and (ii) powder/powder particles [7].

For the contact-sintering SL experiments, a specific cavity height (76.2 µm or 101.6 µm) was settled between the substrate and rotating puck. In comparison to the powder rheometer, the substrate may be involved in the tribocharging events; these being interactions between (i) powder/substrate, and (ii) powder/powder particles.

Recently, Hesse et al. [8] have investigated the tribocharging for polyamide powder during the spreading in SLM process. The charge spectrometry was used to investigate the existence of same-material bipolar charging between particles in the powder bed, and this charging event was confirmed.

The main conclusion of this work is therefore that tribocharging occurs when powders are moving relatively between themselves or between a stationary surface and moving particles, and the future work will be to examine the effect of this on spreading in powder bed fusion AM processing.

Should there be a significant influence on spreading, with regard to process control, maintaining the same level of tribocharging during a build would then be necessary. Since powders seem to reach a state of electrostatic equilibrium, perhaps processing the powders so that this equilibrium is reached before using the powder should be considered as part of any AM powder bed procedure. On the other hand, powders which possess a high level of tribocharging may introduce a safety hazard, so perhaps methods need to be developed that minimize or eliminate any tribocharging.

References

- [1] L. Loewgren and M. Wildheim, "Method for improved powder layer quality in additive manufacturing", U.S. Patent 2016/0129501 A1, May 12, 2016.
- [2] E. Parteli and T. Pöschel, "Particle-based simulation of powder application in additive manufacturing," *Powder Tech.*, vol. 288, pp. 96-102, 2016.
- [3] W. Nan, M. Pasha, T. Bonakdar, A. Lopez, U. Zafar, S. Nadimi, and M. Ghadiri, "Jamming during particle spreading in additive manufacturing," *Powder Tech.*, vol. 338, pp. 253-262, 2018.
- [4] M. K. Stanford and C. DellaCorte, "Effects of humidity on the flow characteristics of a composite plasma spray powder," *J. Therm. Spray. Tech.*, vol. 15, pp. 33-36, 2006.
- [5] D. Schulze, *Powders and Bulk Solids: Behavior, Characterization, Storage and Flow.* Berlin, Germany: Springer-Verlag Berlin Heidelberg, 2008.
- [6] B. Alchikh-Sulaiman, P. R. Carriere, X. Chu, Y. Liu, and S. Yue, "Powder spreading and tribocharging for additive manufacturing process," *Euro PM2019: European Powder Metallurgy Association*, O. Coube Ed., October 13-16, 2019 (Maastricht, The Netherlands), Euro PM 2019, pp. (4347446) 1-6.
- [7] P. M. Ireland, "Dynamic particle-surface tribocharging: the role of shape and contact mode," *J. Electro.*, vol. 70, pp. 524-531, 2012.
- [8] N. Hesse, M. A. Dechet, J. S. Bonilla, C. Lübbert, S. Roth, A. Buck, J. Schmidt, and W. Peukert, "Analysis of tribo-charging during powder spreading in selective laser sintering: Assessment of polyamide 12 powder ageing effects on charging behavior," *Polymers*, vol. 11, pp. 1-12, 2019.

8.2 Conclusions

To evaluate spreadability for AM-PBF, a novel technique was proposed in which a single layer of powder was spread by a standard method, 'frozen' in the as spread condition by 'contact-sintering' and then characterized using coherence scanning interferometry (white-light interferometry).

Three surface topography parameters (surface roughness R_a (μ m), Skewness parameter S_{sk} and the root mean square gradient of the surface S_{dq} (μ m/mm) were applied to compare between substrates. Also, the texture for a single layer was evaluated with the previous topographical parameters.

The powder rheometer has some similarities to powder spreading in additive manufacturing powder bed fusion (AM-PBF) process and was therefore used to investigate relations between flowability and powder properties. The applicability and repeatability of the stability and variable flow rate (VFR) test in the powder rheometer were examined.

In particular, the powder rheometer was used to detect tribocharging effects for different additive manufacturing (AM) metallic powders. A novel technique was introduced to investigate tribocharging generated inside the powder rheometer and assessed its effect on the flowability of powder using the total flow energy (e_f) generated by the continuous flow rate (CFR) test. This charging was basically caused by the interactions between the powder/powder particles and powder/vessel. Thus, the evolution of CFR test in the borosilicate glass vessel revealed three periods: (i) the incubation period, (ii) the transition period, and finally (iii) the electrostatic equilibrium. The evolution of CFR test in the stainless steel vessel revealed the transition, and the electrostatic equilibrium periods, but there was no incubation period. In addition, a new triboelectric series was obtained with the assistance of powder rheometer, where the positions of Inconel 718, commercial purity titanium and Ti-6Al-4V were proposed in this series.

8.3 Future work

For powder bed fusion processes, a correct understanding of the particle charging, the control of charge distribution over a powder bed, and relevant measurement techniques for particles movement are required. The following research topics need to be addressed in near future.

- 1. If the Hall flowmeter and powder rheometer can be installed inside a glove box, the flowrate, stability and variable flow rate (VFR) and continuous flow rate (CFR) tests can be conducted for different additive manufacturing (AM) metallic powders with different ambient conditions (%RH relative humidity and temperature). Thus, the charging behavior for a powder can be obtained, and then, correlated with the flow rate.
- 2. Different rheometer vessel materials need to be fabricated (such as, plastic, aluminum, etc.), so their tribocharging effects can be compared with results obtained in Chapter 7.
- 3. Based on the results obtained in Chapter 7, the tribocharging and same-material bipolar charging might affect the spreadability in AM-PBF. Therefore, a next step would be to examine the interrelationship between spreadability and tribocharging by varying tribocharging levels and performing the spreadability test with these powders.
- 4. For the spreadability testing, different thicknesses should be applied to help explain the correlation between powder mass and particle size distribution, and the corresponding packing factor.